

68787

MICROSTRUCTURE AND HIGH TEMPERATURE PHASE STUDIES OF
RAPIDLY SOLIDIFIED Al-Fe-V-Si ALLOY

A THESIS SUBMITTED TO
THE GRADUATE SCHOOL OF NATURAL AND APPLIED SCIENCES
OF
THE MIDDLE EAST TECHNICAL UNIVERSITY

BY

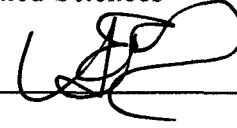


SUAT KEMAL ANGI

IN PARTIAL FULFILLMENT OF THE REQUIREMENTS FOR THE DEGREE
OF
MASTER OF SCIENCE
IN
THE DEPARTMENT OF METALLURGICAL AND MATERIALS ENGINEERING

DECEMBER 1997

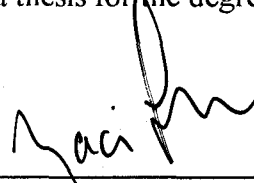
Approval of the Graduate School of Natural and Applied Sciences



Prof. Dr. Tayfur Öztürk

Director

I certify that this thesis satisfies all the requirements as a thesis for the degree of
Master of Sciences.



Prof. Dr. Naci Sevinç

Head of Department

This is to certify that we have read this thesis and that in our opinion it is fully
adequate, in scope and quality, as a thesis for the degree of Master of Sciences.



Assoc. Prof. Dr. Ali Kalkanlı

Supervisor

Examining Committee Members

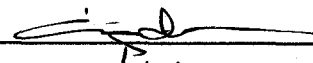
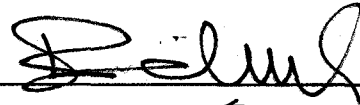
Prof. Dr. Ekrem Selçuk

Assoc. Prof. Dr. Bilgehan Ögel

Assoc. Prof. Dr. Rıza Gürbüz

Assoc. Prof. Dr. Çiğdem Erçelebi

Assoc. Prof. Dr. Ali Kalkanlı



ABSTRACT

MICROSTRUCTURE AND HIGH TEMPERATURE PHASE STUDIES OF RAPIDLY SOLIDIFIED Al-Fe-V-Si ALLOY

Angi, Suat Kemal

M.S., Department of Metallurgical and Materials Engineering

Supervisor: Assoc. Prof. Dr. Ali Kalkanlı

December 1997, 124 pages.

In this study, microstructure and high temperature phase analysis of rapidly solidified Al-Fe-V-Si alloys were investigated. For this purpose, a series of commercial aluminum alloys designed for high temperature strength application were prepared and then solidified rapidly in flake and ribbon form by melt spinning technique. The average thickness' of the resulting ribbons were in the range of 30 to 250 μm and the corresponding cooling rates were about 10^5 - 10^7 $^\circ\text{C}/\text{sec}$. These as-cast products were then heat treated at the temperature range of 150 to 500 $^\circ\text{C}$ for 1-3 hours. The melt-spun ribbons were examined by X-ray Diffractometer, Scanning Electron Microscope (SEM) and Transmission Electron Microscope (TEM) for phase analysis and microstructural morphology at both as-cast and heat treated conditions.

Examinations of the melt-spun ribbons revealed that the very fine dispersoids which are uniformly distributed throughout the aluminum matrix in high volume fraction are stable at as-cast and heat treated conditions. In addition, rapidly solidified Al-Fe-V-Si alloys have characteristically cellular type morphology and the nearly spherical second phase particles (silicide dispersoids) decorate the aluminum cell boundaries.

Keywords: High temperature stability, rapid solidification, Al-Fe-V-Si alloy, solid solubility extension, dispersoids.



ÖZ

HIZLI SOĞUTULMUŞ Al-Fe-V-Si ALAŞIMININ MİKROYAPI VE YÜKSEK SICAKLIK FAZ ÇALIŞMASI

Angı, Suat Kemal

Yüksek Lisans, Metalurji ve Malzeme Mühendisliği Bölümü

Tez Yöneticisi: Doç. Dr. Ali Kalkanlı

Aralık 1997, 124 sayfa

Bu çalışmada, hızlı soğutulmuş Al-Fe-V-Si alaşımlarının mikroyapısı ve yüksek sıcaklıktaki faz analizi araştırılmıştır. Bu amaçla öncelikle, yüksek sıcaklık uygulamaları için geliştirilmiş olan Al-Fe-V-Si ticari alaşımları hazırlanmış ve bu alaşımlardan eriyik savurma yöntemi ile hızlı katılaşmış şeritler elde edilmiştir. Ortalama kalınlıkları 30 ile 100 μm arasında değişen bu şeritler 10^5 - 10^7 $^\circ\text{C}/\text{sn}$ gibi çok yüksek soğuma hızlarında katılaşmıştır. Daha sonra bu şeritler üzerinde 150 ile 500 $^\circ\text{C}$ sıcaklıkları arasında 1 ile 3 saat için ısıl işlem uygulanmıştır. Çalışılan alaşımların faz analizinin yapılabilmesi ve şekilsel olarak tanımlanabilmesi amacıyla hızlı katılaştırılmış şeritler, X-ray Difraktometresi, Taramalı Elektron Mikroskobu (SEM) ve Geçirimli Elektron Mikroskobu (TEM) ile test edilmiştir. İncelemeler sonucunda, alüminyum

matris fazın içine düzenli şekilde saçılmış olan fazın yüksek hacim yoğunluğunda ve çok küçük boyutta olduğu görülmüş ve bu saçılmış fazın yüksek sıcaklıkta kararlılığını koruduğu anlaşılmıştır. Buna ek olarak, Al-Fe-V-Si alaşımının yüksek katılma hızları ile hücresel biçimde katılaştığı ve ikinci fazı oluşturan küresel küçük tanelerin alüminyum hücre sınırlarına yerleştiği belirlenmiştir.

Anahtar Kelimeler: Yüksek sıcaklık kararlılığı, hızlı katılma, Al-Fe-V-Si alaşımı, katı çözünürlük artışı, saçılmış faz.



ACKNOWLEDGEMENTS

I would like to thank to Assoc. Prof. Dr. Ali Kalkanlı for his valuable supervision and guidance throughout this research.

I am also grateful to Dr. Alp Alanyalıođlu for his valuable discussions and suggestions during this study.

Thanks for the valuable help provided during the alloy preparation and melt spinning experiments of the foundry laboratory technicians and also all technical stuff of the Metallurgical and Materials Engineering Department.

I am thankful to Elif Tarhan for the valuable and careful work performed for TEM specimen preparation and examination and to Cengiz Tan for the SEM examination and analysis.

Finally, I wish to thank to my family and friends for their encouraging and patience.

TABLE OF CONTENTS

ABSTRACT	iii
ÖZ	v
ACKNOWLEDGEMENTS	vii
TABLE OF CONTENTS	viii
LIST OF TABLES	xi
LIST OF FIGURES	xii

CHAPTER

1. INTRODUCTION	1
2. THEORY	4
2.1 Rapid Solidification Powder Processing	4
2.2 Formation of Uniform Ribbons By Melt Spinning Technique	8
2.2.1 Description of The Process	8
2.2.2 Solidification Models For Ribbon Formation	11
2.2.3 Heat transfer Formulation in Melt Spinning Process	13
2.2.4 Uniformity of Metal Ribbons	15
2.2.4.1 Effect of Reservoir On Ribbon Uniformity	17
2.2.4.2 Effect of Nozzle Geometry On Ribbon Uniformity	17
2.2.4.3 Cylindrical Jet Stability	18

2.2.4.4	Puddle Stability And Puddle (Ribbon) Shape	22
2.2.4.5	Ribbon Dimensions	26
2.3	Rapid Solidification of Aluminum Alloys	28
2.3.1	High Temperature Aluminum Alloys	29
2.3.2	Rapidly Solidified Al-Fe-V-Si Alloys.....	34
3.	EXPERIMENTAL PROCEDURE	45
3.1	Melt Spinning Apparatus	45
3.2	Alloy Preparation, Casting and Heat Treatment Conditions	48
3.3	X-Ray Diffractometer (XRD)	50
3.4	Scanning Electron Microscopy (SEM)	50
3.5	Transmission Electron Microscopy (TEM)	51
4.	DISCUSSION AND RESULTS	52
4.1	Characterization of Melt-Spun Flakes and Ribbons	52
4.1.1	Flake Formation and Pressure	52
4.1.2	Flake Formation and Wheel Speed	54
4.1.3	Effect of Process Parameters on Ribbon Dimensions and Uniformity	54
4.1.4	Planar Flow Casting (PFC)	59
4.1.5	Surface Analysis of Melt-Spun Ribbons	61
4.1.6	Cooling Rates of Melt-Spun Ribbons	66
4.2	X-Ray Diffraction Study	67
4.2.1	Indexing Pattern of Unknown For Cubic Crystals	69

4.3 SEM Study	80
4.3.1 Chemical Compositions of Studied Alloys	80
4.3.2 Microstructural Refinement by Rapid Solidification	80
4.3.3 Microstructural Examination of Melt-Spun Flakes and Ribbons	82
4.3.4 Solubility Limit	89
4.4 TEM Study	92
4.4.1 Effect of Cooling Rate on Cell and Particle Size	93
4.4.2 Effect of Cooling Rate on Chemical Homogeneity	96
4.4.3 Effect of Cooling Rate on Solubility Extension of Alloying Elements	98
4.4.4 Identification of Quasi-crystalline Icosahedral Phase	101
4.4.5 Effect of Heat Treatment on Microstructure of RS Al-Fe-V-Si Alloy	104
4.4.6 Indexing Diffraction Patterns of Silicide Particles	108
5. CONCLUSIONS AND FUTURE WORKS	111
5.1 Conclusions	111
5.2 Future Works	114
REFERENCES	115
APPENDICES	
A. XRD PATTERN OF THE MELT-SPUN FLAKE	119
B. EQUATIONS, FILE CARDS AND MILLER INDICES RELATIVE TO XRD STUDY	121

LIST OF TABLES

TABLE

2.1	Comparison of two RSP powder techniques	6
2.2	Transport properties of some metallic melts	13
2.3	Diffusivity, liquid and solid solubility of some transition metals in Al	29
2.4	Nominal composition of rapidly solidified Al-Fe-V-Si alloys and their product forms	35
3.1	Alloy preparation charge calculation table	48
4.1	Effect of pressure on ribbon dimensions and flow rate in PFC	61
4.2	Indexing x-ray patterns of the RS Al-Fe-V-Si alloy (#2) as-cast and heat-treated conditions	68
4.3	Chemical compositions of studied RS Al-Fe-V-Si alloys in as-cast conditions	80
4.4	Effect of ribbon thickness on cell and particle size	93
4.5	Lattice parameter calculation for ordered BCC silicide particles	110
A.1	XRD pattern obtained from the computerized x-ray diffractometer with CuK_α radiation for the melt-spun flake	120
B.1	Plane spacing equations for following crystal structures	122
B.2	File card 4-0787 for aluminum	123
B.3	Quadratic forms of Miller indices	124

LIST OF FIGURES

FIGURES

1.1	Comparison of advanced aluminum alloys and titanium alloys for impeller application	3
2.1	Schematic diagram of a RS powder process based on planar flow casting ribbon comminution	7
2.2	Schematics of chill block melt spinning casting	8
2.3	The solidification of the liquid alloy arriving on the melt-spinning substrate	10
2.4	Substrate-induced shearing of the undercooled viscous liquid layer	11
2.5	Schematic description of chill block casting. Velocity profiles in the melt puddle (a), and corresponding stream line patterns (b)	11
2.6	A cylindrical liquid-metal jet of radius R_j and velocity V_j impinges on a substrate moving at a velocity V_s and forms a liquid puddle of radius R_p	16
2.7	Standing capillary wave of wavelength λ on the liquid metal jet of radius R_j	20
2.8	Casting instabilities	21
2.9	The projections of the intersection line of the puddle, jet and ribbon with the moving substrate	23

2.10 Lateral cross sections of the ribbons pulled from puddles of circular, rectangular and ellipsoidal shapes	25
2.11 Relationship of quench rate of ribbon thickness and substrate character	27
2.12 X-ray diffractogram of the (Al-5.3% Mn) melt-spun ribbon	32
2.13 A comparison of coarsening rates of dispersoids in various rapidly solidified Al-TM alloys. r is the average particle size at time t	33
2.14 A comparison of elevated temperature tensile yield strength of various high temperature aluminum alloys and standart aerospace aluminum alloys	33
2.15. Microstructures of RSP Al-8Fe-1V-2Si alloys (a) in as-quenched melt-spun ribbon and (b) after extrusion at 375 °C	37
2.16 Corrosion performance of alloy FVS0812 in a salt fog envirement	38
2.17 TEM micrographs of RS Al-Fe-V-Si alloys	41
2.18 The XRD patterns of RS Al-Fe-V-Si alloys	41
2.19 Different orientation diffraction patterns from a quasi-crystals of RS Al-Fe-V-Si alloys	41
2.20 Bright field image of Al-Fe-V-Si alloy in as-extruded condition and diffraction pattern of the structure	42
2.21 TEM bright field micrograph showing growth morphology of isosahedral phase surrounded by crystalline ring	43
2.22 SADPs of silicide grains from regions A and B of Figure 2.21 corresponding to zone $[\bar{1}22]$ axes	44
3.1 Melt-spinning set up	46

3.2	Graphite crucibles for melt-spinning	47
3.3	The crucible is being heated for casting	47
3.4	The ribbon formation by melt spinning technique	50
4.1	Melt-spun flakes with irregular shapes	53
4.2	Ribbons with about 3 mm in width	55
4.3	Ribbons with several lengths	55
4.4	Ribbon with 30 μm in thickness in entire length	56
4.5	A uniform ribbon obtained in a single piece with about 3 meters in length	57
4.6	Schematic description of the positions of crucibles over the spinning wheel for two castings	58
4.7	Effect of pressure on ribbon dimensions and surface texture in PFC	60
4.8	Two distinct surfaces of a melt-spun ribbon	62
4.9	Flow pattern of free surface of a ribbon showing accumulated particles and elliptical lines along its entire length	64
4.10	A free surface flow pattern showing turbulent spots produced by the orifice edges spreaded through the both sides of the central laminar flow	65
4.11	The effect of temperature on lattice parameter of Al from the melt-spun ribbons of Al-Fe-V-Si alloy (#2)	71
4.12	X-ray diffractogram from melt-spun flake of Al-Fe-V-Si alloy (# 1) in as-cast condition	72
4.13	X-ray diffractogram from melt-spun ribbon of Al-Fe-V-Si alloy (#2) in as-cast condition	73

4.14	X-ray diffractogram from melt-spun ribbon of Al-Fe-V-Si alloy (#2) in heat-treated condition at 200 °C for 1 hour	74
4.15	X-ray diffractogram from melt-spun ribbon of Al-Fe-V-Si alloy (#2) in heat-treated condition at 300 °C for 1 hour	75
4.16	X-ray diffractogram from melt-spun ribbon of Al-Fe-V-Si alloy (#2) in heat-treated condition at 400 °C for 1 hour	76
4.17	X-ray diffractogram from melt-spun ribbon of Al-Fe-V-Si alloy (#2) in heat-treated condition at 500 °C for 1 hour	77
4.18	X-ray diffractogram from melt-spun ribbon of Al-Fe-V-Si alloy (#3) in as-cast condition	78
4.19	X-ray diffractogram from melt-spun ribbon of Al-Fe-V-Si alloy (#4) in as-cast condition	79
4.20	SEM micrograph from conventional cast ingot of Al-Fe-V-Si alloy	81
4.21	SEM micrograph from melt-spun ribbon showing variation in microstructure from the chill (C) and the air (A) side	82
4.22	SEM micrograph from melt-spun flake in as-cast condition showing fine and uniformly distributed second phase particles in Al matrix	83
4.23	SEM micrograph from melt-spun flake in heat treated at 200 °C for 1.5 hours showing fine and uniformly distributed second phase particles in Al matrix	83
4.24	SEM micrograph from melt-spun flake in heat treated at 500 °C for 1 hour showing fine and uniformly distributed second phase particles in Al matrix	84

4.25 SEM micrograph from melt-spun flake in heat treated at 500 °C for 3 hours showing fine and uniformly distributed second phase particles in Al matrix	84
4.26 SEM micrograph from melt-spun ribbon in as-cast condition showing fine and uniformly distributed second phase particles in Al matrix	85
4.27 SEM micrograph from melt-spun ribbon in heat treated at 400 °C for 1 hour showing fine and uniformly distributed second phase particles in Al matrix	85
4.28 SEM micrograph from melt-spun ribbon in heat treated at 500 °C for 1 hour showing fine and uniformly distributed second phase particles in Al matrix	86
4.29 EDS analysis of the melt-spun flake indicated in Figure 4.22	87
4.30 EDS analysis of the melt-spun flake indicated in Figure 4.26	87
4.31 EDS analysis of the melt-spun flake indicated in Figure 4.27	88
4.32 EDS analysis of the melt-spun flake indicated in Figure 4.28	88
4.33 SEM micrograph from the melt-spun ribbon of the alloy #4	90
4.34 EDS analysis of the white points indicated in Figure 4.33	91
4.35 Bright field image showing uniform microcellular structure from as-cast melt-spun ribbon 30 μm in thickness obtained from the alloy #2 (x 43500)	94
4.36 Bright field image showing uniform microcellular structure from as-cast melt-spun ribbon 30 μm in thickness obtained from the alloy #2 (x 72000)	94

4.37	Bright field image from as-cast melt-spun ribbon 98 μm in thickness obtained from the alloy #2 (x 40600)	95
4.38	Bright field image from as-cast melt-spun ribbon 250 μm in thickness obtained from the alloy #4 (x 72000)	95
4.39	Effect of ribbon thickness on average cell and particle size	96
4.40	Bright field image showing cellular and eutectic type structure together from as-cast melt-spun ribbon 250 μm in thickness obtained from the alloy #4 (x 43500)	97
4.41	Bright field image showing cellular and eutectic type structure together from as-cast melt-spun ribbon 250 μm in thickness obtained from the alloy #4 (x 26300)	97
4.42	TEM bright field micrograph shows that vanadium rich precipitates and silicide dispersoids are coexist at the cell boundaries (x 54000)	99
4.43	TEM dark field image of Figure 4.42. Vanadium rich precipitates and silicide dispersoids can be seen together at the cell boundaries (x 54000)	100
4.44	Diffraction pattern of vanadium rich precipitates	100
4.45	Diffraction pattern of silicide dispersoids	101
4.46	TEM bright field image showing randomly oriented large granular (hexagonal) particles (x 43500)	103
4.47	TEM dark field image of Figure 4.46 (x 43500)	103
4.48	Diffraction pattern of randomly oriented granular (hexagonal) particles	104
4.49	TEM bright field image showing common microstructure from the melt-spun ribbon heat treated at 300 $^{\circ}\text{C}$ for 1 hour (x 28500)	105

4.50	TEM bright field image showing granular (hexagonal) particles from the melt-spun ribbon heat treated at 300 °C for 1 hour (x 43500)	106
4.51	TEM bright field image showing common microstructure from the melt-spun ribbon heat treated at 400 °C for 1 hour (x 43500)	106
4.52	TEM bright field image showing common microstructure from the melt-spun ribbon heat treated at 500 °C for 1 hour (x 43500)	107
4.53	TEM bright field image showing a network of silicide dispersoids from the melt-spun ribbon heat treated at 300 °C for 1 hour (x 28500)	107
4.54	Transmission electron diffraction patterns of silicide particles corresponding to zone [100], [012] and [113] axis'.	109
4.55	TEM bright field micrograph showing microdiffraction region for a silicide particle.	110

CHAPTER 1

INTRODUCTION

Rapid solidification processing has become a unique technology in material science and engineering during the last two decades. The major benefits of rapid solidification can be summarized as follows:

1. grain size decreases
2. chemical homogeneity increases
3. extension of solid solubility increases
4. formation of metastable crystal structures
5. formation of metallic glasses

The criterion for rapid solidification is somewhat ill-defined, but usually means the temperature of the molten material is reduced to some value well below the freezing point in a very short time, usually milliseconds. For the rapid solidification of about 10^5 to 10^7 °C/s, The Chill Block Melt Spinning (CBMS) and Planar Flow Casting (PFC) techniques and how to obtain uniform melt-spun ribbons by these processes will be discussed in this study.

Rapid solidification ribbon casting technology with subsequent comminution of ribbon to powder has allowed the development of a series of aluminum-iron-vanadium-silicon alloys which combine good high temperature strength, ductility, fatigue and fracture toughness for the aircraft structural applications since the early of 1980's [23]. Rapidly solidified (RS) Al-Fe-V-Si alloys also exhibit high moduli, excellent thermal stability and corrosion and oxidation resistances [14, 24]. High temperature Al-Fe-V-Si alloys have consequently the potential to replace Ti aircraft structure materials for operating in the 149 to 339°C temperature range. Substitution of RS Al-Fe-V-Si alloys for titanium alloys offers the significant benefits of:

- saving in material and fabrication costs,
- reduction in component weights, and
- reduction in component rotating inertia [42]. (see Figure 1.1)

The achievement of strength at high temperatures for RS aluminum alloys requires thermally stable dispersoids in Al matrix. These dispersoids should be include the elements with low solubility and diffusivity in aluminum, and with a spherical morphology. Transition metal elements of Fe and V satisfy this requirements. The RS Al-Fe-V-Si alloys consist of very fine, nearly spherical $Al_{12}(Fe,V)_3Si$ (silicide) dispersoids formed during rapid solidification. This silicide phase has a BCC structure and no tendency for the formation of needle or plate-like precipitates which degrade alloy ductility and fracture toughness. These very fine, nearly spherical silicide dispersoids are uniformly distributed throughout the aluminum matrix in high volume fractions and have excellent thermal stability

because of their much slower coarsening rates [14]. Although the dispersoids are noncoherent, some of coherency is obtained due to their cubic crystal structure for these alloys. In all practical alloys of the aluminum-transition metals systems, rapid solidification produces either crystalline cellular-dendritic, microeutectic or quasicrystalline icosahedral solidification structures [16].

In this study, the discussion is limited primarily to define the microstructure of the melt-spun ribbons with several Al-Fe-V-Si alloy compositions and thickness'. In addition, some variations observed in the microstructure depending on the alloy composition and ribbon thickness will also be discussed.

- OBJECTIVE:
 - EXTEND USE OF ALUMINUM ALLOYS
- PAYOFFS:
 - REDUCTION IN:
 - WEIGHT
 - INERTIA
 - COST

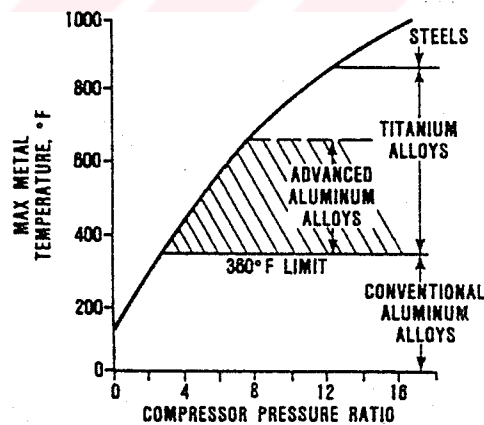


Figure 1.1 Comparison of advanced aluminum alloys and titanium alloys for impeller application. [42]

CHAPTER 2

THEORY

2.1 Rapid Solidification Powder Processing

Rapid solidification has developed and attracted increasing interest in a few decades. The normal two-phase mixture of equilibrium phases in a eutectic alloy could be replaced by an extended solid solution, a new non equilibrium crystalline phase, or, most remarkably, by a noncrystalline phase (a metallic glass), quite simply by quenching with sufficient rapidity from the liquid state [1].

Rapid solidification has some of the particular attractions compared with conventional solidification. By rapid quenching from the melt, a high degree of microstructural refinement (decreasing grain size, increasing chemical homogeneity, decreasing segregation), extended solubilities of alloying elements, and elimination of complex constituent phases (formation of metastable non equilibrium crystal structures) can be obtained. In addition, rapid solidification eliminates the redundant working and finishing operations involved in ingot processing and provides

obtaining the near net shape products (e.g., foils, sheets, and ribbons) which have potential economic advantage by direct melt processing [1, 2].

The most commercially rapid solidification processing (RSP) powder techniques fall into two main categories: atomization (both high pressure and centrifugal gas atomization) and melt spinning-ribbon comminution [16].

The refinement of the structure is directly related to the cooling rate from the melt. In the case of atomized powder this is related to the particle size and particle velocity: the finer the particle size, the higher the solidification rate. In atomization processes to maximize the heat transfer coefficient- h_f and obtain finer powder particles, gas atmospheres are sharply limited both in terms of conductivity and cost. Nitrogen and argon are the most preferred gases.

For solidification rates greater than about 10^4 K/s metal substrate quenching must be used rather than atomization techniques. In this case high cooling rates are based on substrate conductivity and ribbon thickness. It is obvious that a solid substrate such as copper has a many orders of magnitude higher thermal conductivity than that of a gas and as a result of this fact the higher cooling rates exists for solid substrate cooling. The highest solidification rates attainable by the several techniques are as the following [2]:

Melt Spinning: 10^5 K/s at 30 to 60 μm thickness. Primarily ribbon shapes.

Melt Extraction: 10^5 K/s at 30 to 60 μm thickness. Ribbon plus other particulate shapes.

Twin Roller: 10^6 K/s at 30 to 100 μm thickness; higher for thinner splats. Flakes and foils of irregular shape.

Piston and Anvil: 10^6 K/s at 60 to 120 μm thickness. One large circular flake.

Gun: 10^6 to 10^9 K/s at 10 μm down to 0.1 μm thickness. Very fine flakes of irregular shape.

The first two are single-substrate methods; the next two are two surface methods; and the last is a single-surface technique [2] which requires flake thickness as fine as 0.1 to 1 μm to achieve quench rates of 10^8 to 10^9 K/s.

Table 2.1 shows a brief comparison of some of the key parameters of the two basic processes [16].

Table 2.1 Comparison of two RSP powder techniques

	Atomization	Planar flow casting- ribbon comminution
Cooling rate	$< 10^4 \text{ K}^{-1}$	$> 10^5 \text{ K}^{-1}$
Atmosphere	Inert atmosphere	Carried out in air
Morphology	Nearly spherical	Irregular flakes
Microstructural uniformity	Limited to finest particle sizes	Uniform, irrespective of particle size
Economics	Depends on atomization process used	Low cost
Safety	Extreme precaution needed in handling of fine (~ 325 mesh) powder	Less hazard associated with coarse (~ 30 mesh) powder particulate

During the subsequent thermomechanical processing, of course, that refined microstructure achieved by rapid solidification must not be altered. In order to take advantage of RPS for fabricating structural components, clever alloy design is necessary. In alloy systems with high volume fractions of ultrafine dispersed phases, dispersoids in rapidly quenched particulates are stable and do not coarsen appreciably during subsequent processing. Since the grain sizes of as-quenched microcrystalline alloys are usually extremely fine, stable dispersoids, they inherently pin the grain boundaries and prevent the coarsening during high temperature consolidation.

The principles of such type dispersion strengthening mechanism will be discussed in section 2.3 for specific high temperature Al-Fe-V-Si aerospace alloy.

Figure 2.1 shows a schematic diagram of a RSP powder metallurgy process currently in practice to produce tonnage quantities of Al-TM (TM=transition metals) alloys [16].

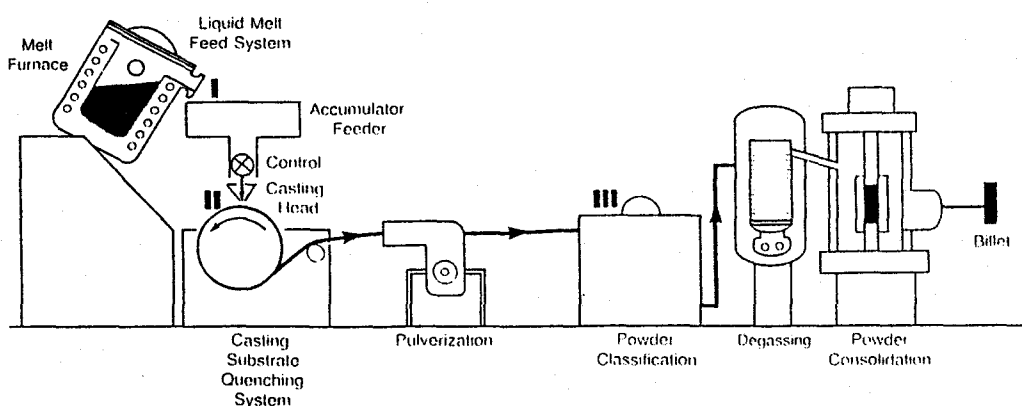


Figure 2.1 Schematic diagram of a rapid solidification powder process based on planar flow casting ribbon comminution, as practiced by Allied-Signal Inc.

2.2 Formation of Uniform Ribbons By Melt Spinning Technique

2.2.1 Description of The Process

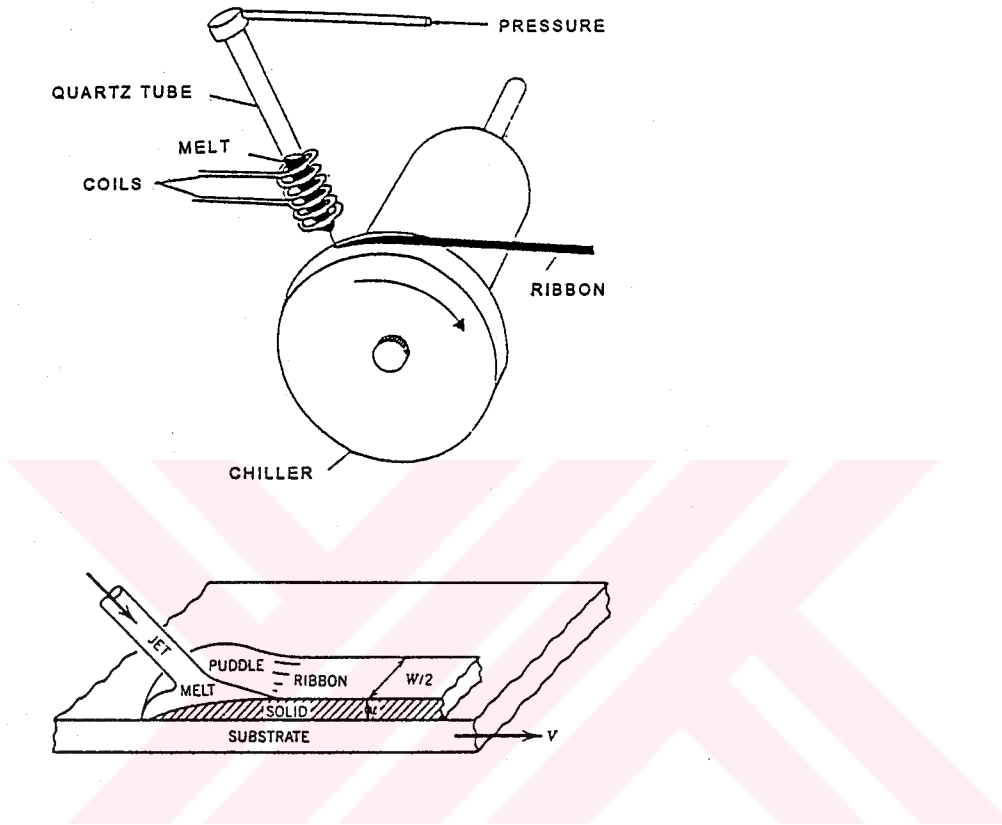


Figure 2.2 Schematics of chill block melt spinning casting.

The method had been developed by R.B. Pond [3, 4] whereby continuous ribbons or fibers could be solidified. This continuous process, which is called Chill Block Melt Spinning (CBMS), is very simple and involves the ejection of a molten metal jet onto a rapidly rotating, polished, cold, conductive (most frequently copper drum) cylindrical surface (Figure 2.2). In this process the molten metal or alloy which is melted in a crucible and then ejected through a small orifice by gas pressure or gravity impinges on the surface of a rapidly rotating wheel where the melt solidifies

and a continuous ribbon is formed. The molten jet may be inclined at an angle to the tangent plane of the chill/wheel surface and spreads into a puddle of width w . The chill surface moving a velocity creates a ribbon of thickness t , whose width is the same as the width of the puddle. The velocity of the chill surface is generally about 10-50 m/sec. The rotating wheel is invisible with the exception of the slight reflections on its polished surface. The time of exposure is 1 millisecond throughout experiments [5]. The very high quenching rates (about 10^6 K/s) are achieved and that the high degree of quenching rates in many cases allow alloys to freeze in the disordered state, i.e. to form a metallic glasses.

The crucial point in this process is the impingement of the jet on the wheel and the ribbon formation. As pointed out by several authors [6-8], a stationary melt puddle is formed as an intermediate state between the molten jet and the solidified ribbon layer (Figure 2.2, 2.3). The shape of the puddle is formed under the counteracting forces of tangential flow of the material and of the surface tension. In the analysis of the casting process [9], the flow in the puddle is generally assumed to be laminar. But the melt in the vicinity of the liquid solid transition layer (Figure 2.3, 2.4) is subjected to very high shear and the Reynold's number- Re characterizes the liquid flow is either laminar or turbulent. If the turbulent flow develops in a melt puddle, several type of instability can occur which will be discussed later.

Yavari *et al* [9] said that the liquid is sheared at a rate during cooling by a rapidly moving metal surface. As in Figure 2.3, the liquid layer solidified on the

substrate leaves the melt puddle along the x direction with the velocity of substrate ($V_x=V_R=V_S$), while for the melt arriving in the puddle the melt velocity is equal to zero ($V_x=0$). As the ribbon moves beneath the stationary melt puddle, solidification continuous and the solid-liquid interface penetrates the liquid puddle along z (normal to the substrate) until the solidified ribbon leaves the puddle. It is suggested that such a stable melt puddle also maximizes the quenching rates [7, 8].

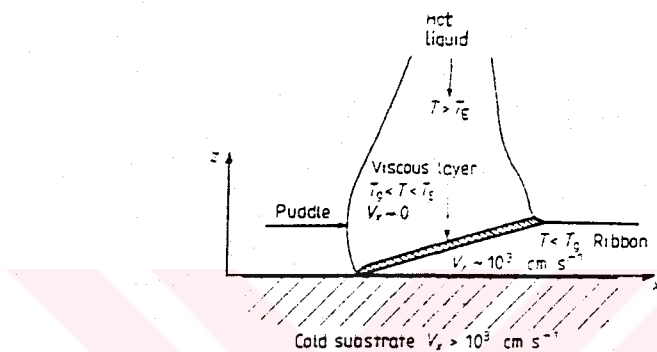


Figure 2.3 The solidification of the liquid alloy arriving on the melt-spinning substrate.

According to Zielinski *et al* [10], there are two limiting cases depending on the distance between the nozzle orifice and the wheel surface that is length of the jet L_j . If this distance is large compared to the jet diameter, the jet can be treated as a free flow. In the preparation of most ribbon formation, however, the distance is so small that the nozzle limits the height of the melt puddle. Fluid elements close to the nozzle have a lower energy than those close to the wheel surface and they are slowed down by the pressure gradient to the point where flow direction is reversed. Figure 2.5 displays the description of this process. In the experiment which is described by

Figure 2.5, the crucible is positioned 0.5 to 0.6 mm above the substrate and note that the molten jet is absent.

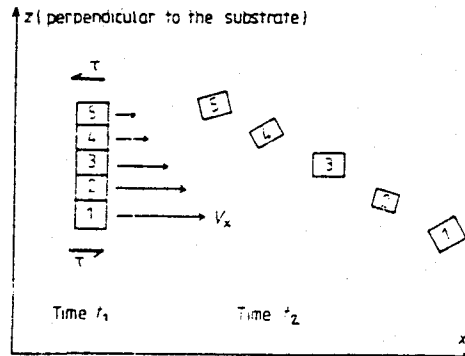


Figure 2.4 Substrate-induced shearing of the undercooled viscous liquid layer. [9]

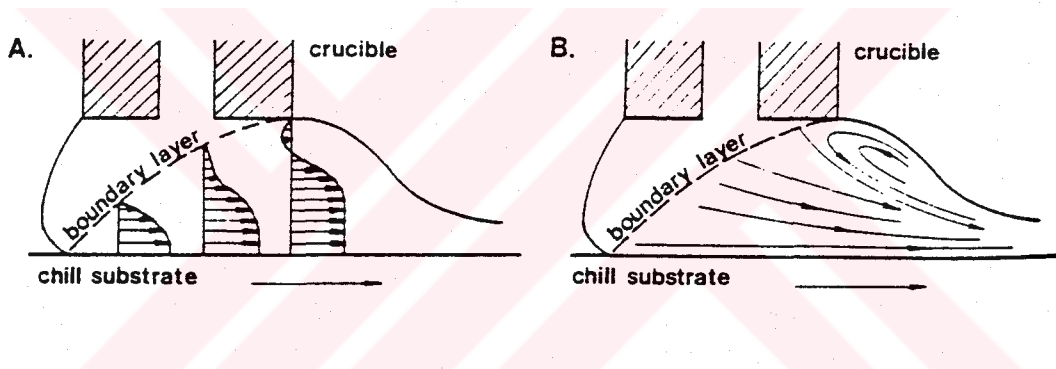


Figure 2.5 Schematic description of chill block casting. Velocity profiles in the melt puddle (a), and corresponding stream line patterns (b).

2.2.2 Solidification Models For Ribbon Formation

The liquid puddle is visualized as consisting a boundary layer zone in which the thermal and momentum effects of the chill surface are strongly felt and an outer zone where the effects of the chill surface have not yet penetrated.

According to the first analysis on CBMS by Kavesh [7], there are possible two transport mechanisms which control the ribbon formation and determine the final ribbon dimensions.

If thermal transport is much faster than momentum transport, a solid boundary layer will form adjacent to the chill surface and propagate into the melt puddle to form the ribbon. In this case ribbon thickness results entirely from solidification over the puddle length l . (Figure 2.3) Thus, ribbon thickness increases with the puddle length through the residence (dwell) time θ_r , and it may be defined as $t \sim l/V_s$. It is apparent that substrate velocity controls both l and t [12]. The puddle length increases with decreasing roll velocity and becomes more sensitive to instabilities which will be mentioned about later. For low substrate velocities ($V_s=10$ m/s), however, the melt puddle is no longer stable and no continuous ribbons can be produced. Also, the resulting ribbon is irregular in shape and very often crystallization of material takes place [5].

Whereas, when the momentum transport mechanism dominates the process, a liquid boundary layer will be dragged out of the melt puddle by the moving substrate. In this case, the ribbon is extracted from the puddle entirely as liquid and solidifies farther downstream.

Determination of which of the limiting cases is dominant throughout the process is based on the transport properties of the melt. On the basis that the Prandtl number for molten metals is large, Kavesh proposed that the thermal boundary layer

would propagate much more rapidly than the momentum boundary layer. The depth of penetration of thermal and momentum effects in a fluid near a solid boundary is given by [7]

$$\delta_T/\delta_M \sim (\text{Pr})^{-1/2} \dots\dots\dots (1)$$

where Pr is the Prandtl number of the fluid,

$$\text{Pr} = C_p\mu/k \text{ (dimensionless)}$$

δ_T = thermal boundary layer thickness (cm)

δ_M = momentum boundary layer thickness (cm)

Table 2.2 shows the transport properties of some metallic melts.

Table 2.2 Transport Properties of Some Metallic Melts

Metal	T, °C	C _p , cal / g-°C	μ, poise	k, cal / sec-cm-°C	Pr	Pr ^{-1/2}
Aluminum	600	0.259	0.029	0.247	0.0304	5.7
	1000	0.259	0.014	0.290	0.0125	8.9
Tin	300	0.058	0.019	0.08	0.0138	8.5
Zinc	450	0.12	0.032	0.138	0.0278	6.0
Iron	1600	0.189	0.056	0.075	0.141	2.7
Fe ₄₀ Ni ₄₀ P ₁₄ B ₆ 3.6		1000	0.13	~ 0.03	0.05	0.078

2.2.3 Heat Transfer Formulation in Melt Spinning Process

Basic one dimensional heat transfer due to conduction in the solidified layer can be written as:

$$q = k (T_m - T_s) / t \dots\dots\dots (2)$$

where k is thermal conductivity, T_m is solidification temperature, T_s is the absolute interface temperature and t is the thickness of solidified layer.

The heat transfer at the solidifying metal-spinning wheel interface by convection can be defined as:

$$q = h_i (T_s - T_w) \dots\dots\dots (3)$$

where T_w is the substrate temperature and h_i is the heat transfer coefficient across the wheel/strip interface.

Heat transfer by radiation from free surface of the strip can be described by Stefan's Law :

$$q = A \sigma_s \varepsilon (T_{sur}^4 - T_0^4) \dots\dots\dots (4)$$

where σ_s is the Stefan's constant ($= 5.67 \times 10^{-8} \text{ W/m}^2\text{K}^4$), ε is emissivity (0.15-1) and A is the radiating area, T_{sur} is the free surface temperature, T_0 is the ambient temperature of the surroundings.

The basic relation for one dimensional heat flow by conduction within the strip and the substrate can be written as:

$$\frac{\partial T}{\partial \theta} = \alpha \frac{\partial^2 T}{\partial y^2} \dots\dots\dots (5)$$

where T is temperature function of distance (y) through the thickness from the strip/wheel interface, θ is the time variable and α is the solid thermal diffusivity. An analytic expression of Equation 5 can be obtained for non-Newtonian conditions,

allowing for temperature gradients through the strip thickness but neglecting temperature gradients within the wheel. Under Newtonian cooling conditions, temperature gradients through the thickness and chiller are negligible and heat removal from the strip controlled by resistance to heat flow across the strip/wheel interface. The average strip temperature decays exponentially with time:

$$T - T_w = (T_i - T_w) \exp\left(\frac{-h_i \theta}{t \rho C_p}\right) \dots\dots\dots (6)$$

where θ is time and T_i is the initial strip temperature at $\theta = 0$, where the strip is fully liquid at time $\theta = 0$, the initial deposit thickness is equal to zero. ρ is the density and C_p is the specific heat capacity of the strip.

In addition, at the strip/wheel interface the rate of heat extraction is given by following boundary condition:

$$-k (dt/dy) = h_i (T - T_w) \dots\dots\dots (7)$$

Left hand side of Equation 6 is the heat extraction in the solidified layer by conduction and right hand side of it the heat transfer at the strip/wheel boundary layer by convection.

2.2.4 Uniformity of Metal Ribbons [8]

A metal ribbon made in this manner usually exhibits undesirable dimensional variations both across and along the major axis of the ribbon. Although the elimination of all dimensional variability of the ribbon would be difficult, such

variability can be limited by paying close attention to the factors that generate ribbon nonuniformity.

When a ribbon is solidified, the dimensions of the ribbon are fixed. Thus it is logical to look for the sources of ribbon nonuniformities in unsteadiness of the liquid puddle and liquid jet upstream (Figure 2.6).

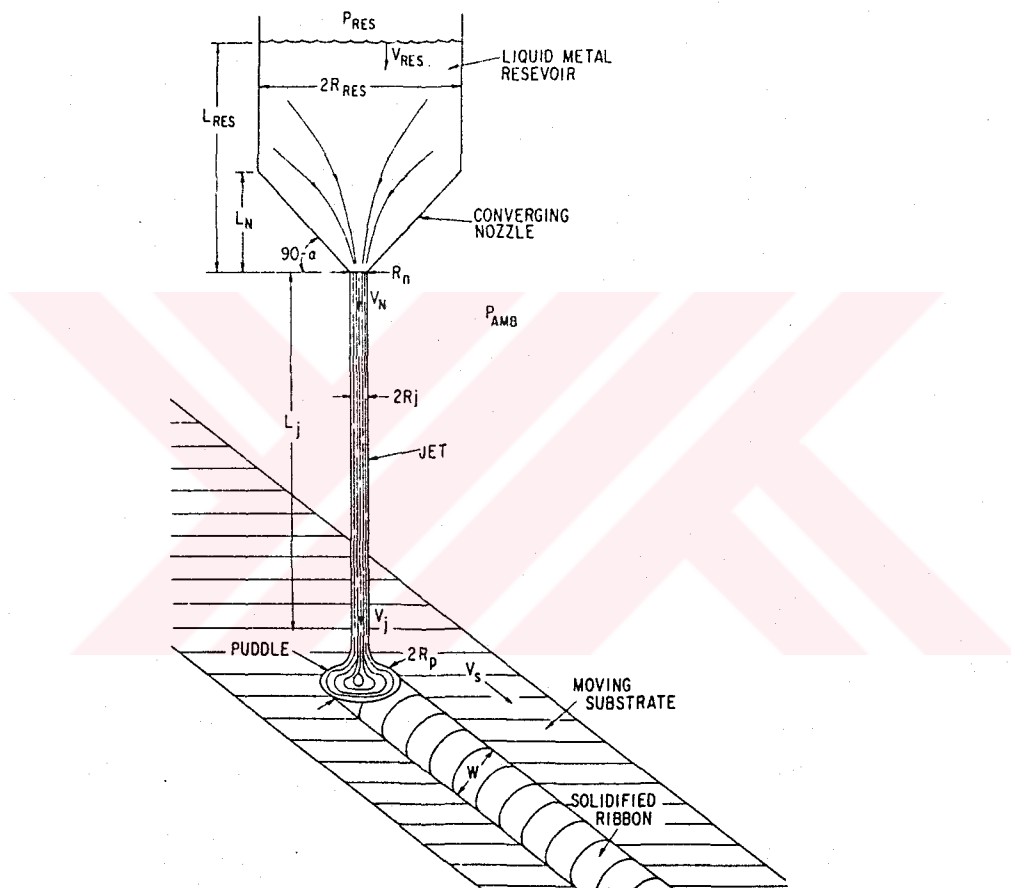


Figure 2.6 A cylindrical liquid-metal jet of radius R_j and velocity V_j impinges on a substrate moving at a velocity V_s and forms a liquid puddle of radius R_p . A solid ribbon of width W is pulled from the puddle by the cold moving substrate. The reservoir is separated from the moving substrate by a distance L_j .

2.2.4.1 Effect of Reservoir On Ribbon Uniformity

Because of the conservation of matter, the mass of liquid material leaving the nozzle of the reservoir per unit time, $\pi R_N^2 V_N \rho_l$ in Figure 2.6, must equal to the mass of the solidified ribbon leaving from the puddle per unit time, $A_R V_S \rho_s$, or

$$A_R = V_N (\pi R_N^2 \rho_l / V_S \rho_s) \dots\dots\dots (8)$$

where, A_R is the cross-sectional area of the ribbon, R_N is the nozzle radius, V_N is the average velocity at nozzle, V_S is the velocity of the moving substrate, and ρ_l and ρ_s are, respectively, the density of the liquid metal and solidified ribbon at their respective temperatures.

From Equation (8), it is apparent that a ribbon with constant cross-section area can be made only if the fluid velocity V_N through the nozzle is held constant. In order that the fluid flow from the nozzle of the reservoir be constant in time, the pressure at the nozzle must not vary. Changes in the nozzle velocity during ribbon making can be avoided by maintaining a constant reservoir depth. In the closed systems in which the molten alloy is ejected by gas pressure rather than the gravity, the pressure over the molten alloy may be lowered simultaneously with the reservoir depth.

2.2.4.2 Effect of Nozzle Geometry On Ribbon Uniformity

The ideal nozzle should impart the following properties to the liquid jet.

First, the liquid flow in the nozzle should be laminar but not turbulent. Turbulence is an indication of many local variations in velocity with time and space across the cross section of fluid flow. Such velocity fluctuations may cause temporal variations in the nozzle velocity, or puddle diameter and those generate dimensional nonuniformities in the resulting ribbon.

Second, the fluid velocity should be uniform across the cross sections of the jet. That the uniform velocity distribution provides the best condition to minimize turbulence and fluctuations in the liquid puddle beneath the jet.

Finally, the nozzle geometry should be selected to minimize the contraction in the cross-sectional area of the jet as it leaves the nozzle orifice or nozzle-substrate separation distance be made large enough so that the jet has reached a stabilized cross-sectional area by the time it arrives at the moving substrate.

All of these conditions for a uniform and steady fluid flow are enhanced by a converging-nozzle geometry as seen in Figure 2.6. The laminarity of fluid flow is also stabilized by a converging nozzle geometry.

2.2.4.3 Cylindrical Jet Stability

Standing or traveling capillary waves can form on the liquid jet, as the liquid metal travels from the nozzle orifice to the moving substrate. These waves are

initiated at sources at the orifice and in the puddle. In addition, capillary waves can be generated along the jet by the interaction between the atmosphere and the jet. The velocity of capillary waves C_λ of wavelength λ is determined from a balance between inertia forces and surface tension. These waves can be formulated as

$$C_\lambda = (2\pi\gamma / \lambda\rho_l)^{1/2} \dots\dots\dots (9)$$

where γ is the surface tension of the liquid metal, λ is the wave length of the capillary wave, and ρ_l is the density of the liquid metal.

The jet velocity should be high enough to sweep all incipient capillary waves of some critical wavelengths and prevent their formation.

$$V_j > C_{\lambda \text{ cr}} \dots\dots\dots (10)$$

From Equations (9) and (10), it is apparent that it is not possible to eliminate all capillary waves, since $C_\lambda \rightarrow \infty$ as $\lambda \rightarrow 0$. However, since not all waves will grow on a cylindrical jet, it is sufficient to eliminate just those waves that will spontaneously develop. Waves of other wavelengths will be damped out and not form. As in Figure 2.7, a capillary wave of wavelength λ distorts a liquid-metal jet with an initial radius R_j . Because of the different surface radii of curvature at points A and B in the jet, a pressure gradient exist between points A and B. In response to this pressure gradient, fluid will flow between these points. Flow from A to B will stabilize the jet while flow from B to A will cause eventual breakup of the jet.

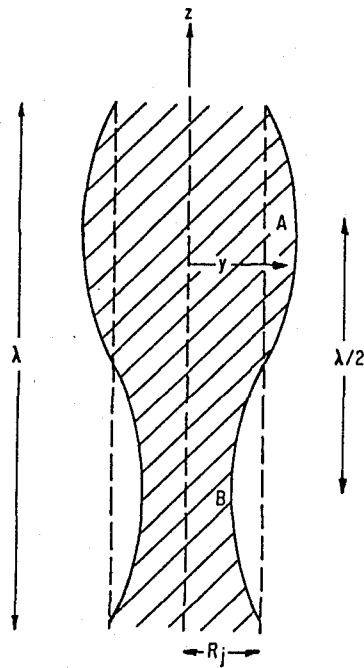


Figure 2.7 Standing capillarity wave of wavelength λ on the liquid metal jet of radius R_j .

The jet velocity not only must be large enough to wash away any shape instabilities developing on the jet but also must be great enough so that these instabilities do not grow to any appreciable size by the time they reach the puddle. Otherwise, the impingement of these instabilities on the puddle would cause a time variations in the ribbon dimensions.

Theoretically, several other types of instabilities can occur on the jet and puddle as illustrated in Figure 2.8. Kelvin-Helmholtz instability that has been mostly observed under the usual casting conditions causes the formation of characteristic disturbances along the ribbon edges. This instability arises from the relative motion between the stratified fluid of the melt puddle and the gas layer which moves with

the velocity of the chill block. The instability can be suppressed by casting in a light viscous gas such as He or H [10, 11]. The Marangoni instability is a bulk flow arising from local variations of surface tension. The Marangoni instability may be driven by concentration or temperature fluctuations. Rayleigh jet instability means that the cylindrical jet surface becomes increasingly perturbed as it leaves from the nozzle until at some distance the jet breaks up into droplets. Rayleigh jet instability is mostly observed in the liquid jet of metallic glasses having very high viscosities and low surface tension in the liquid state [7].

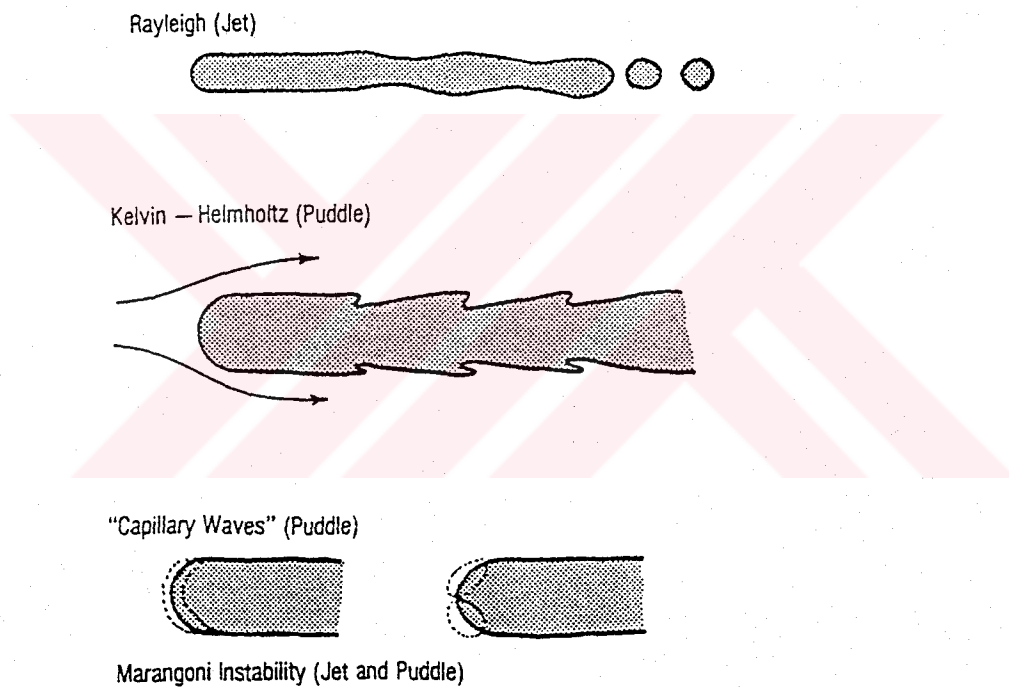


Figure 2.8 Casting instabilities.

2.2.4.4 Puddle Stability and Puddle (Ribbon) Shape

Since both the ribbon width w and the ribbon thickness t are affected by the shape of the puddle beneath the liquid jet, it is important that the puddle have a clean regular geometric shape that does not vary with time. Excessive jet velocities should be avoided to prevent the formation of a circular hydraulic jump on the substrate. The turbulent disturbance around the outer periphery of the hydraulic jump would cause the puddle to be irregular both in space and time. Thus, it would cause the resulting ribbon to be irregular both across its width and along its length.

The puddle shape is for a jet impinging perpendicular to a flat moving substrate. If a jet impinges at an angle to the substrate, a net momentum will be imparted to the puddle and this momentum will distort the puddle in a direction away from the jet. Similarly, if the substrate is curved (e.g., a spinning wheel), the effect of gravity will distort the puddle in a downward direction along the wheel. Also, the interaction of the air boundary layer with the molten puddle may distort or wobble the puddle. If this distortion of the puddle is not even or constant in time (as in high-speed wheel spinning process), dimensional nonuniformities will appear in the resulting ribbon.

So far, we have followed the liquid on its path through the reservoir, the nozzle, the jet, and the puddle, and pointed out what parameters should be adjusted to give a steadiest and most uniform flow. However, even after all of these precautions, the intersection line of the puddle with the substrate will probably vary in space and

time. As shown in Figure 2.9, it is obvious that the width of ribbon is drawn out from the time-varying lateral extremes of the puddle. [8]

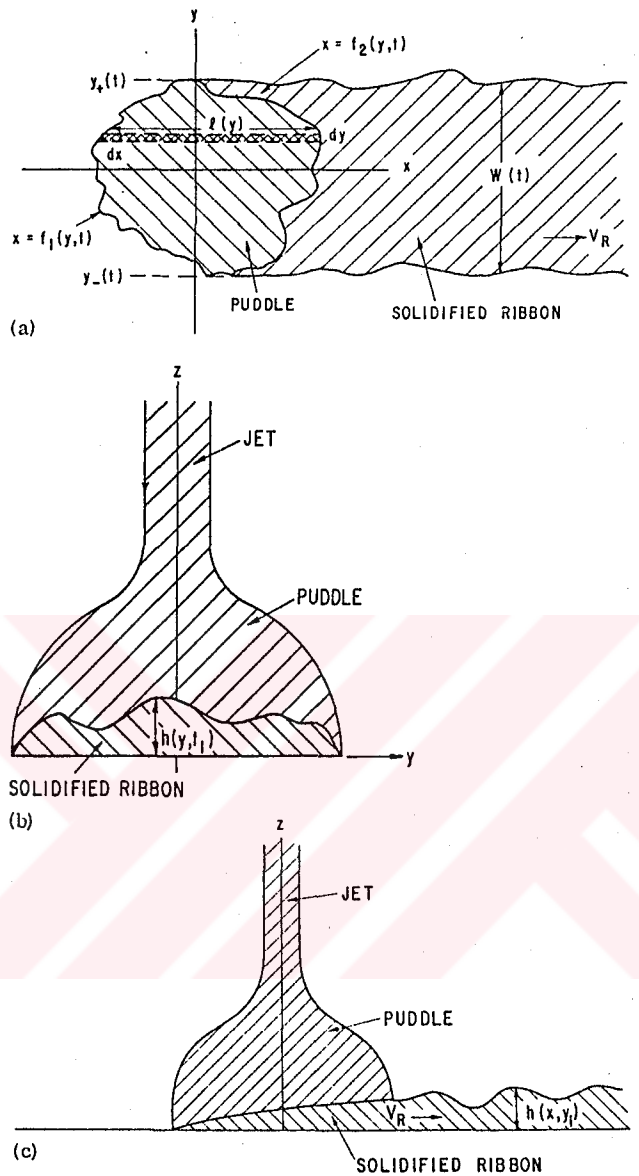


Figure 2.9 (a) A projection of the intersection line of the puddle and ribbon with the moving substrate. The puddle lateral extremes are shown, as $y_+(t)$ and $y_-(t)$ and the ribbon width as $W(t)$. (b) A projection of the jet, puddle and the ribbon on Z-Y plane. The variation of the ribbon thickness across its width. (c) A projection of the jet, puddle and the ribbon on Z-X plane. The variation of the thickness along the ribbon is shown.

If the lateral extremes of the puddle do not vary with time, then the resulting ribbon will have a uniform width along its entire length. In contrast, any lateral puddle motion seen in a high-speed ribbon making process is a direct indication that the ribbon produced in that process will have a width that varies along its length.

In Figure 2.10, the lateral cross sections of various ribbons formed from rectangular, square, circular, and ellipsoidal puddles which do not vary with time are shown. Since rectangular or square puddles do not form beneath cylindrical jets, it must be concluded that the current mode of making ribbon with a cylindrical jet will produce a ribbon with dimensional uniformity only along its length but not across its width. But, if care is not taken to eliminate vibrations and to operate under the conditions of steady uniform fluid flow, then the ribbon produced from the cylindrical jet will also be nonuniform along its length.

The shape of the puddle and its variations in time gives important knowledge to the type and stability of the process. For example, a flat ribbon whose thickness does not vary across its width is the indication of that the ribbon was made from rectangular puddle constrained at its sides by solid walls to maintain the rectangular shape of the puddle (i.e. planar flow casting). A ribbon whose thickness varied periodically across its width would suggest it was made by a multiple jet process whose jet diameters equal the lateral periodic spacing on the ribbon. As the last example, a ribbon rounded across its width (some commercial amorphous type) would indicate it was made by a single cylindrical jet.

Consequently , variations in either the thickness or width of a ribbon along its length are evidence of an unstable puddle and a ribbon making process that needs to be better controlled.

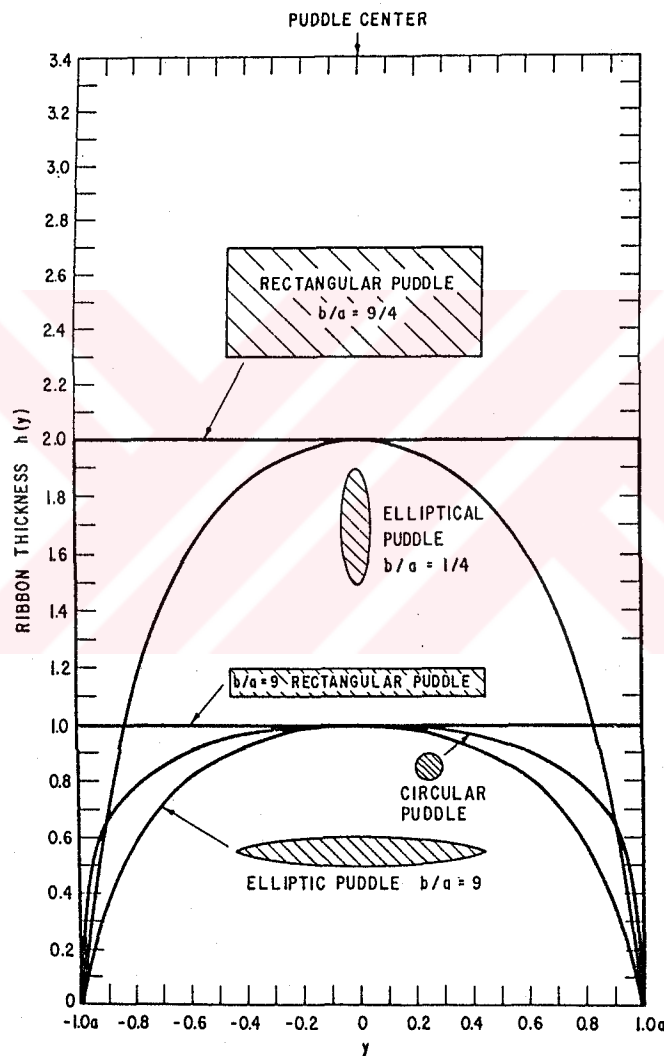


Figure 2.10 Lateral cross sections of the ribbons pulled from puddles of circular, rectangular and ellipsoidal shapes. [8]

2.2.4.5 Ribbon Dimensions

It can be understood that the two major operating parameters, volumetric flow rate Q and the surface velocity of the roll V_s control the final cross-sectional dimensions, thickness t and width w , of the ribbon.

The overall mass balance gives:

$$Q = \pi R_j^2 V_j = t w V_s \dots\dots\dots (11)$$

The melt puddle spreads to a size such that $t \cdot w$ satisfies this balance; w equals to the puddle width, while t is related to the puddle length l through the residence (dweel) time θ_R as it was defined in section 2.2.2. In order to keep Q constant, V_s must not be changed during the ribbon formation.

In CBMS, the round section liquid jet is free and the puddle spreads laterally as well as in direction of casting. For the PFC the small nozzle/roll separation distance generally prevents significant lateral spread and w is equal or similar to the slot length. From the viewpoint of the magnitude of the cooling rate and the mechanism of ribbon formation, t is the important parameter [5, 7, 8, 12]. Decreasing the ribbon thickness, increasing the cooling rate. (Figure 2.11)

Some researchers derived experimentally relations about the ribbon dimensions: Hillman and Hilzinger [5] from photographic measurements of l for the glassy alloy $Fe_{40}Ni_{40}P_{14}B_6$, found

$$t \propto \theta_R^m \dots\dots\dots (12)$$

with $0.5 \leq m \leq 1$ and solidification time

$$\theta_R = l / V_s \dots\dots\dots (13)$$

From Equations 12 and 13, the ribbon thickness may be written as

$$t \sim l^m / V_s^{-m} \dots\dots\dots (14)$$

However, according to regression data analysis of the same alloy by Liebermann and Graham [7, 13] the following sets of expressions are determined.

$$w = c_1 (Q^n / V_s^{1-n}) \dots\dots\dots (15)$$

$$\langle t \rangle = c_2 (Q^{1-n} / V_s^n) \dots\dots\dots (16)$$

where $\langle t \rangle$ is the average ribbon thickness across its width. In this case ribbon cross section A_R which is $t.w$, can be assumed as a rectangular and calculable.

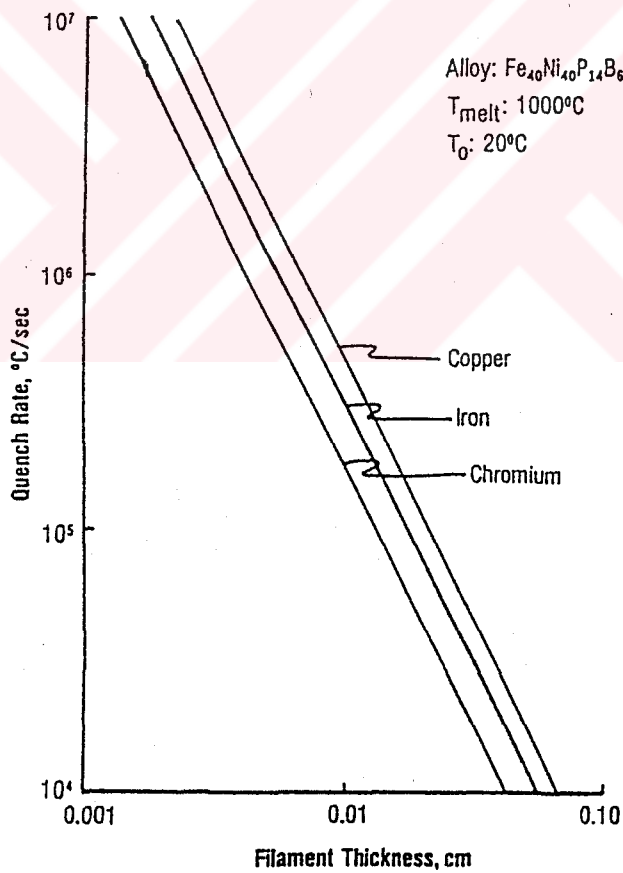


Figure 2.11 Relationship of quench rate of ribbon thickness and substrate character.

2.3 Rapid Solidification of Aluminum Alloys

There are two major limitations common to all conventional aluminum alloys. One of them is thermal stability. Age-hardenable compositions tend to lose strength rapidly above temperatures in the range 100-200 °C (0.4 to 0.5 T_m) as a result of precipitate coarsening. Resistance to coarsening can be improved by reducing solubility and diffusivity of solute in the matrix and by reducing interfacial energy between the precipitate and the matrix. Transition metal additions in general satisfy the first requirement and the metastable ordered cubic Al_3M ($M \equiv$ transition metal) precipitate formed. It may also, at least potentially, satisfies the second one. Such additions are limited to small amounts in conventional processing to avoid formation of embrittling intermetallic phases during solidification. Rapid solidification removes this limitation either by generating directly a suitable fine dispersion of the intermetallic phase in the α -Al matrix, or by retaining the addition in extended solid solution for subsequent precipitation in a subsequent aging treatment.

Another deficiency of conventional aluminum alloys is their low elastic stiffness which is approximately one-third that of steel. Considerable increases in modulus can also be achieved by using rapid solidification to disperse a substantial volume fraction of high-modulus intermetallic compound formed by transition metal additions.

2.3.1 High Temperature Aluminum Alloys

Transition metals have very low equilibrium solid solubilities in aluminum and very low diffusion rates. Both factors are essential in developing high temperature aluminum alloys. Low diffusion rates ensure very slow or minimal coarsening of dispersoids in aluminum matrix. In other words, once the dispersed phase form in the solid solution, the nucleation of new phases and/or the growth of existing dispersoids will be very slow. As such development of high temperature aluminum alloys through RSP involved addition of at least one transition metal. The relative resistances of aluminum alloys to diffusion of transition metal elements are indicated in Table 2.3 [17].

Table 2.3 Diffusivity, liquid and solid solubility of some transition metals in Al.

Transition metal	D (cm ² s ⁻¹) at 618 K	Liquid solubility at 1400 K (wt.% (at.%))		Maximum equilibrium solid solubility at indicated temperature		
Fe	5.4 x 10 ⁻¹⁴	32	(18.52)	0.04	(0.025)	at 928 K
V	7.4 x 10 ⁻¹⁵	1.6	(0.85) ^a	0.6	(0.32)	at 934 K
Zr	3.4 x 10 ⁻¹⁸	11.5	(3.7)	0.28	(0.085)	at 934 K
Cr	1.1 x 10 ⁻¹²	15	(8.4)	0.77	(0.40)	at 934 K
Ce	8.4 x 10 ⁻¹⁶	41.5	(12)	0.05	(0.01)	at 910 K
Mo	2.4 x 10 ⁻¹⁴	3	(0.86)	0.25	(0.056)	at 934 K
Ti	3.0 x 10 ⁻¹⁶	6.3	(3.6)	1.3	(0.57)	at 938 K

^a At 1200 K

Beginning with the work of Jones [13], it was demonstrated that rapid cooling of liquid to solid could result in the extension of the solid solubility of iron in aluminium of orders of magnitude (from 0.05 to about 10 wt %). He observed metallographically two distinct zones (A and B) on the normal-sections of the splat

cooled foils of Al-Fe binary alloys containing 4-24 % Fe. The hardened surface layer (zone A) is exposed layer (more frequently to substrate side) and distinguishable by its relative lack of response to etching. However, a dark etching and less hardened layer (zone B) is occupied at the central areas of the foils. Microanalysis on an Al-8%Fe sample showed no significant differences in iron content between these two zones. X-Ray diffraction of splats containing zone A showed broadening and shifting of α -Al reflections indicating a reduction in lattice parameter and showing supersaturation. In zone A second phase reflections were not detected. For zone B, in contrast, α -Al reflections were not significantly broadened or shifted, and second phase metastable FeAl_6 reflections were detected, displacing the equilibrium FeAl_3 phase. All these results showed that the higher cooling rate was necessary to form zone A than zone B and that high cooling rate can occur during deposition if the thermal contact between splat and substrate is adequate. Jones also reported that rapidly solidified Al-Fe alloys with Fe up to 10 wt % present a fine cellular structure. The cells are a solid solution of α -Al with intercellular regions consisting of small randomly oriented precipitates.

It was further shown by Thursfield and Stowell [18] that controlled nucleation and growth of metastable second phases (e.g. Al_6Fe) during extrusion of splat-cooled Al-Fe alloys leads to high stiffness and high strength because of the dispersoids acting as the obstacles to dislocation motion, and to retention of high levels of strength to high temperatures (350 °C) because of the relative resistance of the Al-Fe dispersoids to Ostwald ripening.

Other works on binary Al-TM alloys comprise of Al-Mn, Al-Cr and Al-Zr alloys, D. Shechtman *et al* [19] identified of quasi-crystalline icosahedral phases (i-phase) on Al-Mn alloy, opening up a new chapter in the understanding of crystal structure. They observed the icosahedral phase forms during rapid cooling of the melt by a nucleation and growth mechanism. This mechanism is characteristic of a first-order transition because the two phases coexist along a moving interface. Each particle nucleates at a center and grows out from there. Their evidence for the first-order character is morphological. Samples with 10 to 12 at.% Mn showed many nodular grains separated from each other by crystalline films of fcc Al. The morphology is similar to a commonly observed one in rapid solidification in which crystals nucleate at many centers and grow until the remaining liquid solidifies. The obvious cellular morphology indicates that the growth of i-phase is slow enough to permit little diffusional segregation on the scale of 1 μm . But, the i-phase in rapidly solidified Al-Mn alloys is remarkable resistant to crystallization. They conclude that the icosahedral phase is a truly metastable which nucleates and grows for a range of cooling rates which are slow enough to permit its formation but rapid enough to prevent crystallization. The icosahedral phase has lacking translational symmetries intermediate between those of a crystal and a liquid. It differs from other intermediate phases in that it is both solid, like a metallic glass, and that it has strong orientational order. The x-ray diffraction patterns obtained from the i-phase could not be indexed to any Bravais lattice although consisting of sharp diffraction lines like a crystal.

Using the precise x-ray data by Bancel *et al.* [21], Csanady *et al.* [20],

recognized the 200 and 111 lines of fcc-Al as well as the peaks of the quasicrystal icosahedral phase on melt-spun Al-5.3 at % Mn alloy as it is seen in Figure 2.12.

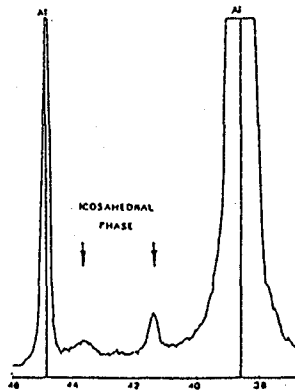


Figure 2.12 X-ray diffractogram of the (Al-5.3% Mn) melt-spun ribbon.

It is observed that, however, all the binary aluminum-TM alloys are moderately soft and/or they possess only moderate thermal stability. Coarsening and loss of strength with these alloys can occur at intermediate temperatures because of the incoherent nature of the binary intermetallic dispersoids. Thus, optimization of alloy development focused on ternary or quaternary alloys. The most prominent alloys developed so far are based on Al-Fe with further additions of Ce, Mo or V + Si to establish ternary/quaternary intermetallics with a more symmetrical lattice. Among these dispersion strengthened alloy systems, the coarsening rates of dispersoids for Al-Fe-V-Si alloys are two or three orders of magnitude lower than for the Al-Fe-Mo and Al-Fe-Ce alloys (Figure 2.13) [16].

Figure 2.14 [16] shows a comparison of elevated temperature tensile yield strengths of various high-temperature aluminum alloys developed through RSP. As

indicated in the figure, these alloys have the potential to replace of titanium alloys to temperatures of the order of 200-230°C.

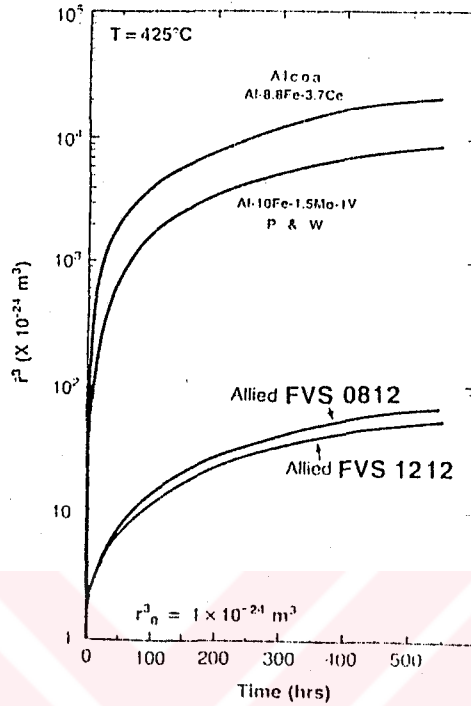


Figure 2.13 A comparison of coarsening rates of dispersoids in various rapidly solidified Al-TM alloys. r is the average particle size at time t .

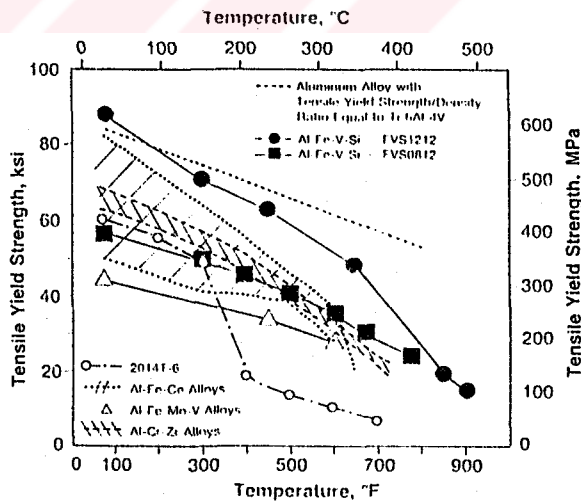


Figure 2.14 A comparison of elevated temperature tensile yield strength of various high temperature aluminum alloys and standard aerospace aluminum alloys.

2.3.2 Rapidly Solidified Al-Fe-V-Si Alloys

For any engineering applications, property improvements in only the primary proper (e.g. strength, density and modulus) is not sufficient to warrant its applications. Other secondary properties (e. g. fracture, fatigue, corrosion and oxidation) must also be improved. In the case of Al-Fe alloys although significant improvement in high temperature strength has been achieved, the alloys had poor fatigue and fracture properties. Furthermore, during fabrication of rapidly quenched Al-Fe alloys into usable shapes the alloys, as it is noted above, frequently lost their strength due to the poor thermal stability of Al_xFe_y intermetallic compounds, which are responsible for high temperature strength [16, 22]. The development of high temperature aluminum alloys at Allied-Signal was initiated in early 1980's to developed alloys with a balanced set of properties for aircraft structural applications [23]. A series of aluminum-iron-vanadium-silicon alloys which combine good elevated temperature strength, ductility, fatigue and fracture toughness have been developed [14, 16, 22, 23, 24].

The three most advanced Al-Fe-V-Si alloys are: FVS0611, FVS0812 and FVS1212. These three alloys have been designed with specific applications and product forms. Table 2.4 lists the compositions and product forms of these alloys [15]. Recently, a commercial alloy developed by Allied Signal, namely FVS0812 (Al-8Fe-1.4V-1.7Si by wt%), has been re-designated as 8009 by the Aluminium Association [25]. These alloys contain high transition element concentrations that

form high volume fractions of silicides dispersoids and their desirable microstructural morphology essentially controls the mechanical properties of these alloys.

Table 2.4 Nominal Composition of Rapidly Solidified Al-Fe-V-Si Alloys and Their Product Forms

Alloy	FVS 1212	FVS0812	FVS0611
Composition (weight %)	11.7 Fe 1.2 V 2.4 Si	8.5 Fe 1.3 V 1.7 Si	6.5 Fe 0.6 V 1.3 Si
Designed for	High Stiffness	Good Fracture Toughness	High Formability
Product Form	Sheet Extrusions	Forging, Extrusions	Rivet Wires, Thin Tubings

In the pioneering study, Skinner *et al.* [14] showed the stabilization of the cubic phase in ternary Al-Fe-Si alloy by the addition of quaternary element, vanadium. The addition of vanadium in relatively small amounts to Al-Fe-Si alloys stabilized the bcc α -Al₁₂(Fe, V)₃Si (silicide) phase (complex with 138 atoms/unit cell), rather than the equilibrium hexagonal phase Al₈Fe₂Si [34-37]. X-ray analysis performed on Al-Fe-V-Si alloys showed no indication of other intermetallics apart from this cubic phase. This silicide phase has a bcc structure and no tendency for the formation of needle or plate-like precipitates which degrade alloy ductility and fracture toughness. These very fine, nearly spherical Al₁₂(Fe,V)₃Si (silicide) dispersoids are uniformly distributed throughout the aluminum matrix in high

volume fractions (16 to 37%) and have superior high temperature strengths and excellent thermal stability because of their much slower coarsening rates (three to four orders of magnitude slower) compared to the non silicon dispersoids found in other high temperature aluminum alloys (Figure 2.13, 2.14). It is apparent that these uniformly distributed ultra fine spherical dispersoids (0.05 μm in diameter [14]) in high volume fraction pin the grain boundary movement at high temperatures. According to the investigations of Skinner *et al.* [14], increasing the iron to vanadium ratio from 5 to 10 further decreases the coarsening rate of these silicide dispersoids. EDX analysis on these dispersoids reveals that the initial Fe:V ratio formulated in the alloy composition is carried through to the dispersoid. The Fe:V ratio in the dispersoid changes the lattice parameter of the phase. Even though the silicides are noncoherent dispersoids, it is considered that their much slower coarsening rates are due to the fact that the silicide lattice parameters which are in the range of 1.260 to 1.2620 nm for the alloys with above Fe:V ratios. Skinner concluded that the silicide lattice which is approximately three times the unit cell edge length for aluminum (0.4049596 nm), closely overlays the aluminum unit cell leading to some degree of coherency and slower than predicted coarsening rates. The high thermal stability allows silicide containing alloys to be forged into desired product forms such as extrusions, forgings, sheet, and wire [15] (Table 2.4). In addition, Skinner *et al* [14], observed the cast ribbons, of 25 to 40 μm thickness, were entirely of zone "A" microstructure which is firstly pointed out by Jones [13].

Figure 2.15 (a) displays the microstructure of as-cast Al-8Fe-1V-2Si alloy which is strengthened by intermetallic dispersoids of $\text{Al}_{12}(\text{Fe,V})_3\text{Si}$, some 20-50 nm in diameter in an aluminum matrix. It is a microcellular structure and the second phase particles of the silicide phase decorate the cell boundaries [26]. After extrusion at 375 °C the structure is as shown in Figure 2.15 (b). In this case, the uniform concentration of spherical dispersoids of $\text{Al}_{12}(\text{Fe,V})_3\text{Si}$, about 50 nm in diameter and 24% volume fraction. This fine-scale uniform structure provides a high toughness [16].

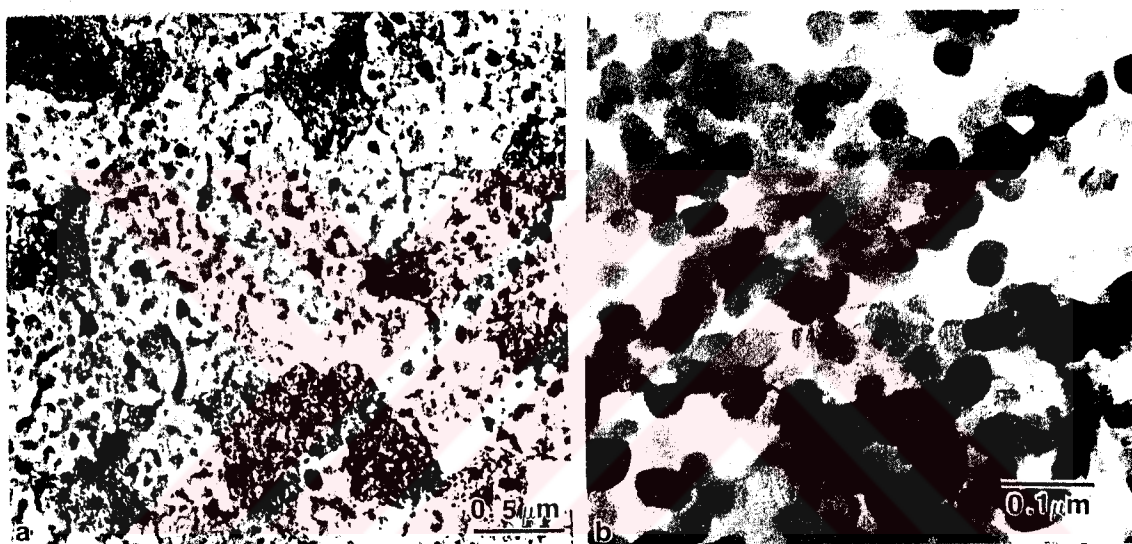


Figure 2.15. Microstructures of RSP Al-8Fe-1V-2Si alloys (a) in as-quenched melt-spun ribbon and (b) after extrusion at 375 °C (a reduction of 18 to 1) [16].

The presence of a large volume fraction of these silicide dispersoids also results in a marked increase in elastic stiffness. The Young's modulus at room temperatures for the alloys Al-12Fe-1V-2Si (containing about 37 volume % of dispersoids), and Al-8Fe-1V-2Si (containing about 24 volume % of dispersoids), are reported as 96.5 GPa and 82.8 GPa respectively in the Technical Bulletin in 1987 by

Allied-Signal. Consequently, rapidly solidified Al-Fe-V-Si alloys are useful stiffness critical applications as well as high temperature applications.

These uniformly distributed fine scale silicide dispersoids have also been reduced oxygen and hydrogen contents [27]. Alloy FVS0812 is extremely corrosion resistant as measured by exposure to a salt fog, (Figure 2.16) [15]. The excellent corrosion strength of this alloy is thought to be due to the fine, uniform distribution of the silicide whereby the silicides act to increase the adherence of the aluminum oxide layer. Moreover, they act as closely spaced dipoles that negate the chemical polarization of the alloy [22]. The silicides are also chemically inert.

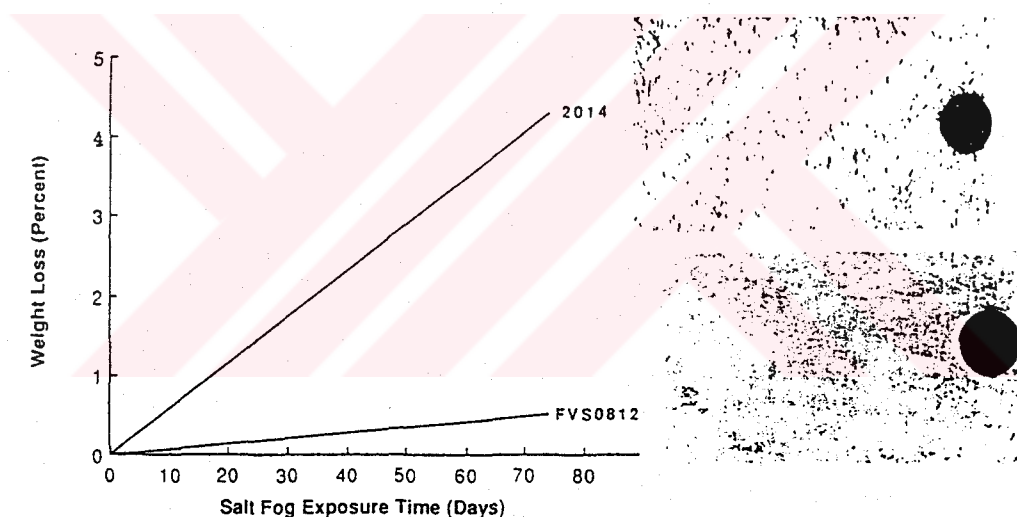


Figure 2.16 Corrosion performance of alloy FVS0812 in a salt fog environment.

All the works so far in all practical alloys of the aluminum-transition metals systems, rapid solidification produces either cellular-dendritic or icosahedral solidification structures. Kim [28] has demonstrated that the bcc structure of $Al_{12}(Fe,V)_3Si$ (silicide) dispersoids is closely related to that of quasicrystals. When

we consider the investigation of Schechtman *et al* [19], it is not strange that an i-phase has been found in RSP Al-Fe-V-Si alloys. Here, that is the question when the $\text{Al}_{12}(\text{Fe},\text{V})_3\text{Si}$ (silicide) dispersoids forms in rapidly solidified Al-Fe-V-Si alloys. Some researchers [29] have reported that the intercellular regions in Al-Fe-V-Si alloys consisted of many randomly oriented i-phase particles. These quasi-crystalline phases can transform to $\alpha\text{-Al}_{12}(\text{Fe},\text{V})_3\text{Si}$ particles after consolidation. In other words, silicide dispersoids form from the decomposition of the rapidly solidified microstructure. However, other researchers found that the intercellular phases had $\alpha\text{-Al}_{12}(\text{Fe},\text{V})_3\text{Si}$ particles as the primary phase [30].

Tang *et al.* [31] have been studied on rapidly solidified Al-8.9wt%Fe-1.7wt%V-2.0wt%Si alloy to understand the relationship between the formation of the i-phase and thermal history of the melt. In this study nine alloys with same compositions were ejected with different ejecting temperature (950, 1150, 1350 °C) and holding times before ejections (0, 5, 10 minutes) on to a copper drum rotating with a surface velocity of 30 m/s. Melt-spun ribbons obtained 10 mm in width and 60 μm in thickness were examined both by transmission electron microscopy (TEM) and X-ray diffraction (XRD) with CuK_α radiation. After these examinations they made the following observations and conclusions:

At all lower ejecting temperatures, a larger (0.2 ~ 0.5 μm) globular i-phase particles existed in the $\alpha\text{-Al}$ matrix, even after a long holding time before ejections. There was no difference in the morphology and the grain size of the i-phase in the

alloys which are ejected at temperatures lower than 1350 °C. However, at ejecting temperatures of 1350 °C, the sizes of the i-phase obtained after holding 5 min before ejecting was smaller than that obtained after direct ejecting. But at the temperature of 1350°C and after the holding time of 10 minutes before ejection, the globular i-phase disappeared. It was considered the solute elements have a higher ability to diffuse and a longer time to form finer clusters or nucleation centers. Finally, a microcellular structure (zone A) formed without a large globular i-phase. Figure 2.17 shows the microstructures of the rapidly solidified Al-Fe-V-Si alloys with different ejecting temperatures and holding times before ejecting.

The XRD and EDXS analysis showed that the intercellular precipitations of silicide particles in the α -Al matrix were also i-phase, having the same structure as the larger i-phase grains found in the matrix, with a chemical composition of 86.7 at% Al, 8.0 at% Fe, 2.1 at% V, 3.2 at% Si. Figure 2.18 shows XRD spectra for these two alloys, the upper one has i-phase and the lower has not. It is clear that there is no obvious difference between these two spectra and so, this result supports that the larger i-phase grains have the same structures as the finer intercellular particles. They also reported that the globular i-phase particles showed a typical icosahedral symmetry (Figure 2.19).

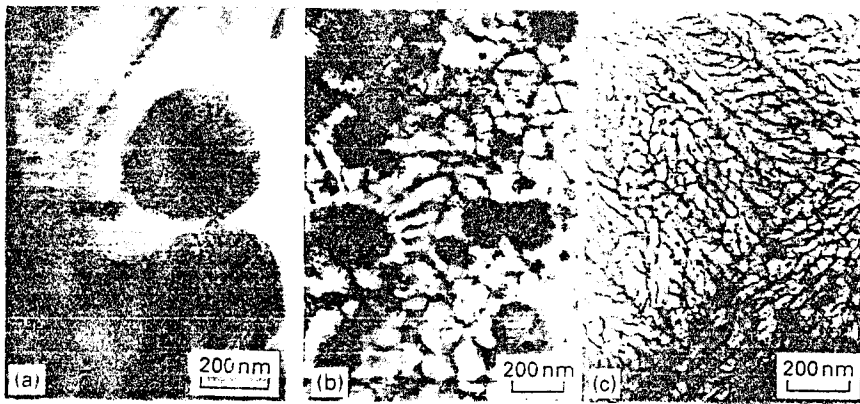


Figure 2.17 TEM micrographs of RS Al-Fe-V-Si alloys with (a) 950 °C, 0 min (b) 1350 °C, 5 min and (c) 1350 °C, 10 min.

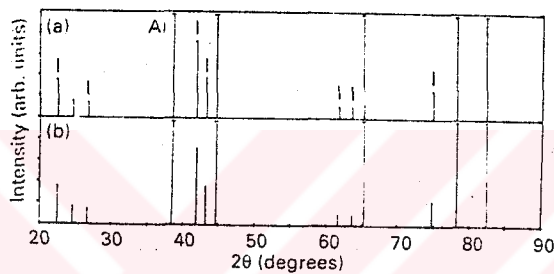


Figure 2.18. The XRD patterns of RS Al-Fe-V-Si alloys with (a) 1350 °C, 5 min (i-phase existing). (b) 1350 °C, 10 min (not i-phase existing).

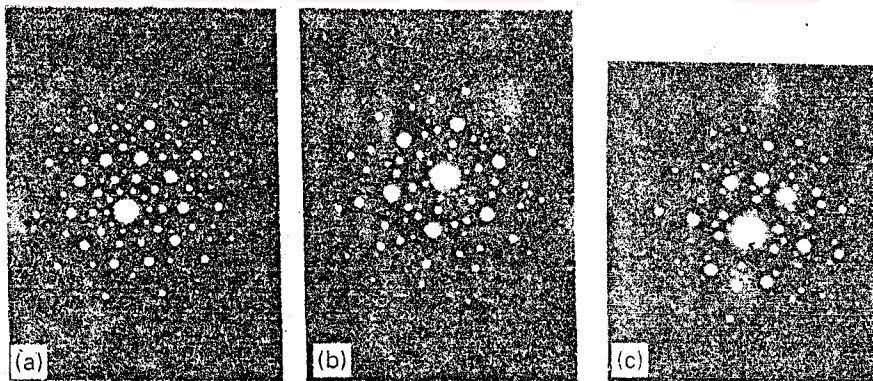


Figure 2.19. Different orientation diffraction patterns from a quasi-crystals of the alloy which was ejected at 950 °C with no holding time before ejecting, with (a) 5-fold, (b) 3-fold and (c) 2-fold rotation symmetry.

Radmilovic et al. [32] also observed a large volume fraction of 20-100 nm size cubic silicide particles uniformly distributed in the Al-matrix with a tendency to form agglomerates in as-extruded condition as in Figure 2.20 (a). The agglomeration is primarily due to the fact that silicides are located predominantly at the cell boundaries during rapid solidification. (This microstructural evolution was also displayed in Figures 2.15 (a) and (b).) Figure 2.20 (b) shows the selected area diffraction pattern (SADP) from the region in Figure 2.20 (a). As it is seen from the figure, particles are randomly oriented and do not exhibit any consistent crystallographic orientation relationship to the matrix.

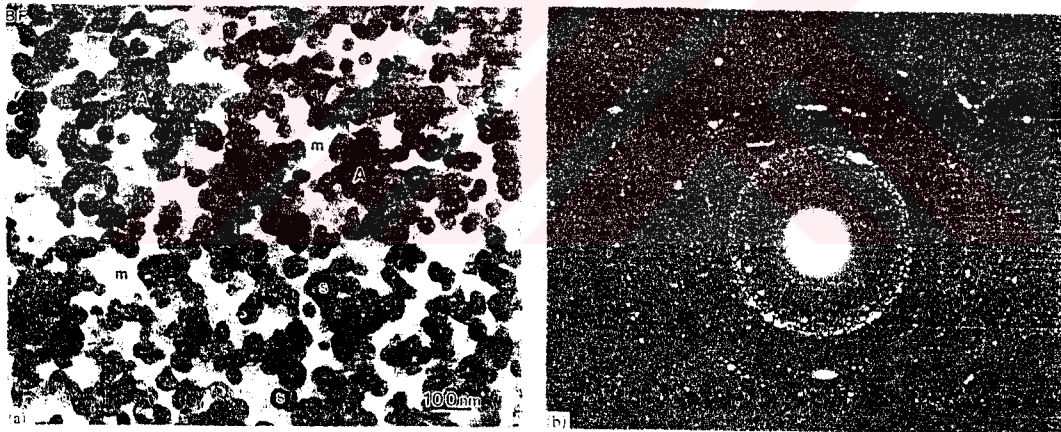


Figure 2.20 (a) Bright field image of Al-Fe-V-Si alloy in as-extruded condition; note the silicide particle agglomerates (A): m, aluminum matrix; s, silicide particles. (b) Diffraction pattern of the structure in (a), note the absence of any consistent crystallographic relationship between the silicide particles and the aluminum matrix.

In a recent report Srivastava and Ranganathan [33] have discussed an interesting microstructure of an icosahedral quasicrystalline phase with the pentagonal star shape surrounded by the ring consisting of very small crystalline silicide particles as seen in Figure 2.21. While the size of central quasicrystal was of the order of $1\mu\text{m}$, the approximate average size of the surrounding grains varies from $0.15\mu\text{m}$ to $0.3\mu\text{m}$. SADPs taken from two different regions of the crystalline ring (marked with arrows in Figure 2.21) are displayed in Figures 2.22 (a) and (b). These patterns show a bcc phase along $[\bar{1}22]$ zone axis. Only the crystalline cubic phase corresponding to $\text{Al}_{12}(\text{Fe},\text{V})_3\text{Si}$ was observed in TEM.

Consequently, all the results of rapid solidified Al-Fe-V-Si alloys have indicated considerable variation in the microstructure of these alloys.

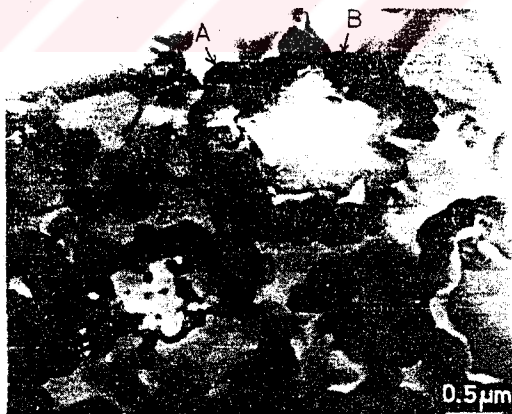


Figure 2.21 TEM bright field micrograph showing growth morphology of icosahedral phase surrounded by crystalline ring.

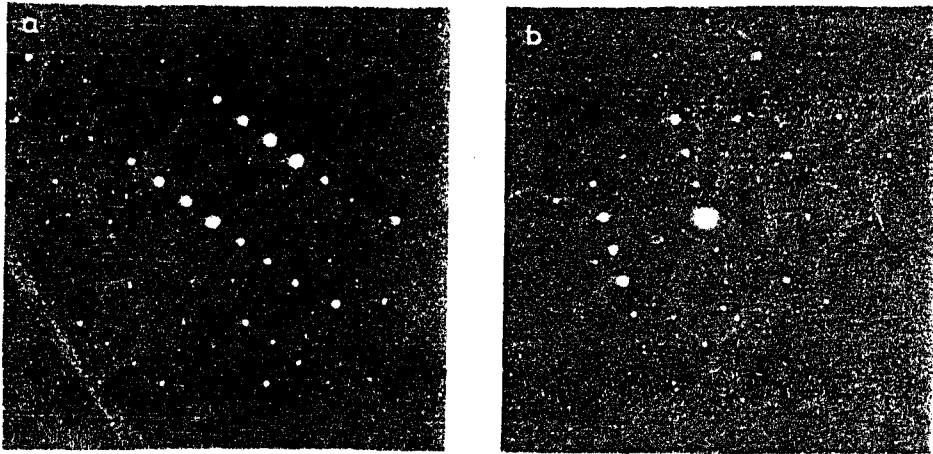


Figure 2.22 SADPs of silicide grains from regions A and B of Figure 2.21 corresponding to zone $[\bar{1}22]$ axes.

CHAPTER 3

EXPERIMENTAL PROCEDURE

In this work, firstly, production of rapidly solidified Al-Fe-V-Si alloys designed for mainly high temperature strength application in ribbon and flake form by melt spinning technique was studied. Then, in turn, identification of the phases and examining microstructure of these melt-spun ribbons on both as-cast and heat treated conditions by X-ray diffraction, SEM and TEM methods were carried out.

3.1 Melt Spinning Apparatus

Melt Spinning machine set-up was made up of five main parts as indicated in Figure 3.1:

1. Spinning Wheel: A copper drum which is assembled on a table and cooled by water flow. Its diameter is 22 cm and capable to rotate up to 3456 cm/s (3000 rpm).
2. Electric Motor: It is a DC motor which is operated by direct current and used to rotate the copper drum with several speeds. It is commanded by a digital driver.

3. Digital Driver: It controls the rotation speed of spinning wheel by adjusting the current.
4. Crucibles: Crucibles can be oriented vertically (in z-direction) over the copper drum by a holder which is free from the main frame. They are made of graphite and have convergent nozzles. One of the graphite crucibles is for planar flow casting with the slot type orifice as indicated in Figure 3.2.
5. Gas Pressure Unit: The gas is carried from the gas supply (Ar or N₂) to the tap on the crucible by means of a polymer hose in order to eject the melt through the orifice on to the copper drum.

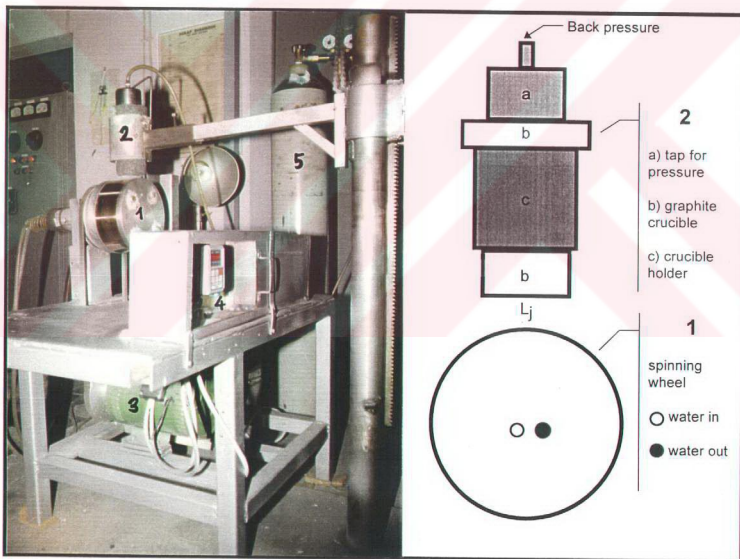


Figure 3.1 Melt-spinning set up. (1) Rapidly rotating water cooled copper drum, (2) Crucible holder, graphite crucible and pressure tap, (3) DC motor, (4) Speed control device, (5) Nitrogen gas tube.

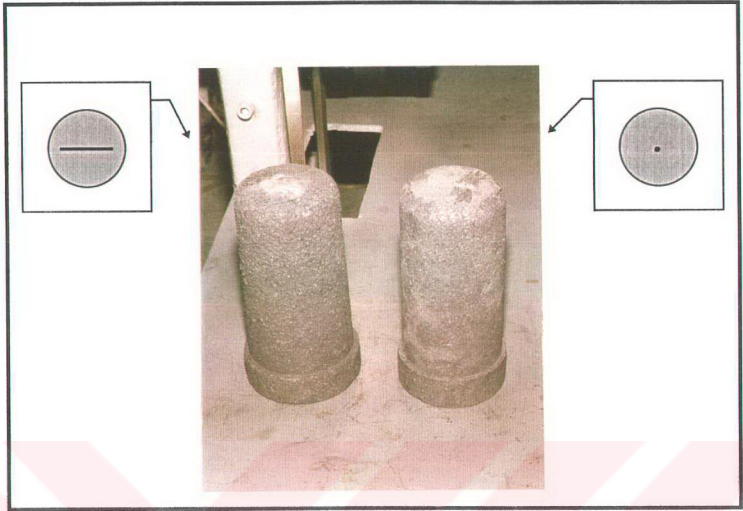


Figure 3.2 Melt-spinning graphite crucibles. The one on left is for planar flow casting.

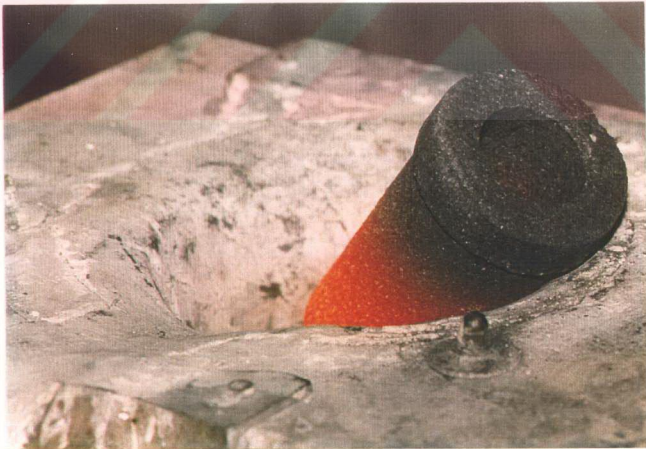


Figure 3.3 The crucible is being heated for casting.

3.2 Alloy Preparation, Casting and Heat Treatment Conditions

All the alloys were prepared by using as the starting materials of pure aluminum, scrap iron, Etial 140 including Al and about 13 % wt Si and Fe-80%wt V alloy. Charge calculation was made for the following master alloy compositions and weights before casting operations as it is seen in Table 3.1.

Table 3.1. Alloy preparation charge calculation table. Note that the alloys numbered by 1 and 2 are the specified alloys as FVS0812.

# of Alloy	Amount of Charge Materials (gr)				Alloy Composition (% wt)			
	FeV	Etial 140	Fe	Al	Al	Fe	V	Si
1	25.81	335.48	154.84	1483.87	88.8	8.0	1.0	2.2
2	13.00	100.00	57.00	576.00	88.9	8.0	1.4	1.7
3	20.00	72.00	40.00	410.00	87.3	8.0	3.0	1.7
4	20.69	60.18	31.44	335.12	86.6	8.0	3.7	1.7

These alloys were melted in induction furnace and poured into graphite crucibles then spinned by water cooled copper chiller. Among these alloys, the molten alloy #1 was pressurized by its gravity whereas the others were ejected by a back pressure gas (Ar or N₂) The ejection pressures ranged from 250 to 450 KPa. In all casting operations graphite crucibles with the convergent nozzle were used. The orifice diameters of the crucibles were 3.5 and 1.5 mm for the operations without and with pressure respectively. For planar flow casting operations carried out with pressure, slot type orifice of 10 mm x 0.5 mm in dimension was used. Although the crucible was heated to about 1000 °C

before casting as it is seen in Figure 3.3, the castings could not be performed through the smaller orifice in the case of not using a back pressure gas.

For the melt-spinning operations without pressure the copper drum was rotated at two different speeds of 2304 cm/s (2000 rpm) and 2880 cm/s (2500 rpm). Then it was kept constant as 2304 cm/s for all the operations performed with pressure. The gap between nozzle and wheel surface which is called jet length, was tested as about 8 to 10 mm for all castings except planar flow casting. Planar flow casting with the slot orifice (10 mm x 0.5 mm) were only tested for the molten alloy #4. In planar flow casting operations the crucible was positioned at the central axis of the wheel in z-direction and the jet length was about 4 mm. The melt-spun ribbons with several dimensions rather than flakes were obtained in all operations performed with pressure. Figure 3.4 shows the ribbon formation by melt spinning technique.

The flakes were heat treated at a temperature range of 150°C to 500°C for 0.5 to 3 hours to examine high temperature stability behavior. The similar procedure was performed for the ribbons at the temperature range of 200°C to 500°C for 1 hour.

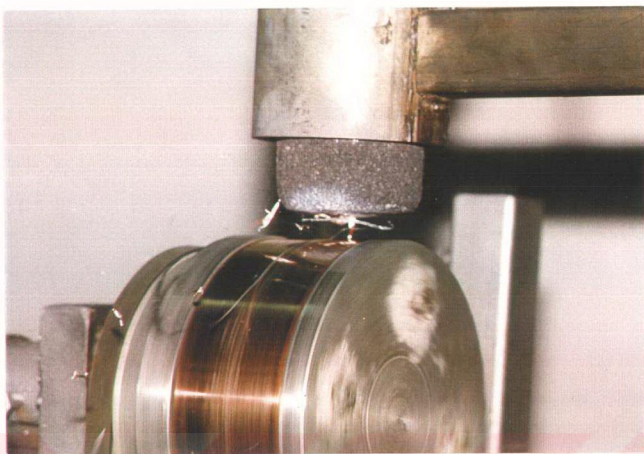


Figure 3.4. The ribbon formation by melt spinning technique.

3.3 X-ray Diffraction

All as-cast and heat treated melt-spun flakes/ribbons were carried out by X-ray diffraction using CoK_α and CuK_α for phase identification. In all diffractograms some definite diffraction lines were easily distinguishable with higher intensities from the others. All the patterns of those clear lines as well as the others were tried to index and determined of crystal structures in as-cast condition.

3.4 Scanning Electron Microscopy

The microstructural analysis was performed by scanning electron microscope (SEM) on some as-cast and heat treated samples. The melt-spun ribbons were

grinded by using abrasive papers (1200) and Keller's etchant for SEM examinations. Sample preparation was very problematic since resultant ribbons were very thin. EDS area analysis and point analysis were carried out during SEM study.

3.5 Transmission Electron Microscopy

The microstructural analysis was also performed by JEOL 100CX-II transmission electron microscope (TEM) operated at 100 kV.

The nonhomogeneities on the free-side of the melt-spun ribbons were grinded and then the discs 3 mm in diameter were punched from these grinded ribbons before electropolishing. Then, the punched discs were electropolished in 80% methanol and 20% nitric acid solution at a bath temperature of -50 °C with 10 volt cell potential by using Struers-Tenupol 3 Double Jet Electropolisher. Selected Area Diffraction Pattern, Bright Field Image and Dark Field Image techniques were studied on these TEM samples. Transmission electron diffraction patterns were also tried to index and calculate the lattice parameters in TEM study.

CHAPTER 4

RESULTS AND DISCUSSION

4.1 Characterization of Melt-Spun Flakes and Ribbons

In this section, mostly the ribbons were examined since the flakes have irregular shapes. But the first step of our melt-spinning experiments is the formation of flakes. In order to understand how the parameters affect the process, it is necessary to analyze flake formation in which pressure parameter of melt-spinning process is not applicable.

4.1.1 Flake Formation and Pressure

In the flake formation (melt-spinning with no pressure) the melt is released drop by drop from the larger orifice (3.5 mm) by its gravity to the copper drum rather than the continuous ejection by a gas pressure. So, non regular and relatively larger amount of melt spreaded laterally on the roll surface at each time and not possible to say formation of a stable puddle. The figure 4.1 shows the irregular melt-spun flakes which are obtained by a non-continious flow of the molten alloy.

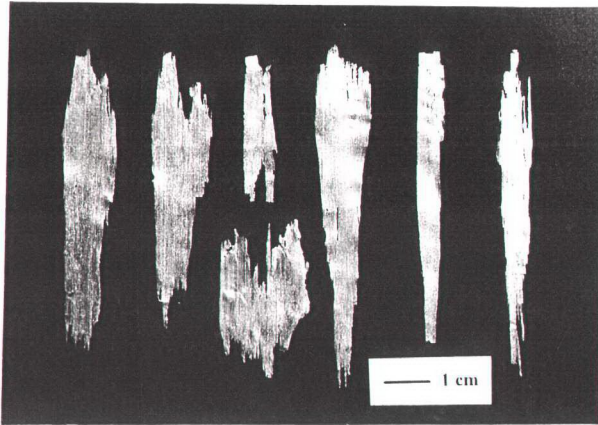


Figure 4.1 Melt-spun flakes with irregular shapes.

Absence of pressure also causes a practical application problem: Nozzle blockage. The molten metal solidifies and its viscosity increases drastically at the vicinity of the crucible orifice during the process. For this reason the process has to be finished in a very short time. If the pressure is not applied to the molten metal nozzle blockage may occur due to solidified metal at the orifice. Note that the crucibles used in our experiments have not been heated by induction melting coils which provide better superheat control.

Consequently, pressure is an unavoidable process parameter which controls the flow rate as well as get rids of nozzle blockage.

4.1.2 Flake Formation and Wheel Speed

In order to indicate the effect of wheel speed on flake thickness, copper drum was operated at two different velocities when the other parameters (jet length, orifice diameter, location of impingement point) are constant. The flakes obtained by the copper drum operated at 2500 rpm (2880 cm/s) are thinner than those at 2000 rpm (2304 cm/s). Correspondingly, the average flake thickness ranged from 120 to 250 μm for lower wheel speed, whereas it was in the range of 80 to 110 μm for higher wheel speed. This is the expected effect of wheel speed on filament thickness, that is, increasing the wheel speed decreases the filament thickness.

4.1.3 Effect of Process Parameters on Ribbon Dimensions and Uniformity

After the observation of the effect of wheel speed V_S on filament thickness, this critical parameter was kept constant as 2000 rpm in all the other castings to understand the effect of other parameters on ribbon dimensions.

The effect of pressure on the ribbon geometry was investigated first. When a nitrogen back pressure was applied to the liquid alloy in the crucible continuous flow of the molten alloy through the relatively small orifice (1.5 mm) could be obtained. As a result of this continuous ejection of the melt, the ribbons with several dimensions were obtained as indicated in Figures 4.2 to 4.5.

Figure 4.2 and the upper part of Figure 4.3 characterize the widths and the lengths of ribbons as about 3 mm and 20 to 60 cm respectively.

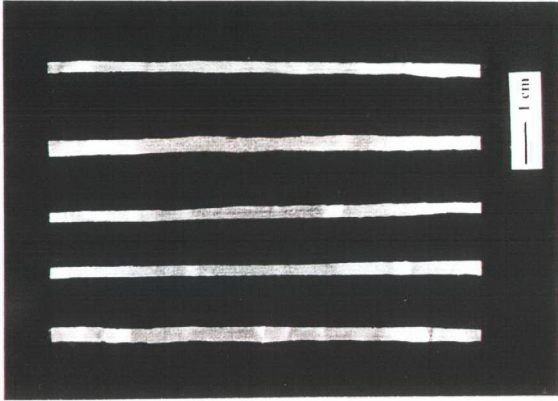


Figure 4.2 Ribbons with about 3 mm in width.

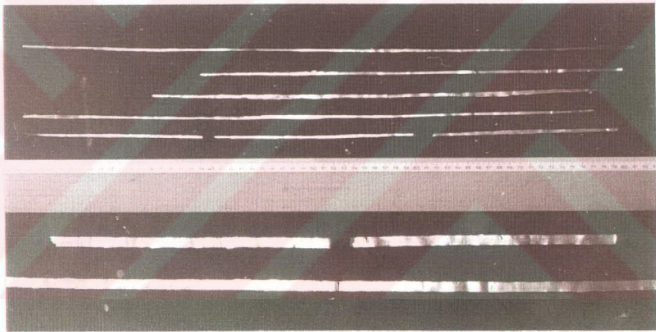


Figure 4.3 Ribbons with several lengths. Note that ribbons below the ruler are obtained by planar flow casting in which the melt is ejected through slot type orifice.

These resulting ribbons were not uniform across their width and along their length. For the ribbon 60 cm in length, for example, its width varies from 1.5 mm to 3 mm along its length. The similar non-uniformities were also observed on the

average thickness of these ribbons. Among these products the thinnest ribbon was noted as 30 μm in thickness as in Figure 4.4. However when we consider the whole products the average thickness is about 90 μm . It is too interesting to obtain ribbons in such variations (in thickness particularly) under constant casting conditions. Although the pressure which is the main parameter controlling the volumetric flow rate is constant, all these dimensional variations indicate that flow rate may change or instability waves may originate from liquid/air interaction during the process.

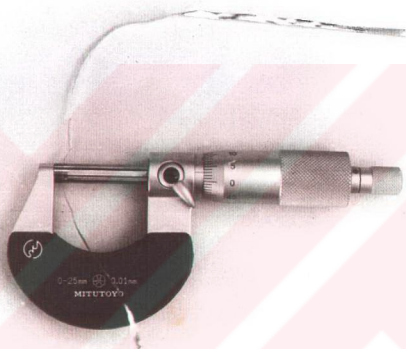


Figure 4.4 Ribbon with 30 μm in thickness in entire length.

If we consider that the melt puddle stability is directly related to the ribbon's uniformities, such variations may result from the variation or distortion of the shape of puddle beneath the liquid jet. We know that substrate velocity V_S must not be changed during the ribbon formation in order to keep volumetric flow rate Q constant according with Equation 11. Wheel speed V_S is constant (2000 rpm) throughout all the melt-spinning ribbon formation processes.

In order to investigate reason or reasons of this instability, we will compare these resulting ribbons with the other ribbon obtained by another casting operation. Figure 4.5 displays a uniform ribbon in a single piece (3 meters in length) obtained in one casting operation. The width of this ribbon is observed about 2.5 mm along its entire length and its average thickness is measured as 120 μm across its width and that value does not change considerably along its length.

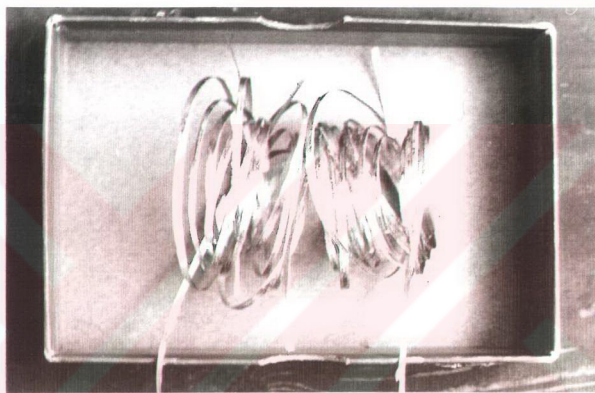


Figure 4.5 A uniform ribbon obtained in a single piece with about 3 meters in length.

The main difference between these two operations is related to the location of crucible over the copper drum. In the last operation whereby a uniform ribbon in a single piece was obtained, the impingement point of the molten jet was on the z-axis of the drum. In other words jet impinging was perpendicular to the spinning wheel. However, in the operation whereby ribbons with dimensional nonuniformities were obtained, the crucible was positioned where the impinging point C made an angle α

with the central z-axis of the spinning wheel. Figure 4.6 compares schematically two melt-spinning castings.

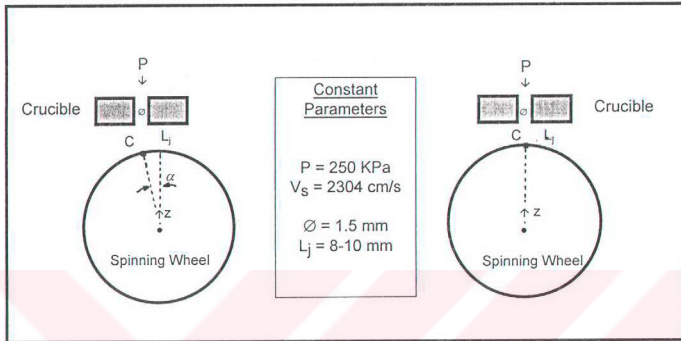


Figure 4.6 Schematic description of the positions of crucibles over the spinning wheel for two castings. C is the impingement point.

Now, we know practically that the impingement point of the molten jet must be on the central axis of the spinning wheel.

Consequently, the shape of melt puddle may be distorted by the gravity in a downward direction along the wheel when the impingement point of the molten jet makes an angle with the central axis of the spinning wheel. As a result of varying shape of melt puddle unevenly with time dimensional nonuniformities appears in the resulting ribbons.

4.1.4 Planar Flow Casting (PFC)

The planar flow casting in which the melt is ejected through a slot (rectangular) type orifice rather than circular one is an advanced form of CBMS process. In PFC the separation distance between the crucible and spinning wheel is shortened in order to make better control on relatively large amount of molten alloy. This limitation makes it also easy to form a stable melt puddle. The main practical advantage of PFC is to be able to obtain a ribbon with desired width by adjusting only the slot length of the crucible. In other words, width of the melt-spun ribbon is the same or similar with the slot length of crucible.

In order to obtain a uniform ribbon with 1 cm in width, three castings are performed under the following constant PFC conditions which are common in these three castings:

- Slot type orifice is 10 mm x 0.5 mm in dimension.
- L_j is adjusted as about 4 mm. (see Figure 3.1)
- Impinging of the jet is positioned at the central z-axis of the spinning wheel.
- Wheel speed is chosen as 2304 cm/s.

However, the back pressure of gas before ejection, in turn, are adjusted as 250, 350 and 450 KPa.

Figure 4.7 characterizes the ribbons obtained by three different pressures. The resulting ribbons are arranged in the figure one under the other by increasing order of pressure from top to bottom. It is easily observed from the figure that two unexpected results are appeared in the ribbons.

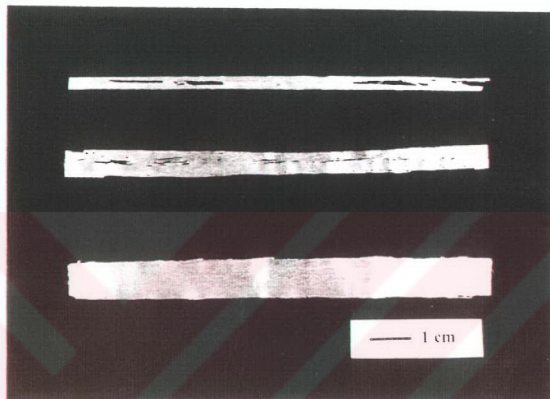


Figure 4.7 Effect of pressure on ribbon dimensions and surface texture in PFC.

The surfaces of the ribbons obtained by the pressures of 250 KPa (top in the figure) and 350 KPa (middle in the figure) are full of tears along their lengths. The same ribbons have also undesirable widths which are less than the slot length of the orifice.

However, the ribbon produced by the pressure of 450 KPa (bottom in the figure) has desirable width and also no surface defects.

The results obtained in PFC experiments against to pressure are tabulated in Table 4.1. According to the results the average thickness of the ribbons increases with increasing pressure as it can be expected.

Consequently, pressure is an important parameter controlling the volumetric flow rate Q which is closely related to the ribbon dimensions. Pressure must be adjusted properly in order to obtain suitable ribbons.

Table 4.1 Effect of pressure on ribbon dimensions and flow rate in PFC.

P (KPa)	w (mm)	t (μm)	$Q=l.w.V_s$ (cm^3/s)
250	3	120	8.3
350	5	150	17.3
450	10	250	57.6

4.1.5 Surface Analysis of Melt-Spun Ribbons

The texture of a ribbon surface may have some valuable indications in order to characterize the flow type of the melt during the melt-spinning castings.

Figure 4.8 displays two distinct surfaces of a melt-spun ribbon. The upper one in the figure indicates the free surface of the ribbon whereas the other one belongs to its chilled side. The chilled surface of the ribbon is always shiny and smooth, but the free surface of the same ribbon is mat and have many non-homogenities as seen

in Figure 4.8. Note that the ribbon in Figure 4.8 is obtained by a cylindrical molten jet formed by a circular type orifice 1.5 mm in diameter.

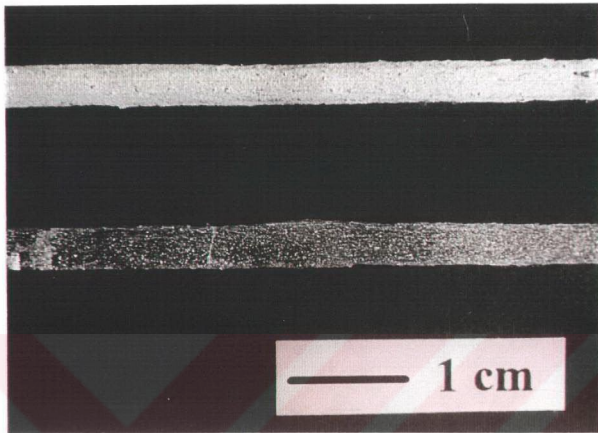


Figure 4.8 Two distinct surfaces of a melt-spun ribbon. The upper one indicates the free surface of the ribbon whereas the other one belongs to its chilled side. Note that its average thickness is about $90\ \mu\text{m}$.

Now, let us examine the free surface indications of a ribbon in a different photograph. Figure 4.9 shows flow pattern of free surface of the ribbon obtained by PFC under the highest pressure (450 KPa). There are many spots preferentially located at the free surface in the flow pattern. It also consists of concentric elliptical lines elongated in the direction of the flow. Those periodically accumulated particles and elliptical lines are large enough to be visible to the unaided eye as seen in Figure 4.9.

Formation of rotational flow spots along the ribbon can be explained by the boundary layer separation process which is described in Figure 2.5 in Chapter 2 [10]: Fluid elements close to the nozzle have a lower energy than those close to the wheel surface and are slowed down by the pressure gradient to the point where the flow direction is reversed [10].

Developing of this flow patterns on the free surface only, in accordance with the experimental observations, supports the above description.

The edges of the crucible nozzle can be considered as a large localized disturbance producing a turbulent spot. The turbulence can be periodically released, similar to the formation of turbulent plugs in pipes, and these spots occupy the entire ribbon cross section. (see Figure 4.9)

Examination of the free surface morphology revealed that, fluid motion in a melt puddle frequently is not laminar but turbulent.

Figure 4.10 characterizes a 30 μm thick strip. It shows a different free surface flow pattern, that is obtained by a circular liquid jet, as an exception. The central region of the ribbon along its length is not mat and doesn't contain non-homogeneities (turbulent spots, elliptical lines) but is shiny and smooth as if it is an chilled side. But both edge sides of the ribbon are mat and have the same indications of turbulent flow. It is noted that the thickness of this central region as 30 μm and is uniform along the entire length, whereas the both edge sides are much more thicker than the central region and not uniform along the ribbon. According to this extreme case,

turbulent flow produced by the orifice edges are spreaded to both edge sides of the central laminar flow.



Figure 4.9 Flow pattern of free surface of a ribbon showing accumulated particles and elliptical lines along its entire length. It is obtained by PFC under the highest pressure (450 KPa) and the average thickness is noted as 250 mm.

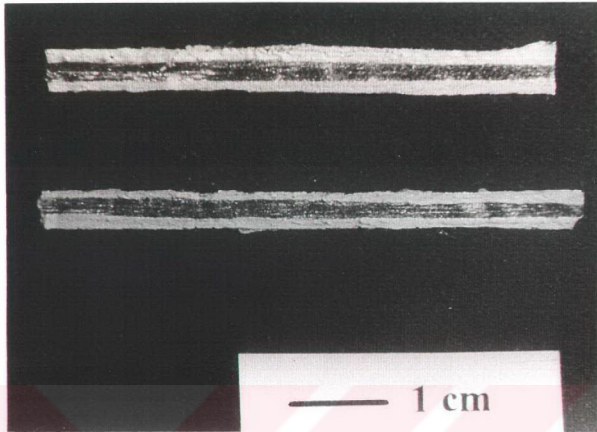


Figure 4.10 A free surface flow pattern showing turbulent spots produced by the orifice edges spreaded through the both sides of the central laminar flow. Thickness of the central region is noted as $30\ \mu\text{m}$.

In our experiments a few ribbon parts having no turbulent spots in its free surface are obtained extremely, so that it is impossible to distinguish the surfaces from the other. These completely uniform samples which are responsible by laminar flow have the same thickness noted as about $30\text{--}40\ \mu\text{m}$.

Finally, Kelvin-Helmholtz instability (see Figure 2.8 in section 2.2.4.3) can be observed characteristically along these ribbon edges almost in all figures as a result of the liquid/gas interaction.

4.1.6 Cooling Rates of Melt-Spun Ribbons

We know that the thickness of a melt-spun ribbon is related to its cooling rate, that is, decreasing the ribbon thickness increases the cooling rate. The cooling rates of the ribbons obtained by our melt-spinning operations can be measured roughly by considering Figure 2.11 showing Quench Rate versus Filament Thickness. It was assumed that, the cooling rates of the ribbons ranged from about 10^7 to 10^5 °C/s for thickness' of 30-250 μm .



4.2 X-Ray Diffraction Study

The X-Ray diffractograms obtained from the resultant flakes and ribbons are presented in Figures 4.12 to 4.19. Figures 4.12 (a) and 4.12 (b) display the x-ray pattern of the as-cast flakes of the alloy #1 which were produced without using pressure. This pattern was obtained from the computerized x-ray diffractometer with Cu K_α radiation and presented in Table A.1 (see Appendix A). All the other diffractograms obtained by using Co K_α radiation shows the x-ray patterns of the ribbons which were deposited by the alloys #2, 3 and 4 using with pressure.

The diffractogram in Figure 4.12 (b) is almost the same with the XRD patterns of RS Al-Fe-V-Si alloys in Figure 2.18 from the study of Tang *et.al.* [31]. Accordance with this study, the XRD patterns of RS Al-Fe-V-Si alloys in Figure 2.18 have α -Al reflections as well as the silicide dispersoids reflections. They also reported that silicide dispersoids have the same structure as the larger *i*-phase.

Phase analysis of rapidly solidified Al-Fe-V-Si alloy for the as-cast and heat treated ribbons is done to determine the crystal structure (shape and size of unit cell) of the alloy #2 and the results are tabulated in Table 4.2. This examination is done for only the four clear and more intense (fundamental) lines which are assumed to belong to Al. But the x-ray diffraction patterns obtained from second phase could not be indexed to any Bravais lattice. This result may confirmed the unindexable *i*-phase diffractions by XRD from the study of Shechtman *et.al* [19]

Table 4.2 Indexing x-ray patterns of the RS Al-Fe-V-Si alloy (# 2) in as cast and heat treated conditions. This analysis is done for four clear diffraction lines which are common in all diffractograms in figures 4.13 to 4.17.

Casting Conditions	Pattern of Unknown		Simple Cubic			Body Centered Cubic			Face Centered Cubic			Diamond Cubic			Least Square Method								
	2θ	$d(\text{\AA})$	h	k	l	h	k	l	h	k	l	h	k	l	S	$\lambda^2/4a^2$	$\cos^2\theta$	X	Y	$Y \cdot X$	X^2	$Y = a + bx$	
as-cast	1	44.75	100	2.350	0.1449	1 0 0	1	0.1449	1 1 1	3	0.0483	1 1 1	3	0.0483	0.7313	0.8551	3.4809	4.0705	3.4809	0.7313	4.0705	0.7313	
	2	52.20	23	2.033	0.1935	1 1 0	2	0.0967	2 0 0	4	0.0484	2 2 0	8	0.0242	0.6505	0.8065	3.2801	4.0670	3.2801	0.6505	4.0670	0.6505	
	3	77.22	16	1.434	0.3893	1 1 1	3	0.1298	2 1 1	6	0.0649	2 2 0	8	0.0354	0.3730	0.6107	2.4764	4.0548	2.4764	0.3730	4.0548	0.3730	4.0379
	4	93.97	17	1.223	0.5345	2 0 0	4	0.1336	2 2 0	8	0.0668	3 1 1	11	0.0334	0.2167	0.4655	1.8891	4.0578	1.8891	0.2167	4.0578	0.2167	
	Σ															2.7379	11.1264	16.2501	11.1264	1.9715			
200°C - 1h	1	44.92	100	2.342	0.1459	1 0 0	1	0.1459	1 1 1	3	0.0486	1 1 1	3	0.0486	0.7295	0.8541	3.4641	4.0559	3.4641	0.7295	4.0559	0.7295	
	2	52.32	31	2.029	0.1943	1 1 0	2	0.0972	2 0 0	4	0.0486	2 2 0	8	0.0243	0.6491	0.8057	3.2697	4.0583	3.2697	0.6491	4.0583	0.6491	
	3	77.25	27	1.433	0.3895	1 1 1	3	0.1298	2 1 1	6	0.0649	2 2 0	8	0.0354	0.3727	0.6105	2.4746	4.0535	2.4746	0.3727	4.0535	0.3727	4.0455
	4	94.15	33	1.222	0.5360	2 0 0	4	0.1340	2 2 0	8	0.0670	3 1 1	11	0.0335	0.2153	0.4640	1.8800	4.0519	1.8800	0.2153	4.0519	0.2153	
	Σ															2.7342	11.0884	16.2196	11.0884	1.9666			
300°C - 1h	1	45.07	100	2.334	0.1468	1 0 0	1	0.1468	1 1 1	3	0.0489	1 1 1	3	0.0489	0.7279	0.8532	3.4495	4.0431	3.4495	0.7279	4.0431	0.7279	
	2	52.40	28	2.026	0.1949	1 1 0	2	0.0974	2 0 0	4	0.0487	2 2 0	8	0.0244	0.6483	0.8051	3.2629	4.0525	3.2629	0.6483	4.0525	0.6483	
	3	77.40	31	1.431	0.3908	1 1 1	3	0.1303	2 1 1	6	0.0651	2 2 0	8	0.0355	0.3711	0.6092	2.4653	4.0469	2.4653	0.3711	4.0469	0.3711	4.0472
	4	94.30	34	1.220	0.5373	2 0 0	4	0.1343	2 2 0	8	0.0672	3 1 1	11	0.0336	0.2141	0.4627	1.8724	4.0470	1.8724	0.2141	4.0470	0.2141	
	Σ															2.7302	11.0501	16.1895	11.0501	1.9613			
400°C - 1h	1	44.90	100	2.343	0.1458	1 0 0	1	0.1458	1 1 1	3	0.0486	1 1 1	3	0.0486	0.7297	0.8542	3.4661	4.0576	3.4661	0.7297	4.0576	0.7297	
	2	52.25	28	2.032	0.1938	1 1 0	2	0.0969	2 0 0	4	0.0485	2 2 0	8	0.0242	0.6499	0.8062	3.2758	4.0633	3.2758	0.6499	4.0633	0.6499	
	3	77.25	18	1.433	0.3895	1 1 1	3	0.1298	2 1 1	6	0.0649	2 2 0	8	0.0354	0.3727	0.6105	2.4746	4.0535	2.4746	0.3727	4.0535	0.3727	4.0514
	4	93.97	22	1.223	0.5345	2 0 0	4	0.1336	2 2 0	8	0.0668	3 1 1	11	0.0334	0.2167	0.4655	1.8891	4.0578	1.8891	0.2167	4.0578	0.2167	
	Σ															2.7364	11.1055	16.2323	11.1055	1.9690			
500°C - 1h	1	44.98	100	2.339	0.1463	1 0 0	1	0.1463	1 1 1	3	0.0488	1 1 1	3	0.0488	0.7289	0.8537	3.4583	4.0508	3.4583	0.7289	4.0508	0.7289	
	2	52.44	19	2.025	0.1951	1 1 0	2	0.0976	2 0 0	4	0.0488	2 2 0	8	0.0244	0.6478	0.8049	3.2594	4.0497	3.2594	0.6478	4.0497	0.6478	
	3	77.29	16	1.433	0.3899	1 1 1	3	0.1300	2 1 1	6	0.0650	2 2 0	8	0.0354	0.3723	0.6101	2.4721	4.0517	2.4721	0.3723	4.0517	0.3723	4.0542
	4	94.15	19	1.222	0.5360	2 0 0	4	0.1340	2 2 0	8	0.0670	3 1 1	11	0.0335	0.2153	0.4640	1.8800	4.0519	1.8800	0.2153	4.0519	0.2153	
	Σ															2.7327	11.0697	16.2041	11.0697	1.9642			

4.2.1 Indexing Pattern of Unknown For Cubic Crystals

Table 4.2 shows identification of the unknown patterns and indexing these patterns for well known cubic crystals. The four clear and more intense diffraction lines were observed commonly in all studied diffractograms.

The values of angular positions (2θ) and the observed relative intensities (I/I_1) of these diffraction lines were obtained from the diffractograms. The d value of each line which is the distance between adjacent planes in the set hkl was also calculated by using the Bragg law ($\lambda=2d\sin\theta$). Then those are written down to get the columns of Pattern of Unknown. After the pattern is obtained, the value of $\sin^2\theta$ can be calculated for each diffraction line. This set of $\sin^2\theta$ values is starting data for the determination of cell size and shape.

It is well known that a cubic crystal gives diffraction lines whose $\sin^2\theta$ values satisfy the following equation:

$$\sin^2\theta / h^2+k^2+l^2 = \sin^2\theta / S = \lambda^2 / 4a^2 \dots\dots\dots (17)$$

This equation can be obtained by combining the Bragg law with the plane-spacing equation for a cubic system, as seen in Table B.1 (see Appendix B) [38]. For a particular incident wavelength λ and a particular cubic crystal of a unit cell size a , it is clear that the quotient of $\lambda^2/4a^2$ value is a constant for any one pattern. X-ray

diffraction study for phase identification was performed using monochromated Co K α radiation. Aluminum matrix reflections were assumed to be yielding $a = 4.0494 \text{ \AA}$ (see Appendix B, Table B.2 [41]) for calculations.

Each of the four common cubic lattice types (SC, BCC, FCC, DC) has a characteristic sequence of diffraction lines and it is described by their sequential S values. The proper set of integers S and the corresponding indices hkl for each diffraction line are written down for the cubic structures in Table B.3 (see Appendix B) [38].

To identify the unknown phase peaks, the observed $\sin^2\theta$ values are divided one by one into the integers S which is the sum of three squared integers of hkl given in Equation 17 to yield a constant quotient for one of the four cubic lattice types. After the computations, the value of $\lambda^2/4a^2$ for each pattern is constant for only FCC lattice type. The a column in the table lists the lattice parameter calculated from each line position. The systematic error in $\sin^2\theta$ shows up as a gradual increase or variation in the value of $\lambda^2/4a^2$, and a gradual decrease or variation in the value of a , as θ increases. Therefore, the lattice parameter was measured precisely by using the Method of Least Square and the results were listed in the a_0 column.

As a result of above analysis, patterns of all the unknown samples were found to be as similar to FCC. But the presence of a high degree of lattice distortion due to very high quench rate can be considered particularly in as-cast condition. Figure 4.11

shows the variation of calculated lattice parameter with temperature. Heat treatment relieves the lattice stresses resulting in a reduction of the lattice parameter of Al. In addition, line intensity peak heights get longer gradually as a result of the stress relief provided by the heat treatment. (see Figures 4.13 to 4.17)

The relative intensities of the diffractogram from melt-spun flakes in Figure 4.12 (a) is very similar to the relative intensities of aluminum as seen in Table B.2 (see Appendix B). However, there is a considerable distortion in the relative intensities of aluminum diffraction lines obtained from all the melt-spun ribbons in Figures 4.13 to 4.19. After this observation we have concluded that the continuous jet flow of the molten by means of the pressure is another factor causing the lattice distortion.

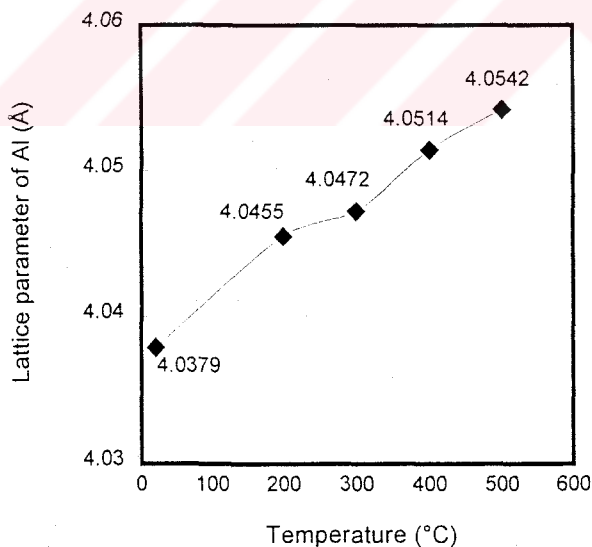


Figure 4.11 The effect of temperature on lattice parameter of Al from the melt-spun ribbons of Al-Fe-V-Si alloy (#2).

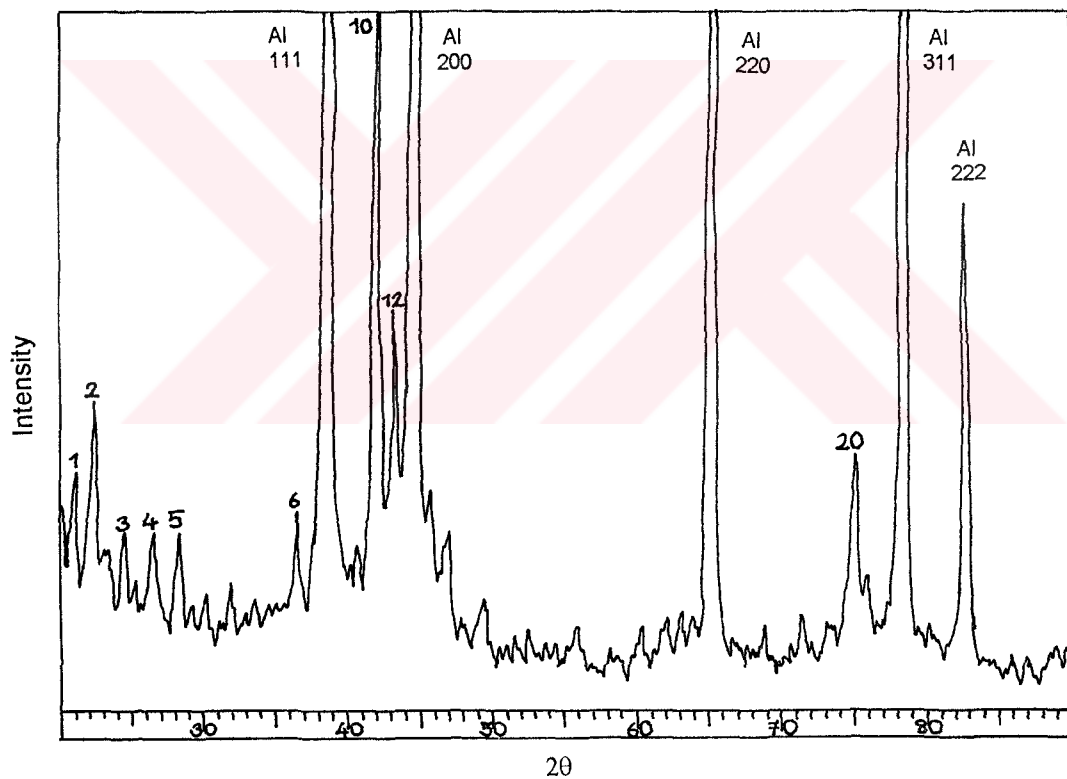
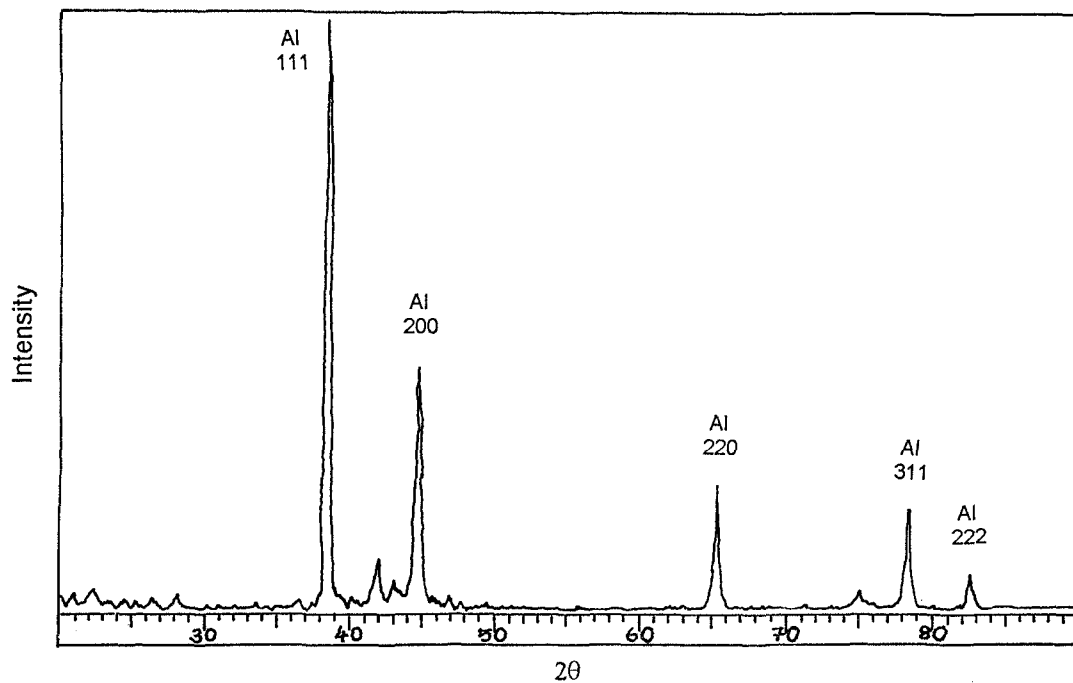


Figure 4.12 (a) X-ray diffractogram from melt-spun flake of Al-Fe-V-Si alloy (#1) in as-cast condition. (b) The same as (a) with the intensity shown by using a more sensitive scale.

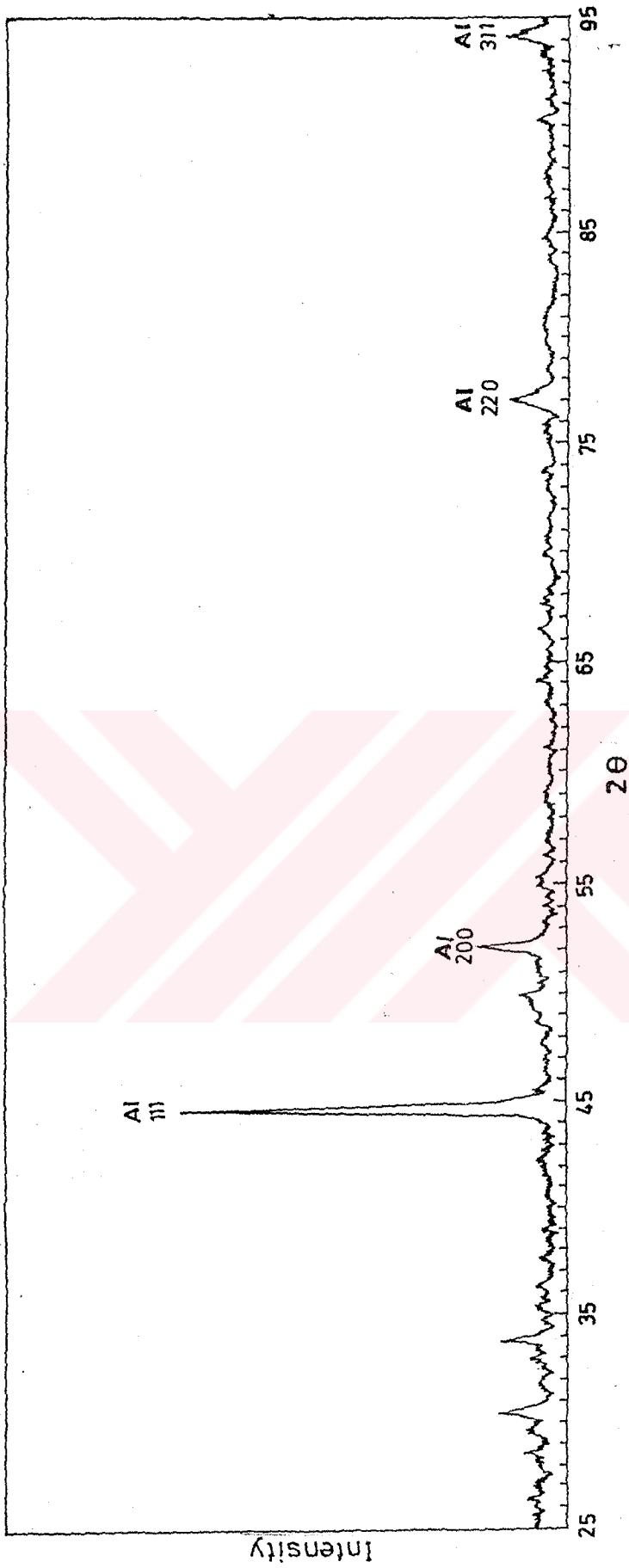


Figure 4.13 X-ray diffractogram from melt-spun ribbon of Al-Fe-V-Si alloy (# 2) in as-cast condition.

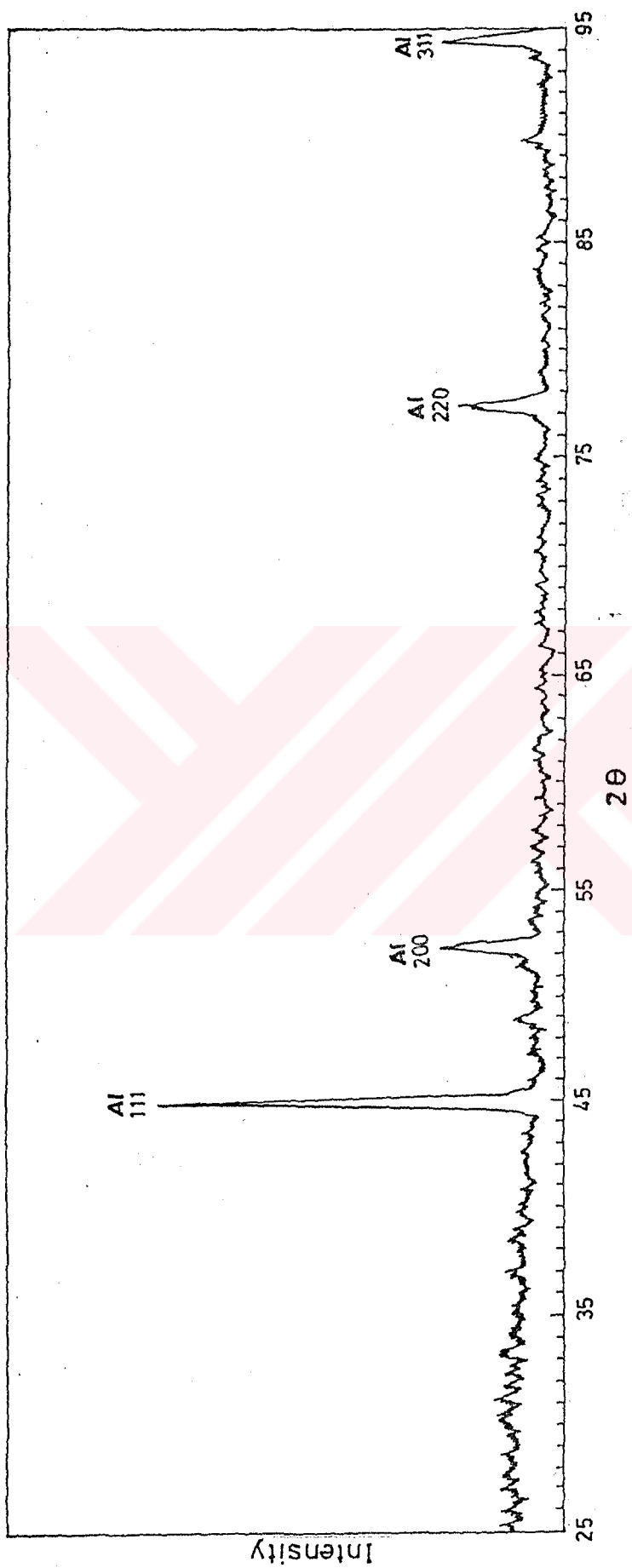


Figure 4.14 X-ray diffractogram from melt-spun ribbon of Al-Fe-V-Si alloy (# 2) in heat treated condition at 200°C for 1 hour.

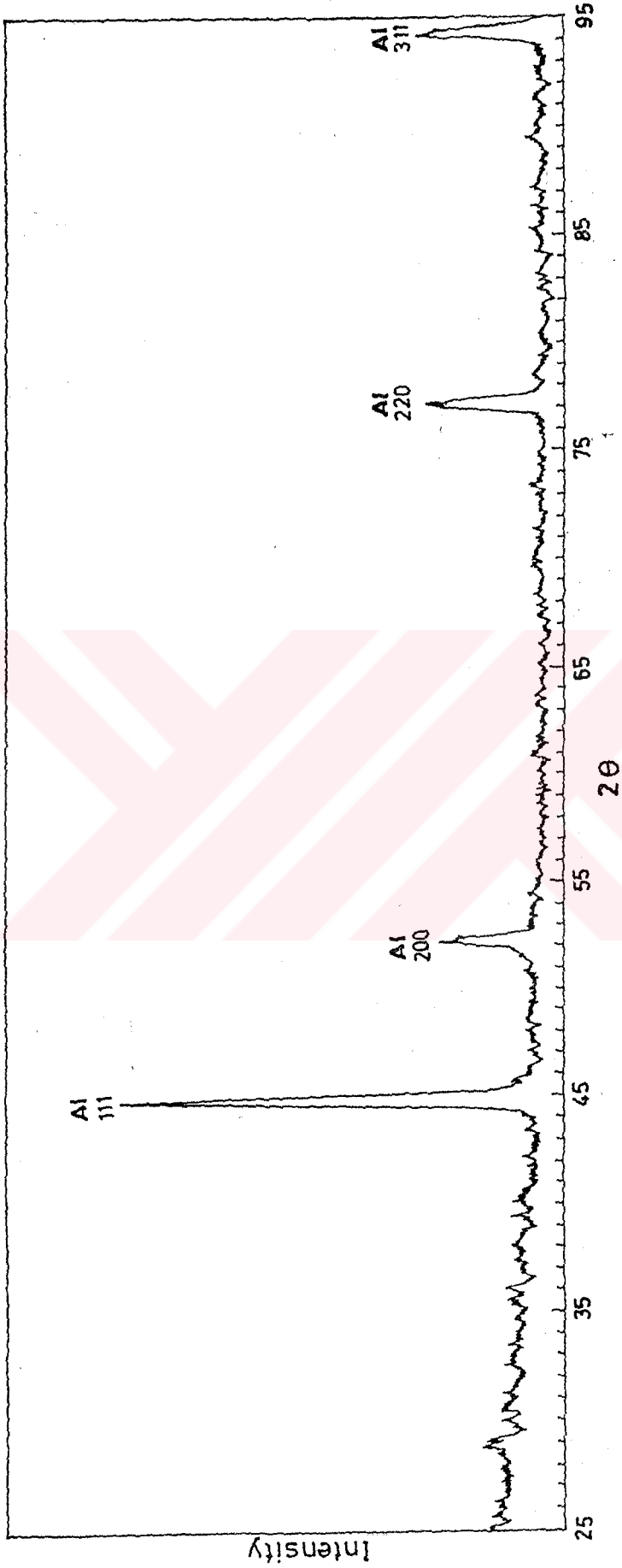


Figure 4.15 X-ray diffractogram from melt-spun ribbon of Al-Fe-V-Si alloy (# 2) in heat treated condition at 300°C for 1 hour.

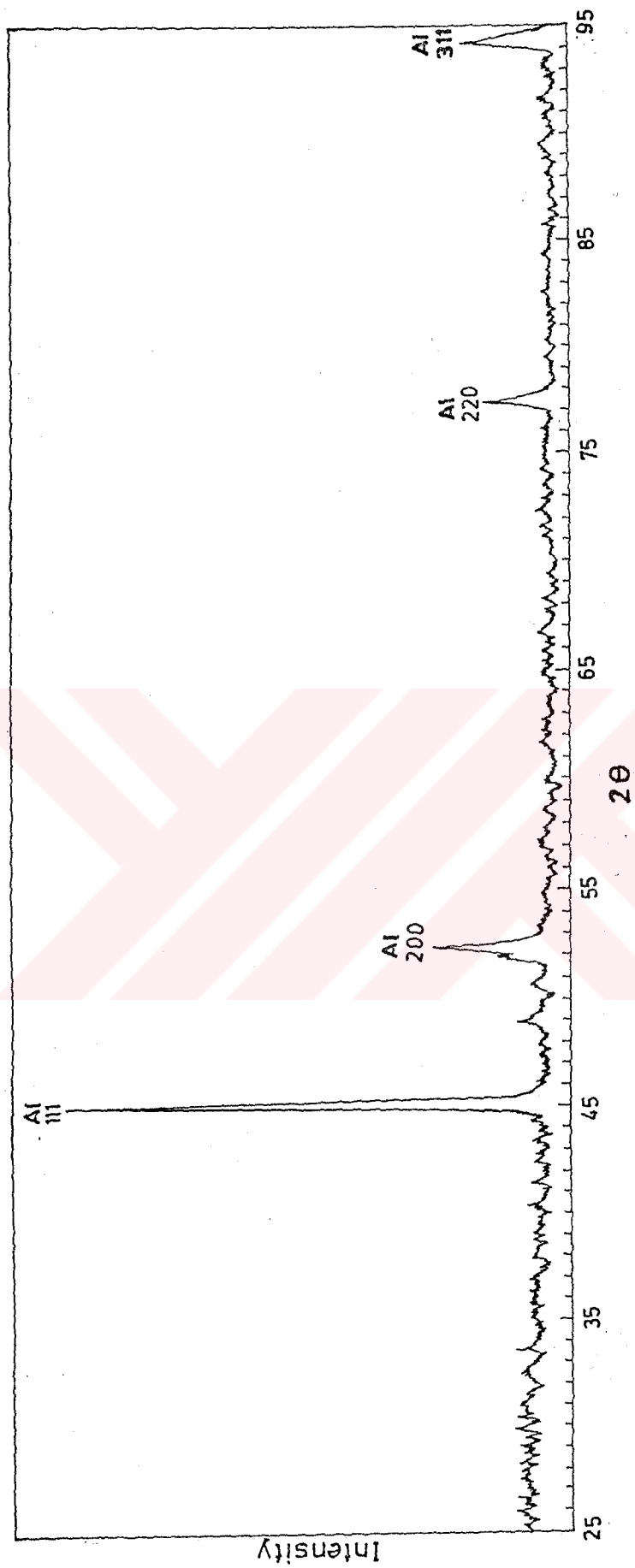


Figure 4.16 X-ray diffractogram from melt-spun ribbon of Al-Fe-V-Si alloy (# 2) in heat treated condition at 400°C for 1 hour.

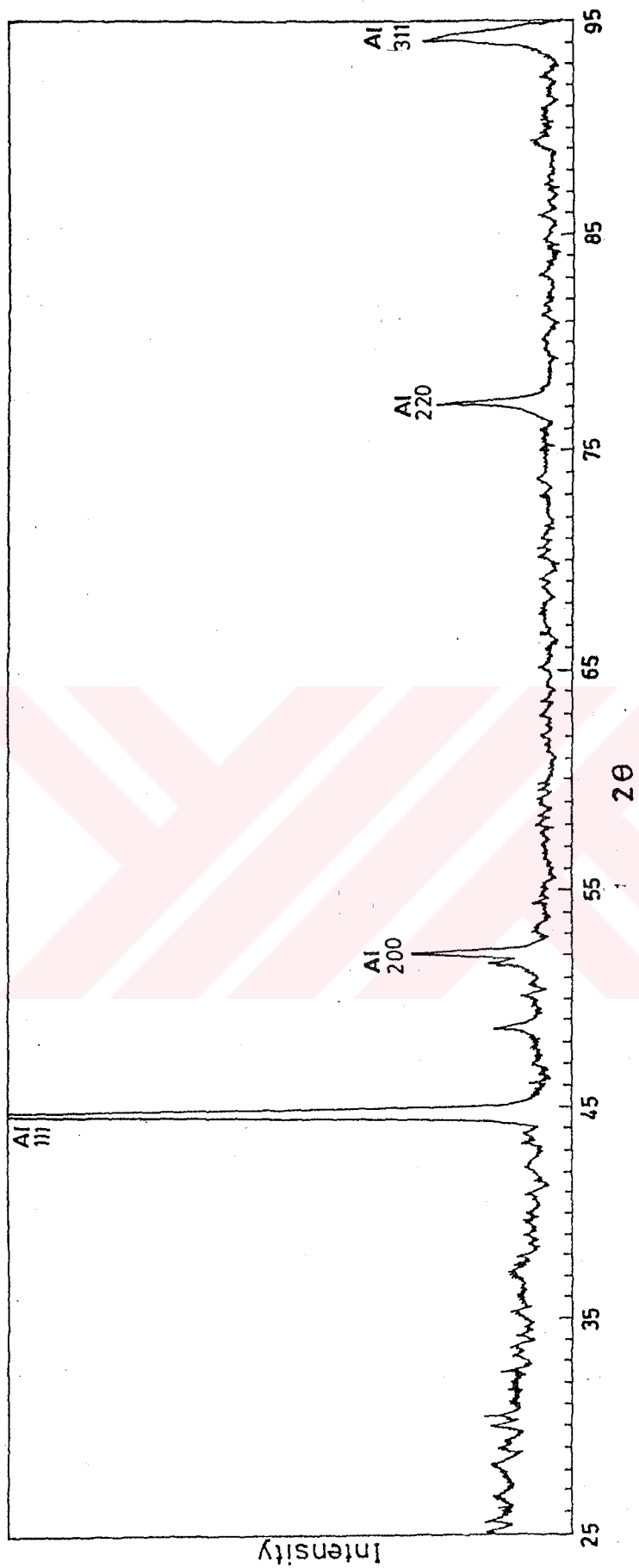


Figure 4.17 X-ray diffractogram from melt-spun ribbon of Al-Fe-V-Si alloy (# 2) in heat treated condition at 500°C for 1 hour.

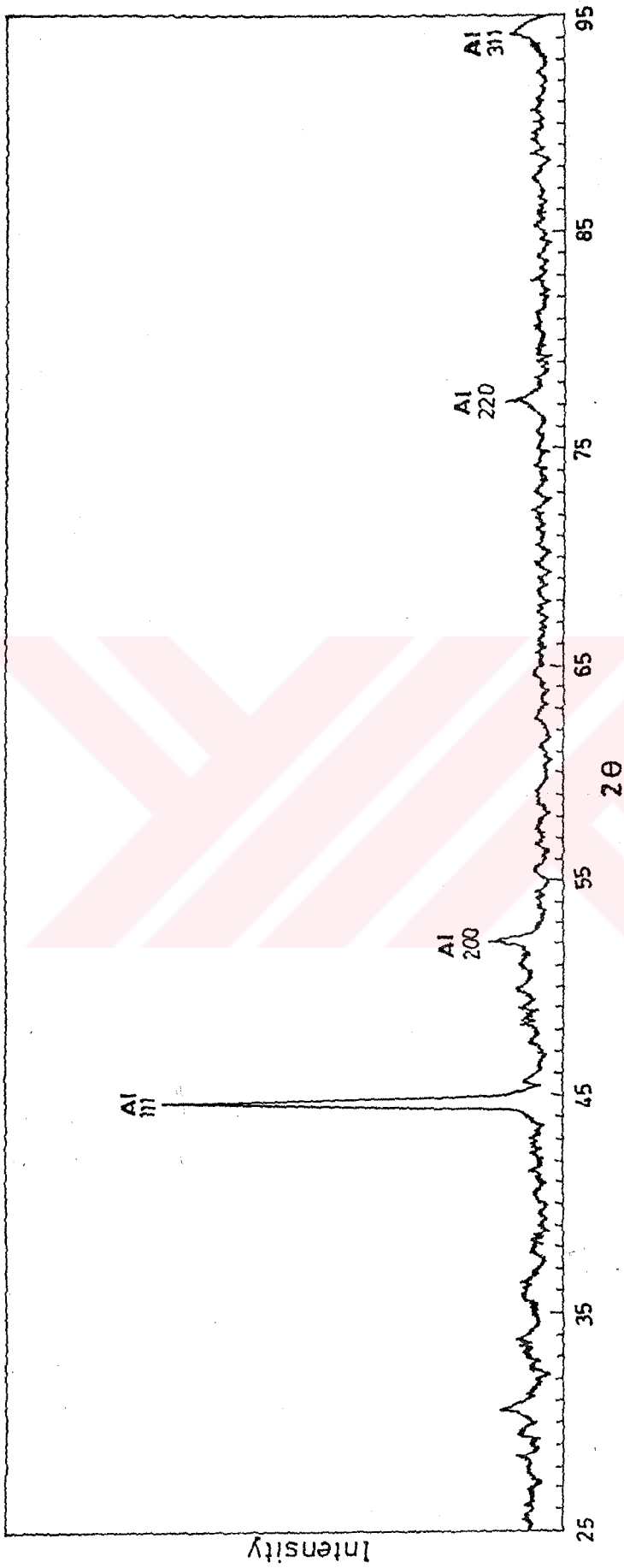


Figure 4.18 X-ray diffractogram from melt-spun ribbon of Al-Fe-V-Si alloy (# 3) in as-cast condition.

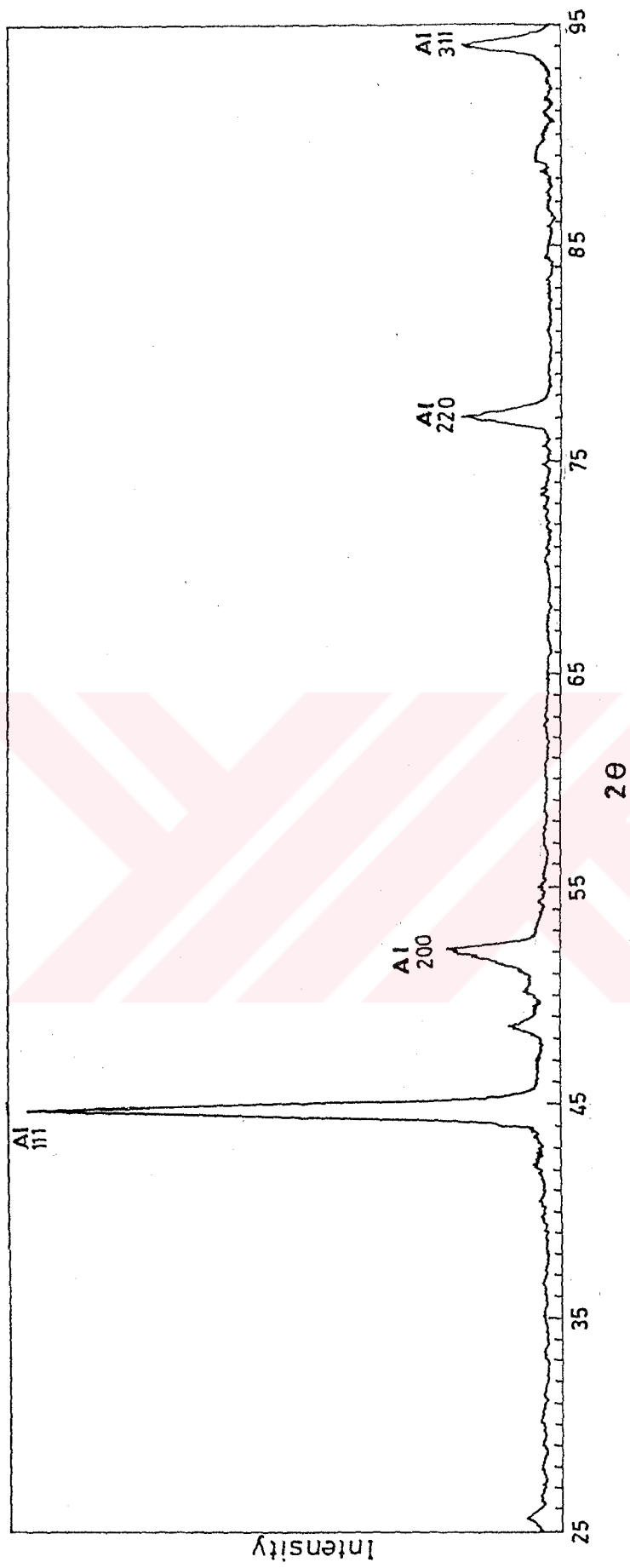


Figure 4.19 X-ray diffractogram from melt-spun ribbon of Al-Fe-V-Si alloy (# 4) in as-cast condition.

4.3 SEM Study

4.3.1 Chemical Compositions of Studied Alloys

The overall chemical compositions of the RS Al-Fe-V-Si alloys are given in Table 4.3. Energy Dispersive Spectrum (EDS) area analysis performed on the large area of the alloy samples confirmed the desired alloy composition. There is only a considerable disagreement in vanadium percentage for the alloy # 4 given in Table 4.3. However, the point analysis performed by EDS didn't show the dispersoid phase composition peaks due to too small particle size. Some reflections coming from the Al matrix were detected besides dispersoid peaks.

Table 4.3 Chemical compositions of studied RS Al-Fe-V-Si alloys in as-cast conditions.

# of alloy	Chemical Compositions (wt%)			
	Al	Fe	V	Si
1	89.20	7.55	1.03	2.21
2	89.07	7.72	1.31	1.89
3	88.03	6.84	3.07	2.05
4	88.70	7.86	1.76	1.68

4.3.2 Microstructural Refinement by Rapid Solidification

It is expected that a high degree of microstructural refinement can be obtained by rapid solidification. The SEM micrograph in Figure 4.20 displays the

microstructure of conventionally solidified (cooled down slowly) Al-Fe-V-Si alloy. It is seen apparently in the figure that, there is no chemical homogeneity in the microstructure, but high degree of segregation and may be complex constituent phases due to non extension of solubilities of alloying elements. However, all the other SEM micrographs from melt-spun ribbons, for example Figure 4.21, reveal that a high degree of microstructural refinement due to rapid cooling. All as-cast melt-spun ribbons contain 0.05 to 0.5 μm rounded second phase particles (may be silicides) homogeneously distributed throughout the Al matrix. This homogeneous and fine distribution of second phase in Al matrix is an evidence of extended solid solubility by rapid solidification. Approximately 10-16 % volume fraction of second phase was detected by x-ray examination on contrary 27% theoretically expected value. That much volume fraction of these second phase may be another result of solid solubility extension achieved by rapid solidification.

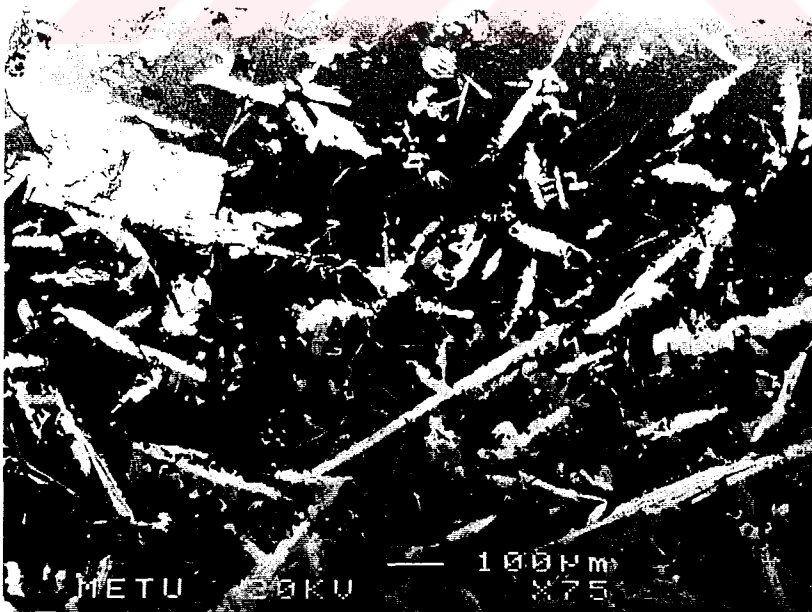


Figure 4.20 SEM micrograph from conventional cast ingot of Al-Fe-V-Si alloy.

4.3.3 Microstructural Examination of Melt-Spun Flakes and Ribbons

SEM micrograph of a cross section of the melt-spun ribbon in Figure 4.21 shows a variation in microstructure. This figure compares the chill side microstructure with the air side one of a ribbon. In melt-spinning casting, the heat is extracted at a faster rate from the molten surface in direct contact with the spinning wheel than the surface exposed to the air. The difference in heat extraction rate results in a finer microstructure at the chill side compared to that in the air side of the ribbon. The air side of the ribbon exhibits coarser dispersoids as shown in the micrograph.

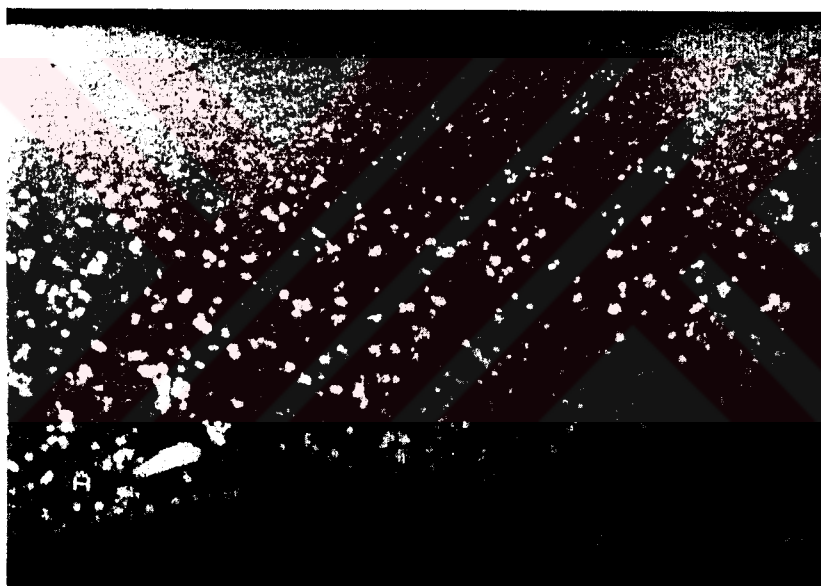


Figure 4.21 SEM micrograph from melt-spun ribbon showing variation in microstructure from the chill (C) and the air (A) side.

SEM micrographs from the polished chiller sides of melt-spun flakes and ribbons in both as-cast and heat-treated conditions are presented in Figures 4.22 to 4.28.

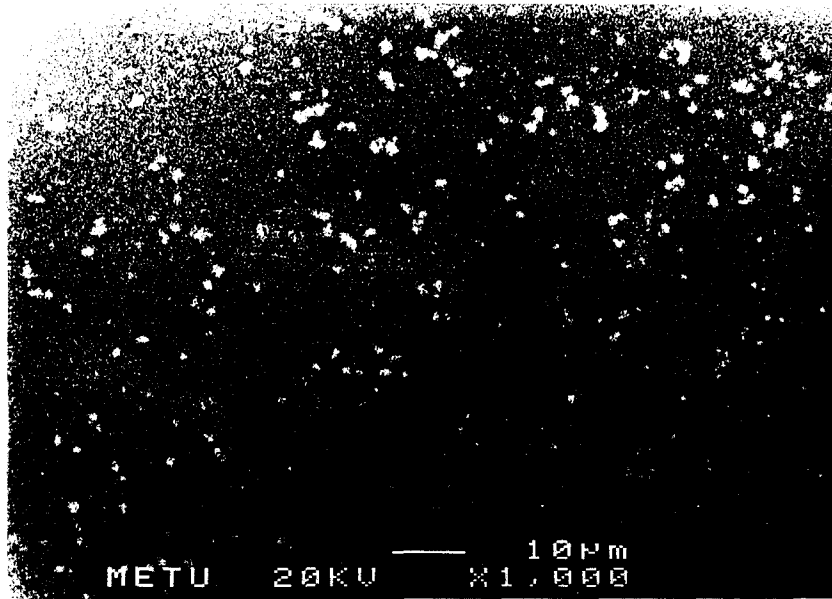


Figure 4.22 SEM micrograph from melt-spun flake in as-cast condition showing fine and uniformly distributed second phase particles in Al matrix.

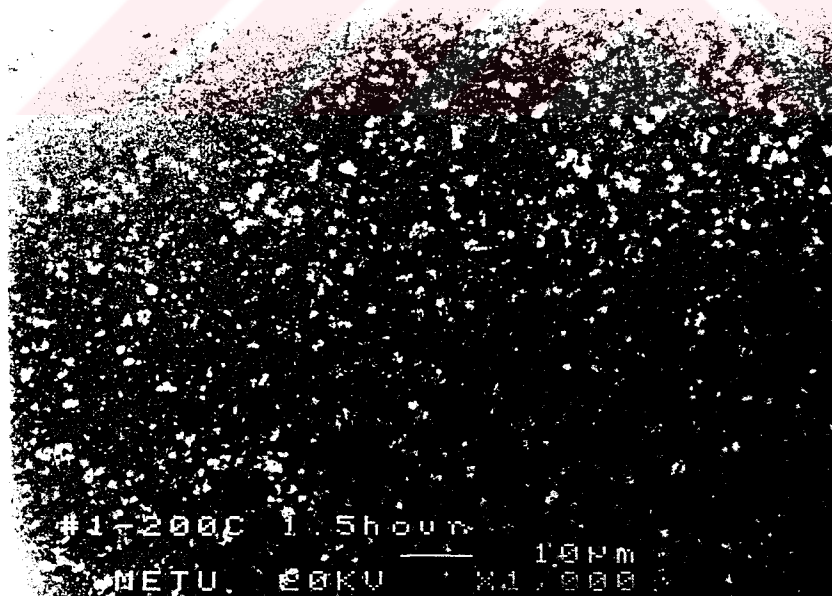


Figure 4.23 SEM micrograph from melt-spun flake in heat treated at 200 °C for 1.5 hours showing fine and uniformly distributed second phase particles in Al matrix.

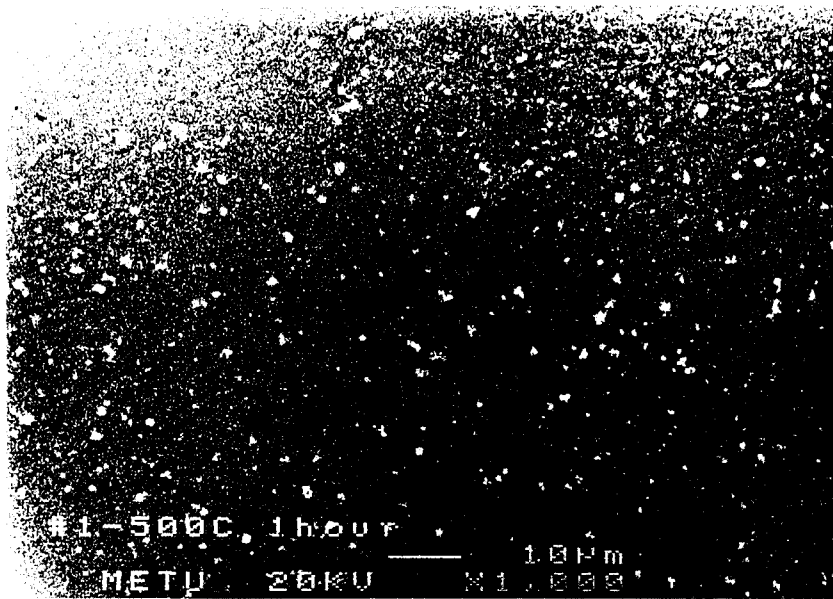


Figure 4.24 SEM micrograph from melt-spun flake in heat treated at 500 °C for 1 hour showing fine and uniformly distributed second phase particles in Al matrix.



Figure 4.25 SEM micrograph from melt-spun flake in heat treated at 500 °C for 3 hours showing fine and uniformly distributed second phase particles in Al matrix.

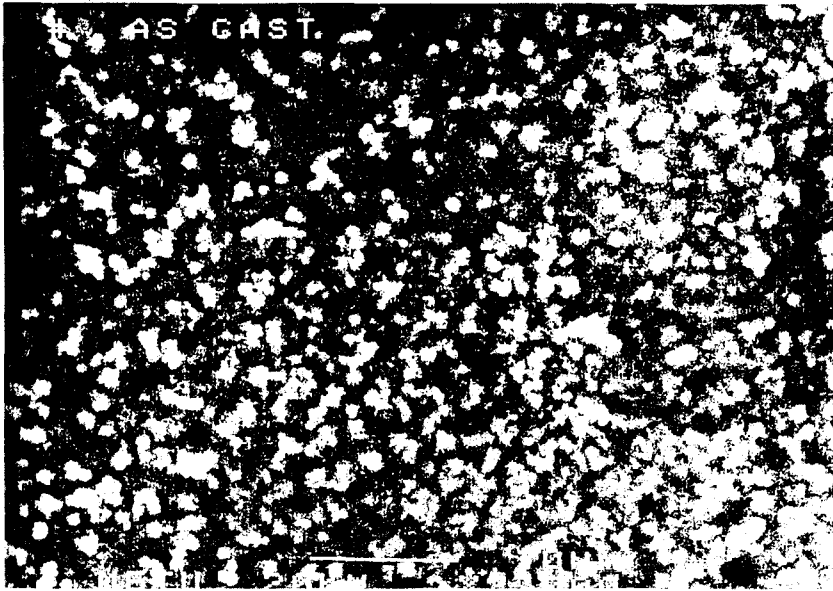


Figure 4.26 SEM micrograph from melt-spun ribbon in as-cast condition showing fine and uniformly distributed second phase particles in Al matrix.

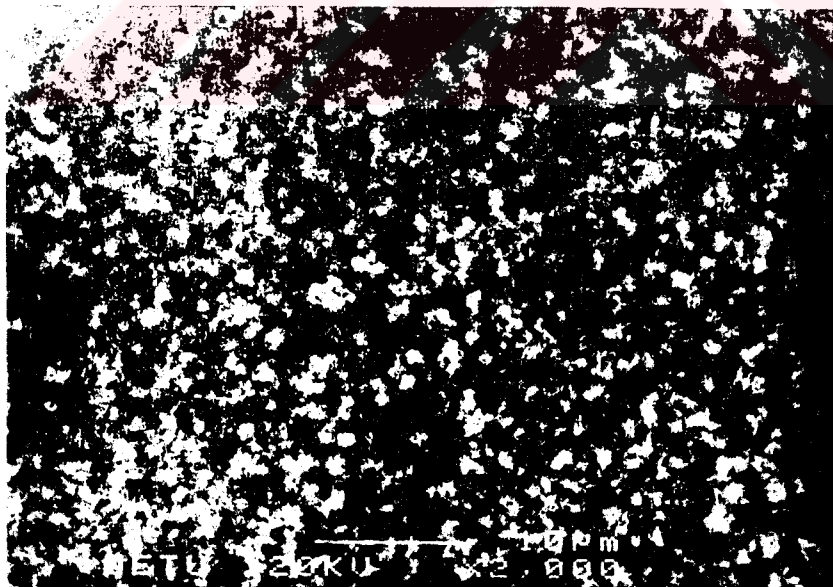


Figure 4.27 SEM micrograph from melt-spun ribbon in heat treated at 400 °C for 1 hour showing fine and uniformly distributed second phase particles in Al matrix.

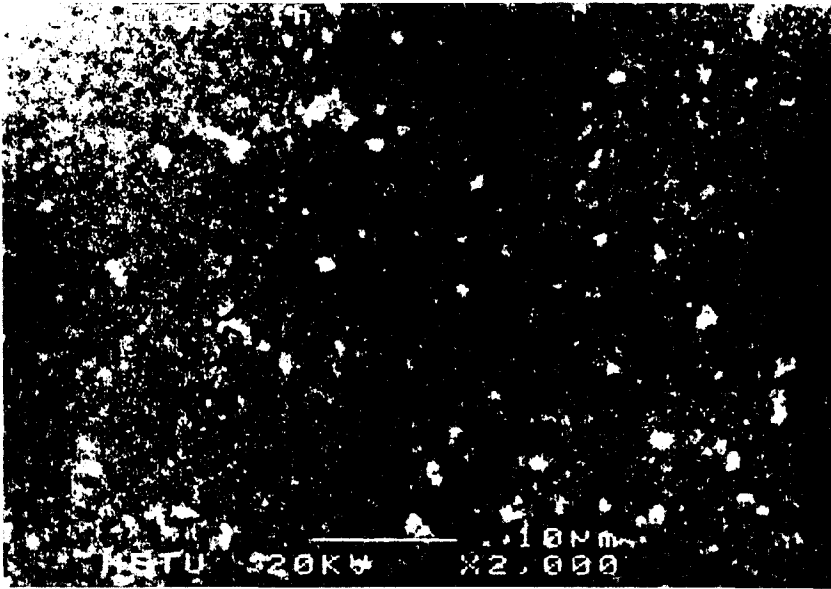


Figure 4.28 SEM micrograph from melt-spun ribbon in heat treated at 500 °C for 1 hour showing fine and uniformly distributed second phase particles in Al matrix.

These micrographs show that the particle coarsening at a temperature range 150 to 500 °C is not considerable. It is the evidence of high temperature stability of the examined alloys. This results also support the dispersed phase which is unindexable by x-ray diffraction may be a cubic phase as reported by Skinner *et al.* [14].

EDS analysis's of some melt-spun flakes and ribbons are presented in Figures 4.29 to 4.32.

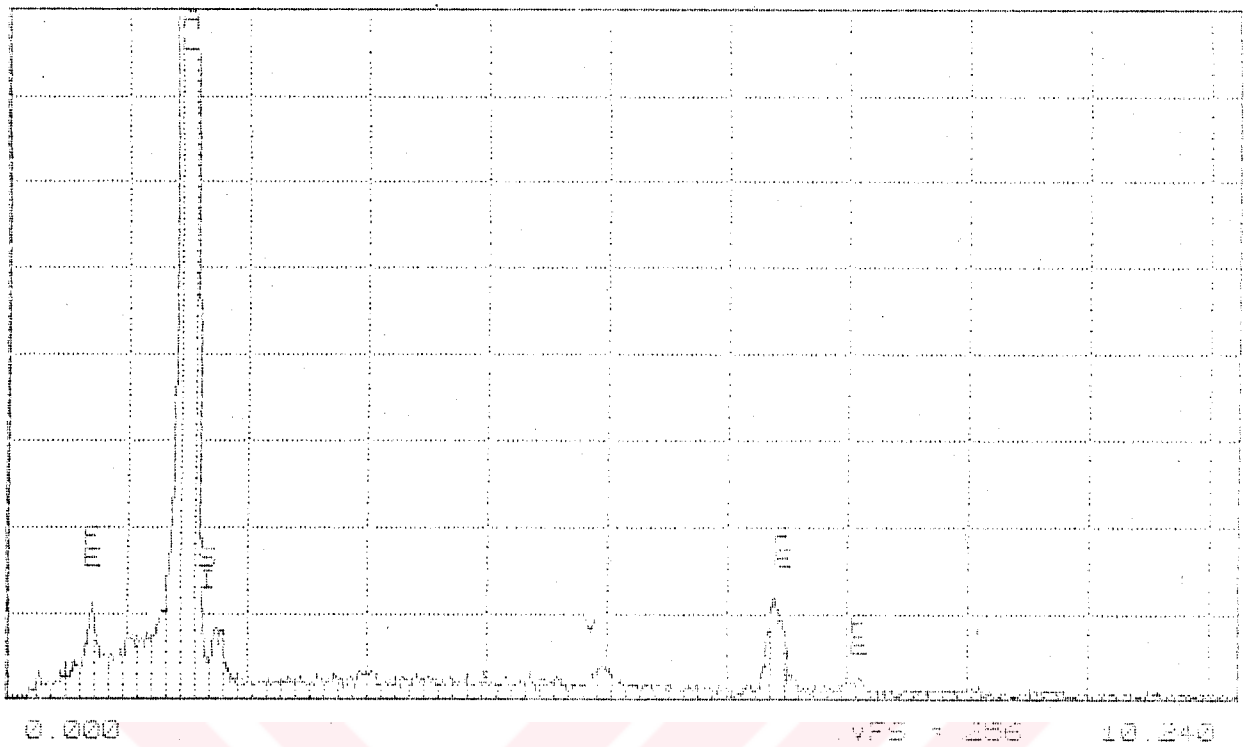


Figure 4.29 EDS analysis of the melt-spun flake indicated in Figure 4.22.

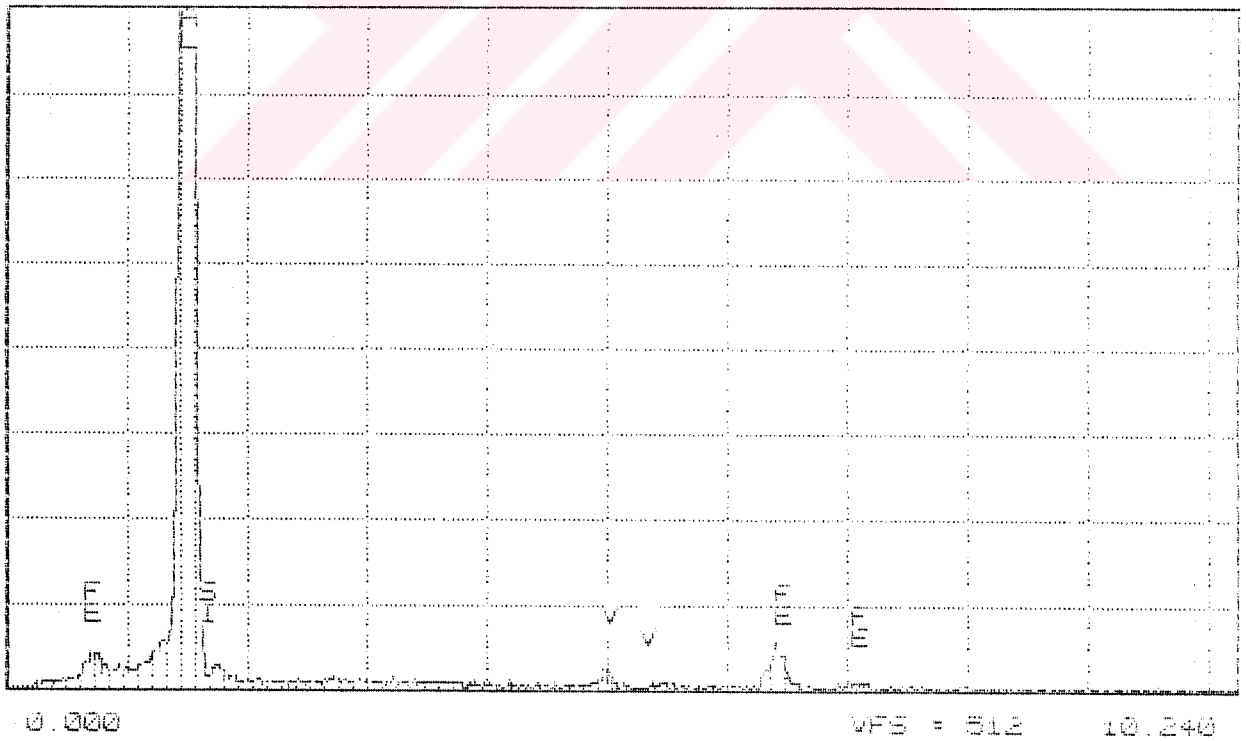


Figure 4.30 EDS analysis of the melt-spun flake indicated in Figure 4.26.

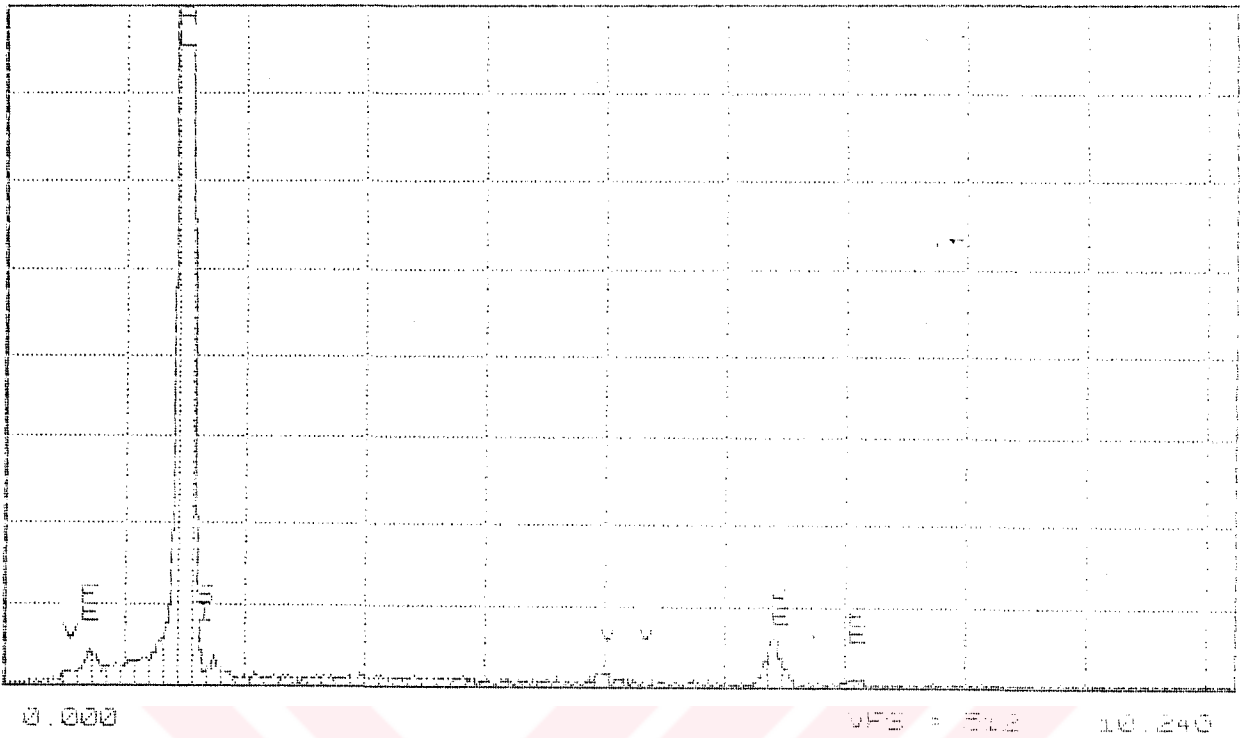


Figure 4.31 EDS analysis of the melt-spun flake indicated in Figure 4.27.

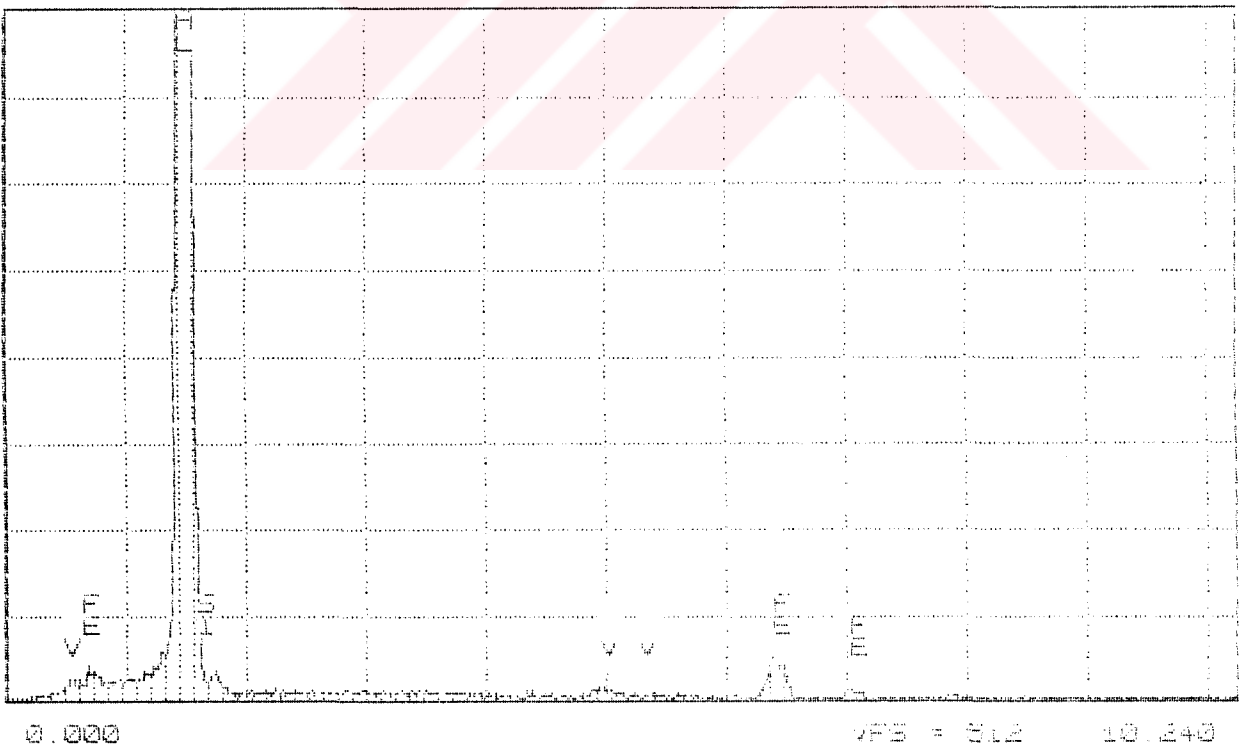


Figure 4.32 EDS analysis of the melt-spun flake indicated in Figure 4.28.

4.3.4 Solubility Limit

It is well known that the transition metals such as Fe and V have very low equilibrium solid solubilities in aluminum as well as diffusion rates. Both factors are essential in developing high temperature aluminum alloys and therefore, such alloys have to involve at least one transition metal to obtain high temperature stability through rapid solidification processes as mentioned about in detail in Chapter 2. John in his study [13] was demonstrated that rapid cooling could result in the extension of the solid solubility of iron in aluminum from 0.05 to about 10 weight percentage. In all the other RS studies with Al-Fe-V-Si alloys, the total amount of transition metals (Fe+V) was designed from 7.1 to 12.9 in wt%.

The solid solubility extension by rapid cooling is also proved in our melt-spinning experiments for the studied alloys. However, as reported in Table 4.3 there is a considerable disagreement in the overall composition for the alloy # 4. EDS analysis showed that the vanadium is 1.76 in weight percentage while the desired one is 3.70. SEM micrograph seen in Figure 4.33 explains this unexpected result. The rest of the vanadium which is not dissolved in aluminum matrix formed the large precipitations with very different compositions (see Figure 4.34). The large white points indicated in Figure 4.33 are these precipitates rich in vanadium.

If we compare the compositions of the studied alloy #4 with the RS Al-Fe-V-Si alloys presented in Table 1.4, we can easily see that the vanadium percentage of

alloy #4 is out of the nominal compositions of the designed alloys while the sum of Fe and V is in the suitable limit.

Consequently, the achieved cooling rate is not adequate to solve that much amount of vanadium for the studied alloy #4. The cooling rate for the melt-spun ribbons obtained from the alloy #4 was assumed as the slowest one (about 10^5 °C/s) depending on its thickness measured as about 250 μm .

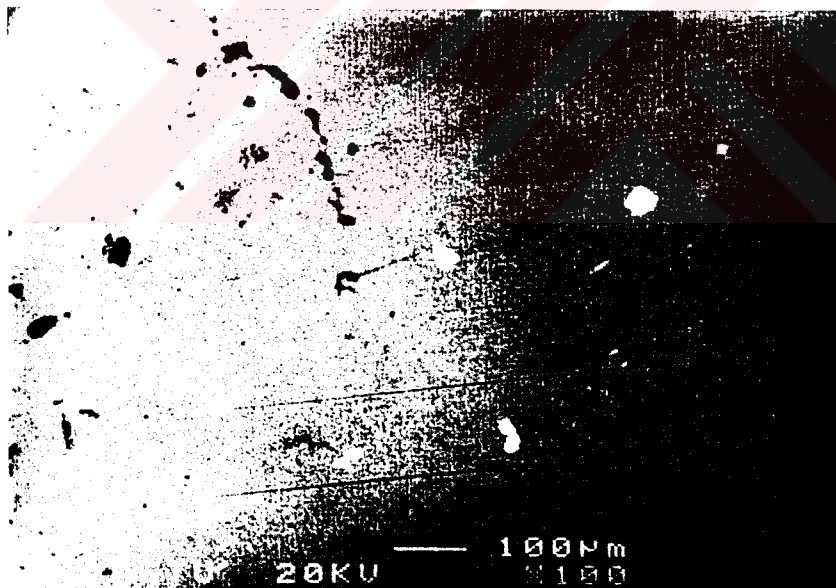
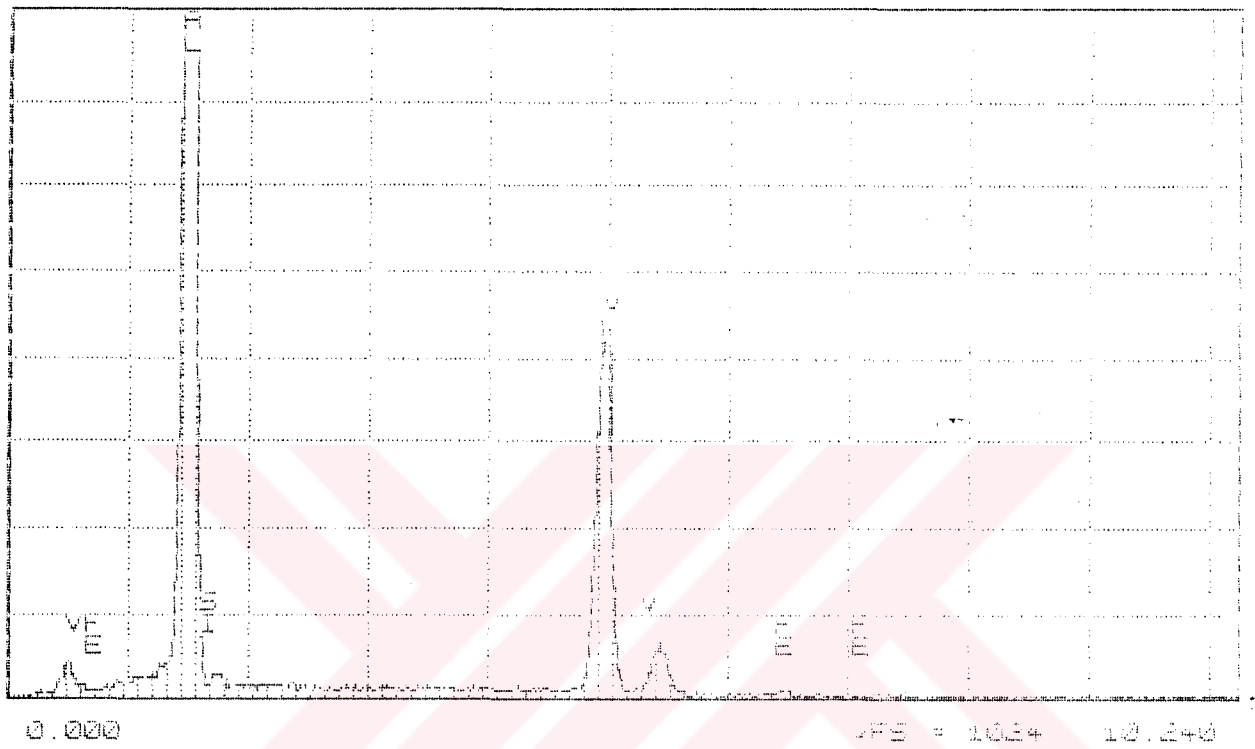


Figure 4.33 SEM micrograph from the melt-spun ribbon of the alloy #4. Note that its cooling rate is the slowest value, 10^5 °C/s, depending on the thickness.



Element	Chemical Composition (wt%)
Al	62.68
Fe	0.34
V	36.28
Si	0.71

Figure 4.34 EDS analysis of the white points indicated in Figure 4.33.

4.4 TEM Study

Transmission electron microscopy examination revealed that rapidly solidified Al-Fe-V-Si alloys have characteristically cellular type morphology. In addition, the second phase particles are observed to decorate the cell boundaries. The diffraction patterns obtained from the cells can be indexed as FCC type structure of aluminum. This result also supports the XRD examination. The diffraction patterns of the second phase particles which are unindexable by XRD revealed that these dispersoids have ordered BCC type structure. After that, we can easily say that the dispersed phase decorating the Al cell boundaries is a silicide phase which has been firstly observed by Skinner *et al* [14]. (The figures showing the indexable diffraction patterns of both aluminum and silicide dispersoids are presented at the end of this section.) Thus, the microstructure of RS Al-Fe-V-Si alloy is characterized by a fine dispersion of silicide phase in the aluminium matrix. However, the result of rapid solidification exhibited considerable variation in the microstructure of the studied alloys as it will be discussed later.

The microstructural examination is done for the as-cast ribbons with three different thickness' (30, 98 and 250 μm) obtained from the alloys # 2 and # 4. Only the heat-treated ribbons about 98 μm in thickness obtained from the alloy # 2 are examined for the effect of heat treatment on RS Al-Fe-V-Si alloy's microstructure.

It is well known that rapid solidification provides to achieve refined grain size, increased chemical homogeneity, extended solid solubility. In general, all these

features requires higher degree of solidification rate which is strictly related to the ribbon thickness.

4.4.1 Effect of Cooling Rate on Cell and Particle Size

Figures 4.35 to 4.38 display the similar microcellular structures, which are comprised of nearly spherical ultrafine silicide dispersoids in aluminum matrix, obtained from the melt-spun ribbons with three different average thickness. Figure 4.35 and 4.36, in turn, are used to measure the particle size and the cell size for the ribbon thickness of 30 μm . The other two TEM micrographs in Figures 4.37 and 4.38 are evaluated for the measurements of both cell and particle size for the ribbon thickness' of 98 and 250 μm respectively. The results are tabulated in Table 4.4. Figure 4.39 shows the effect of ribbon thickness (solidification rate) on average cell and particle size graphically. As it is seen clearly in these figures and table, cell size increases clearly with ribbon thickness while the size of intercellular silicide particles remains almost constant in the studied cooling range. Thus, the ribbon thickness is an indication of degree of cooling rate controlling the microstructural cell size. Note that these dispersoids have the same size with the $\text{Al}_{12}(\text{Fe},\text{V})_3\text{Si}$ intermetallic dispersoids indicated in Figure 2.15.

Table 4.4 Effect of ribbon thickness on cell and particle size.

Ribbon Thickness (μm)	Cell Size (μm)	Particle Size (μm)
30	0.08	0.02 - 0.04
98	0.45	0.02 - 0.05
250	0.60	0.02 - 0.06

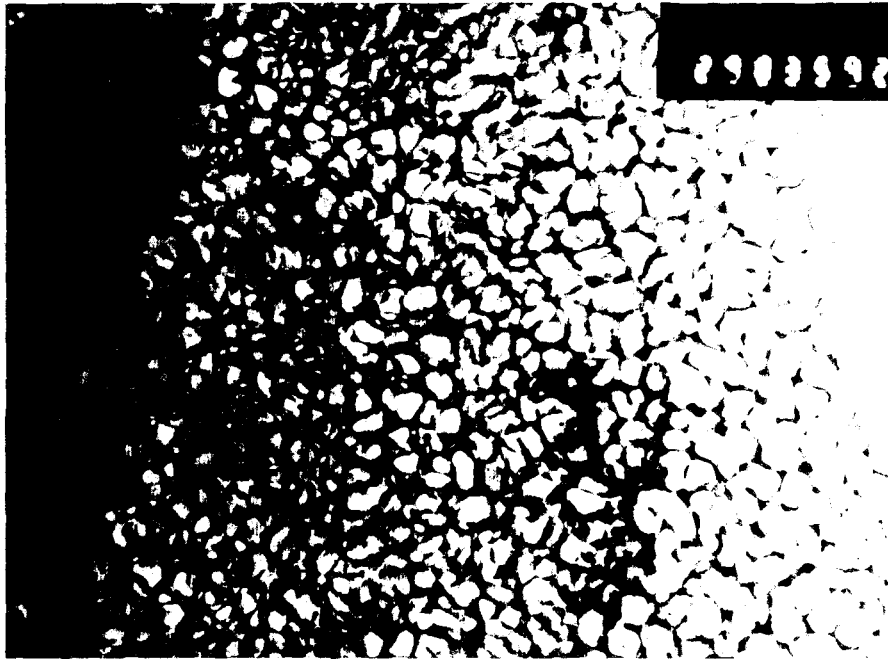


Figure 4.35 Bright field image showing uniform microcellular structure from as-cast melt-spun ribbon 30 μm in thickness obtained from the alloy #2. (x 43500)

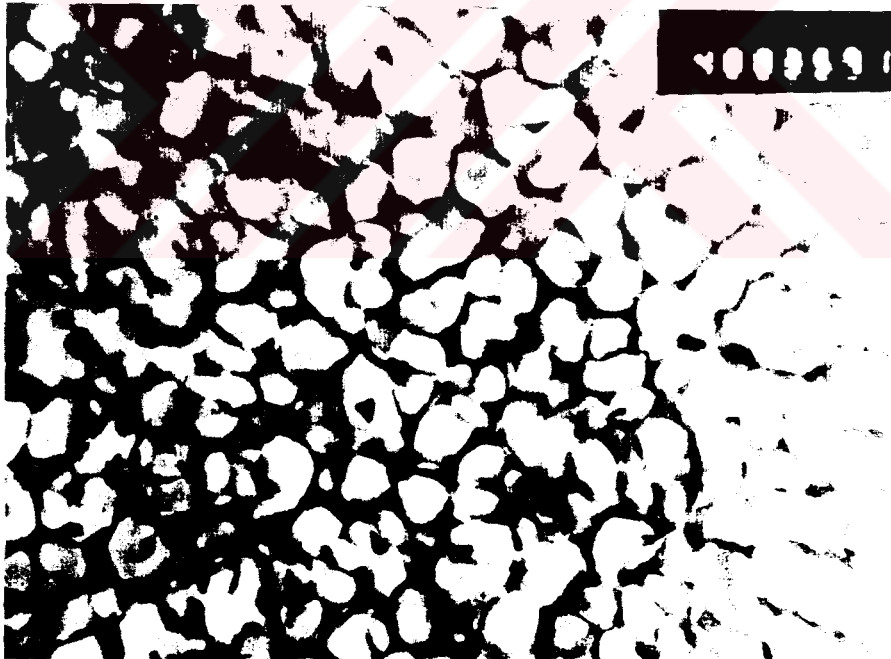


Figure 4.36 Bright field image showing uniform microcellular structure from as-cast melt-spun ribbon 30 μm in thickness obtained from the alloy #2. (x 72000)



Figure 4.37 Bright field image from as-cast melt-spun ribbon 98 μm in thickness obtained from the alloy #2. (x 40600)

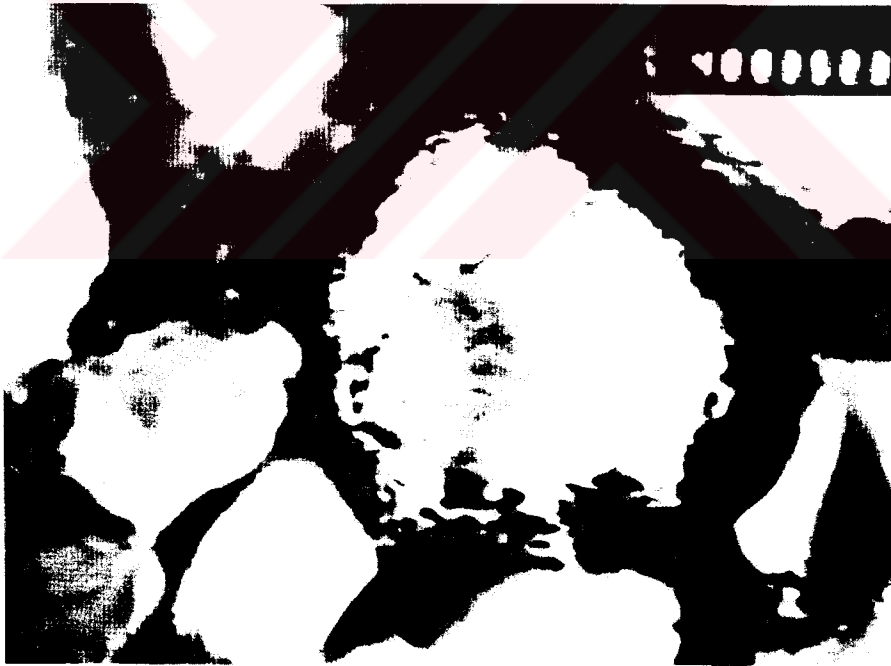


Figure 4.38 Bright field image from as-cast melt-spun ribbon 250 μm in thickness obtained from the alloy #4. (x 72000)

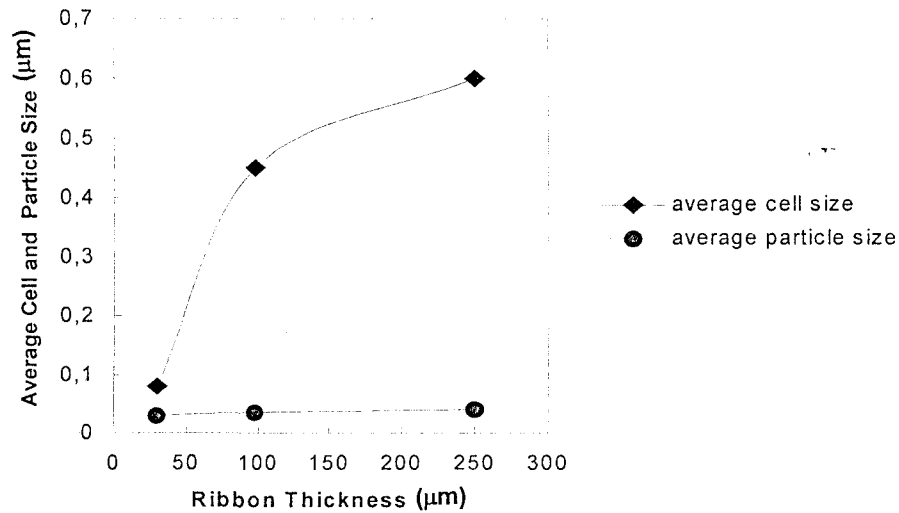


Figure 4.39 Effect of ribbon thickness on average cell and particle size.

4.4.2 Effect of Cooling Rate on Chemical Homogeneity

The TEM micrographs seen in Figure 4.40 and 4.41 indicate an uncommon result in the microstructural morphology of the melt-spun ribbon obtained from only the alloy #4. In the TEM micrograph, some regions have common cellular type morphology however, in contrast to expectations, the adjacent region have elongated cells characterizing the eutectic type solidification. If it is considered that the molten alloy #4 solidified at relatively slower rate (about 10^5 °C/s) depending on the ribbon thickness (about 250 µm), this different structure may be explained by the phenomenon of “recalescence”. Solidification rate achieved in thicker ribbon is sharply reduced locally because of recalescence and therefore the eutectic structures produced are usually appropriate for dilute alloy. [39]

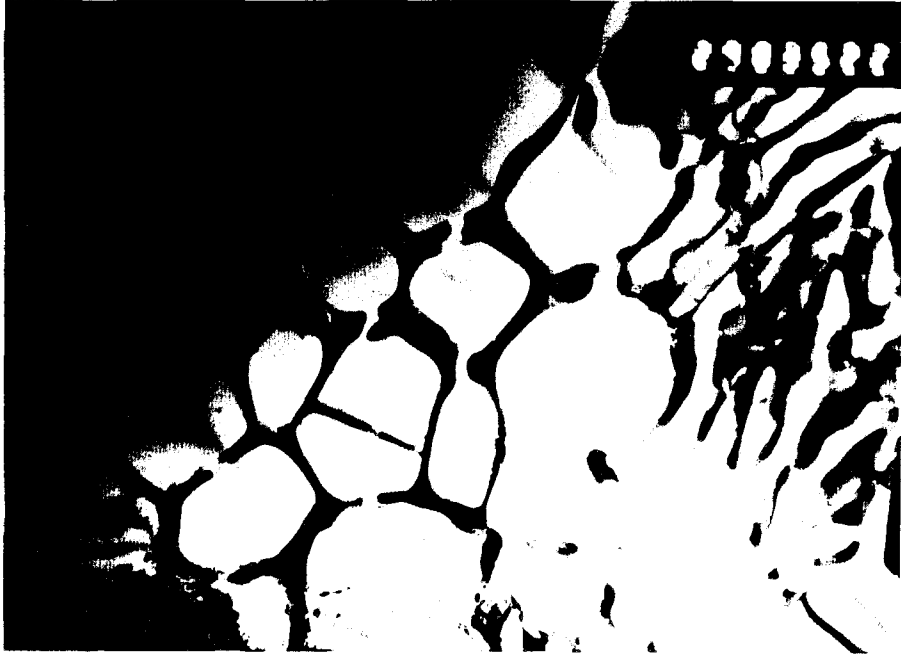


Figure 4.40 Bright field image showing cellular and eutectic type structure together from as-cast melt-spun ribbon 250 μm in thickness obtained from the alloy #4. (x 43500)

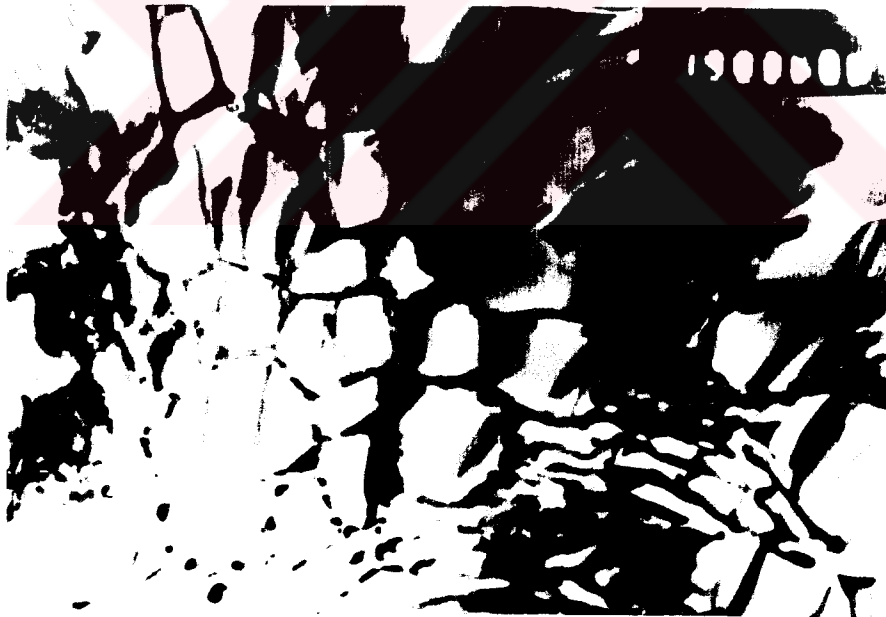


Figure 4.41 Bright field image showing cellular and eutectic type structure together from as-cast melt-spun ribbon 250 μm in thickness obtained from the alloy #4. (x 26300)

4.4.3 Effect of Cooling Rate on Solubility Extension of Alloying Elements

SEM examination revealed the presence of vanadium rich precipitates. It was observed only in the microstructure of the melt-spun ribbons obtained from the molten alloy #4 (see Figure 4.33). TEM study have confirmed that the different precipitates apart from silicide dispersoids exist in the same ribbon microstructure. It is very obvious that these precipitates showing in the TEM micrographs are vanadium rich ones. Figures 4.42 and 4.43 characterize the zone that vanadium rich precipitates and silicide dispersoids coexist in intercellular regions. In dark field image (Figure 4.43) these two types of precipitates shine together at the cell boundaries due to their diffraction spots mostly fit into one another. Therefore, there is too difficult to make any difference between them from the micrographs. But, when considering their diffraction patterns as indicated in Figure 4.44 and 4.45 vanadium rich precipitates give ring shape diffraction pattern dissimilarly.

As it is reported before, the chemical composition of the molten alloy #4 whereby the melt-spun ribbons about 250 μm in thickness obtained, was designed to have highest amount of vanadium, 3.7 wt %, however the corresponding cooling rate was the slowest one, about 10^5 $^{\circ}\text{C}/\text{s}$. While most of vanadium in alloy #4 is not dissolved, in the alloy #3 in which the amount of vanadium is 3.0 wt %, it completely dissolved. Although the vanadium percentages of these two alloys are very close to each other, their cooling rates are quite different. The molten alloy #3 solidified at about ten times higher cooling rate in magnitude, noted as 10^6 $^{\circ}\text{C}/\text{s}$, than the alloy #4.

As a result of this observation we can conclude that solidification rate limits the solubility extension of alloying elements. If the molten alloy #4 could be solidified as much more thinner ribbons, such as about 30 μm , it might be showed no indication of other intermetallics, like vanadium rich pricipitates, apart from silicide cubic phase.



Figure 4.42 TEM bright field micrograph shows that vanadium rich pricipitates and silicide dispersoids are coexist at the cell boundaries. (x 54000)

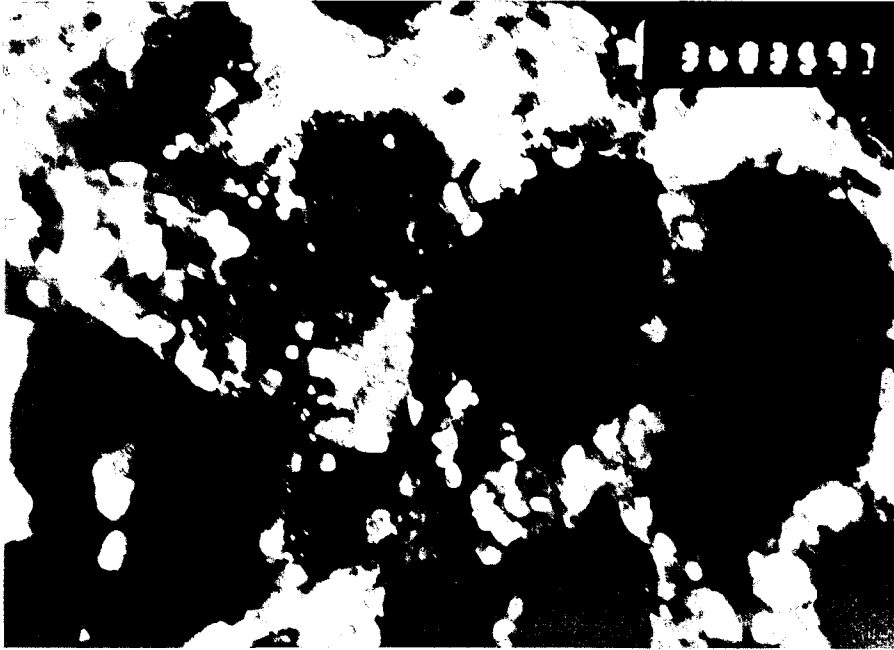


Figure 4.43 TEM dark field image of Figure 4.42. Vanadium rich precipitates and silicide dispersoids shine together at the cell boundaries. (x 54000)

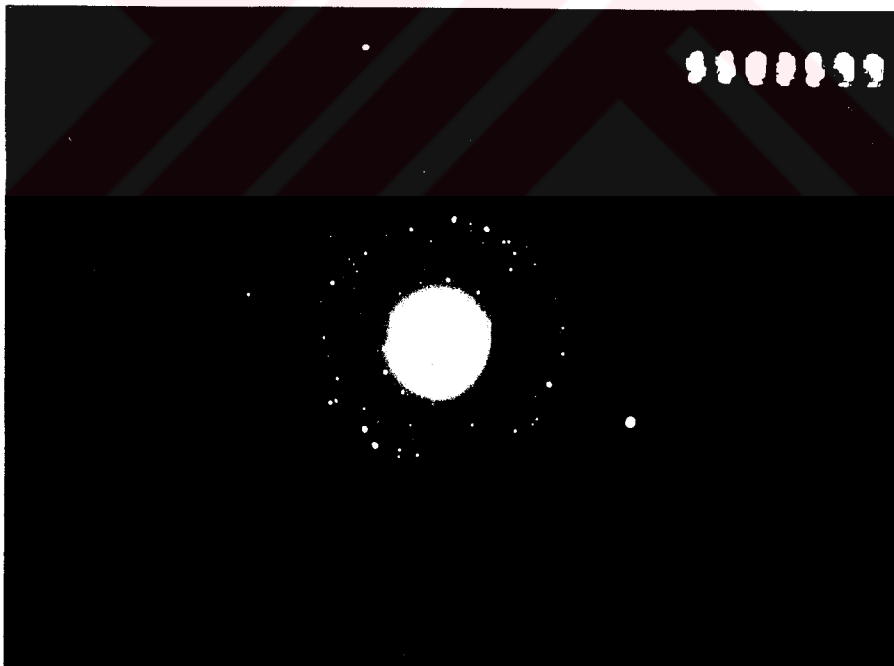


Figure 4.44 Diffraction pattern of vanadium rich precipitates.

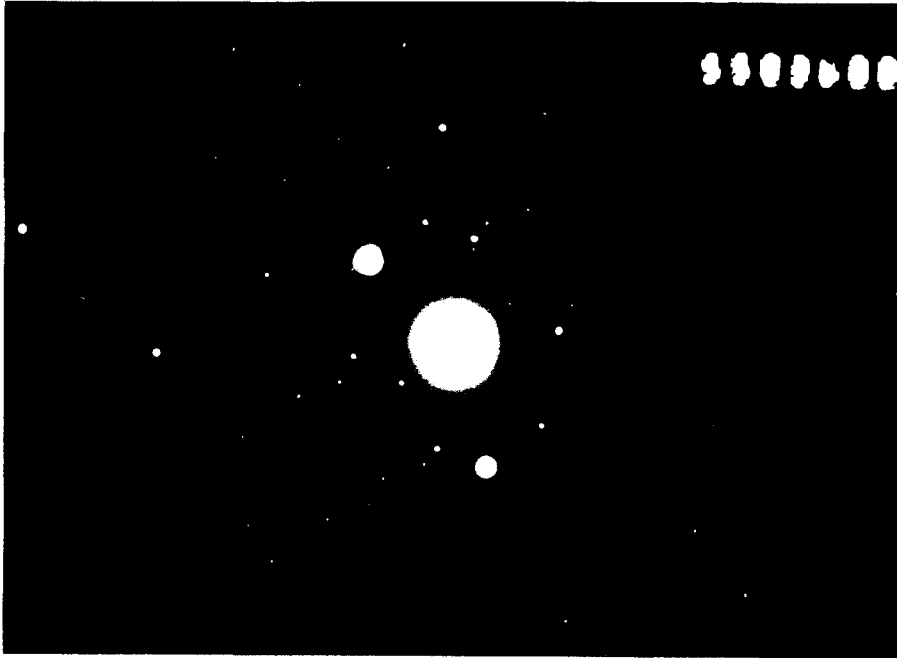


Figure 4.45 Diffraction pattern of silicide dispersoids.

4.4.4 Identification of Quasi-Crystalline Icosahedral Phase

It has been reported by Schechtman *et al* [19] that a quasi-crystalline icosahedral phase (i-phase) in rapidly solidified Al based alloys were discovered after performing a series of experiments. The melt-spun alloy were reported as containing of many randomly oriented icosahedral phase particles which are truly metastable and have symmetries intermediate between those of a crystal and a liquid in intercellular regions. The researchers studied on RS Al-Fe-V-Si alloys after Schechtman *et al* have demonstrated that the BCC structure of $Al_{12}(Fe,V)_3Si$ dispersoids are closely related to that of quasi-crystals as it is written in Chapter 2.

In the section of XRD Study, we pointed out that the similarities between two XRD patterns of Al-Fe-V-Si alloys presented in Figures 2.18 and 4.11 so that the first one is from Tang *et al* [31] investigation and the latter belongs to our study. We expected naturally to observe globular i-phase particles showing a typical icosahedral symmetry in TEM examination. It is observed, in accordance with our expectation, that similar granular (some of hexagonal) particles exist in the microstructure of the melt-spun ribbons (with about 98 μm thickness) obtained from the alloy #2. The TEM bright and dark field micrographs seen in figures 4.46 and 4.47 respectively indicate the presence of these larger particles with about 0.2 - 0.5 μm in diameter. When compared these micrographs with the Figures 2.17 (a) and (b) from the study of Tang *et al* [31], it is too easy to see the similarities between them. Unfortunately, it can not be obtained any significant diffraction patterns showing a typical icosahedral symmetry as in Figure 2.19. The diffraction pattern obtained from the larger granular (hexagonal) particles in Figures 4.46 and 4.47 is presented in Figure 4.48.

Thus, under this conditions, we suggest that the approval of icosahedral symmetry for a later study.



Figure 4.46 TEM bright field image showing randomly oriented of larger granular (hexagonal) particles. (x 43500)



Figure 4.47 TEM dark field image of above figure (x 43500)

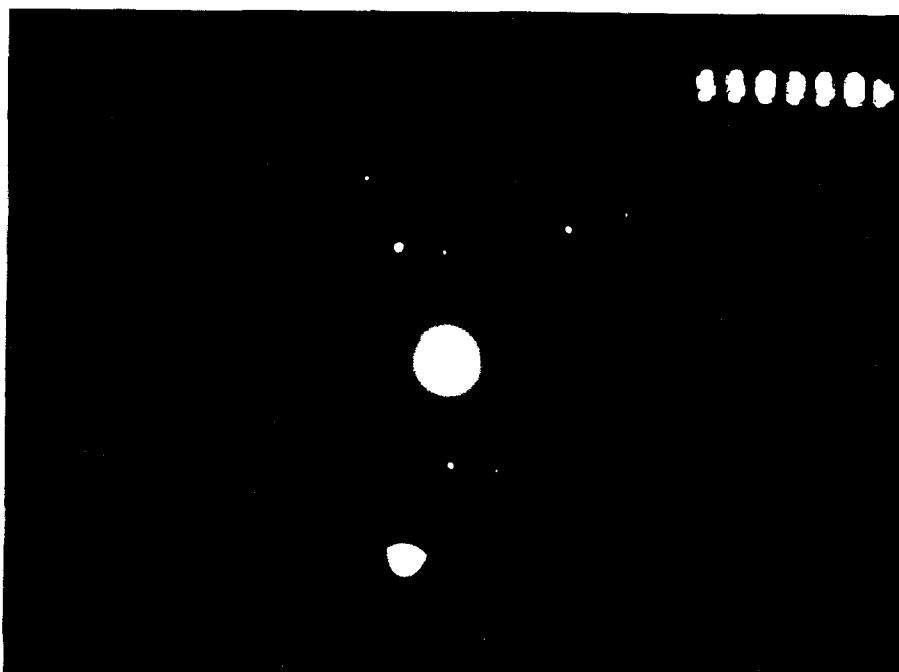


Figure 4.48 Diffraction pattern of randomly oriented granular (hexagonal) particles.

4.4.5 Effect of Heat Treatment on Microstructure of RS Al-Fe-V-Si Alloy

The heat-treated microstructure is almost the same as as-cast one for the examined ribbon about 98 μm in thickness produced from the alloy #2. Figure 4.49 characterizes the microstructure of heat-treated melt-spun ribbon at 300 $^{\circ}\text{C}$ for 1 hour. As it is seen from the figure, microcellular structure consists of aluminum matrix and intercellular silicide dispersoids is also exist in heat treated condition as well as the randomly oriented granular (hexagonal) particles. Figure 4.50 is obtained from the zone rich in those hexagonal particles. The common microstructure is also observed in the melt-spun ribbons heat treated at 400 and 500 $^{\circ}\text{C}$ as seen in Figures 4.51 and 4.52 respectively.

In addition, a different and interesting microstructural morphology is observed in only the heat treated condition at 300 °C as it is seen in Figure 4.53. Here in the structure, the silicide dispersoids formed a network.

The average cell and particle size in heat-treated conditions are 0.8 μm and 0.07 μm respectively for the examined ribbon's microstructure. When compared these values with those of the as-cast ones, the particle coarsening at a temperature up to 500 °C is not considerable. Thus, it is the evidence of high temperature stability of examined alloys confirming the SEM results.



Figure 4.49 TEM bright field image showing common microstructure from the melt-spun ribbon heat treated at 300 °C for 1 hour. (x 28500)



Figure 4.50 TEM bright field image showing granular (hexagonal) particles from the melt-spun ribbon heat treated at 300 °C for 1 hour. (x 43500)



Figure 4.51 TEM bright field image showing common microstructure from the melt-spun ribbon heat treated at 400 °C for 1 hour. (x 43500)



Figure 4.52 TEM bright field image showing common microstructure from the melt-spun ribbon heat treated at 500 °C for 1 hour. (x 43500)

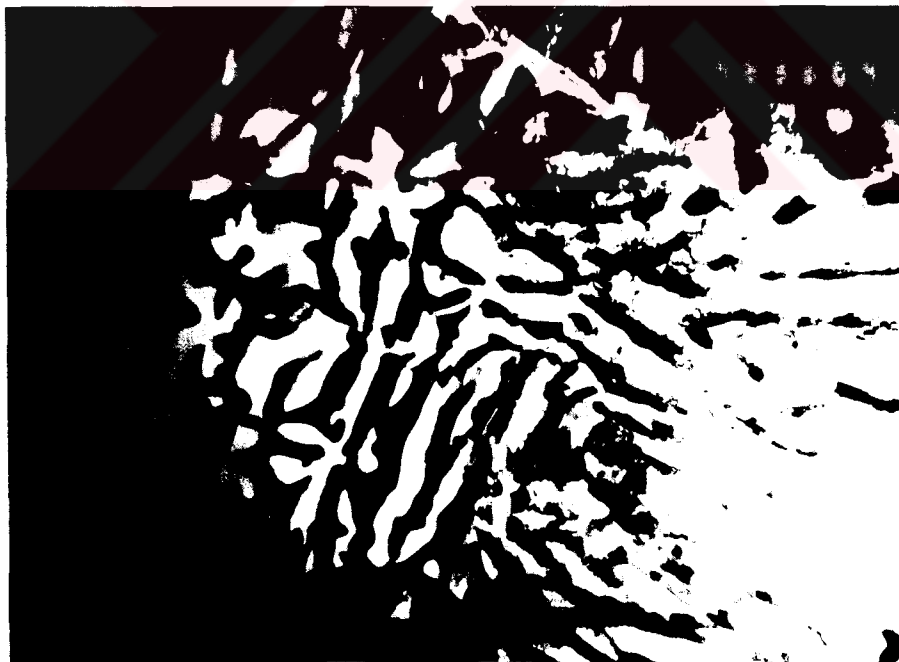


Figure 4.53 TEM bright field image showing a network of silicide dispersoids from the melt-spun ribbon heat treated at 300 °C for 1 hour. (x 28500)

4.4.6 Indexing Diffraction Patterns of Silicide Particles

The intercellular silicide particles can be indexed to ordered BCC lattice type along three zone axis' by the selected area diffraction pattern (SADP) study. Figure 4.54 compares the spot patterns produced by the silicides planes in three zones with the diagrams of single-crystal spot transmission electron diffraction patterns for b.c.c. crystal structure. The crosses in one quadrant of the diagrams indicate the positions of the spots for the ordered b.c.c. (B_2) unit cell [40]. So, we have concluded that the crystal structure of the silicide particles is ordered BCC.

Table 4.5 summarizes how to calculate the lattice parameter a of this cubic silicide particles. Column 1 shows the zone axis' of the reflecting planes. The distances R_1 and R_2 are from the diffracted spot to the transmitted beam (centre spot). This parameter is characteristic of the interplanar spacing $d_{(hkl)}$ of the reflecting plane and the magnification due to the lens settings, that is the camera constant λL . This value for 100 kv electrons is 2.242814. So, d values can be calculated for each R vectors according to the equation [40] :

$$R \text{ (cm)} d \text{ (\AA)} = L \text{ (cm)} \lambda \text{ (\AA)} \dots\dots\dots [18]$$

where L is camera length and λ is electron wavelength.

The specific (hkl) indices to the individual spots assigned in the diagrams in Figure 4.54 were listed in column 4. The last column indicates the lattice parameters calculated according to the plane-spacing equation for cubic crystals. (see Table B.1 in Appendix B)

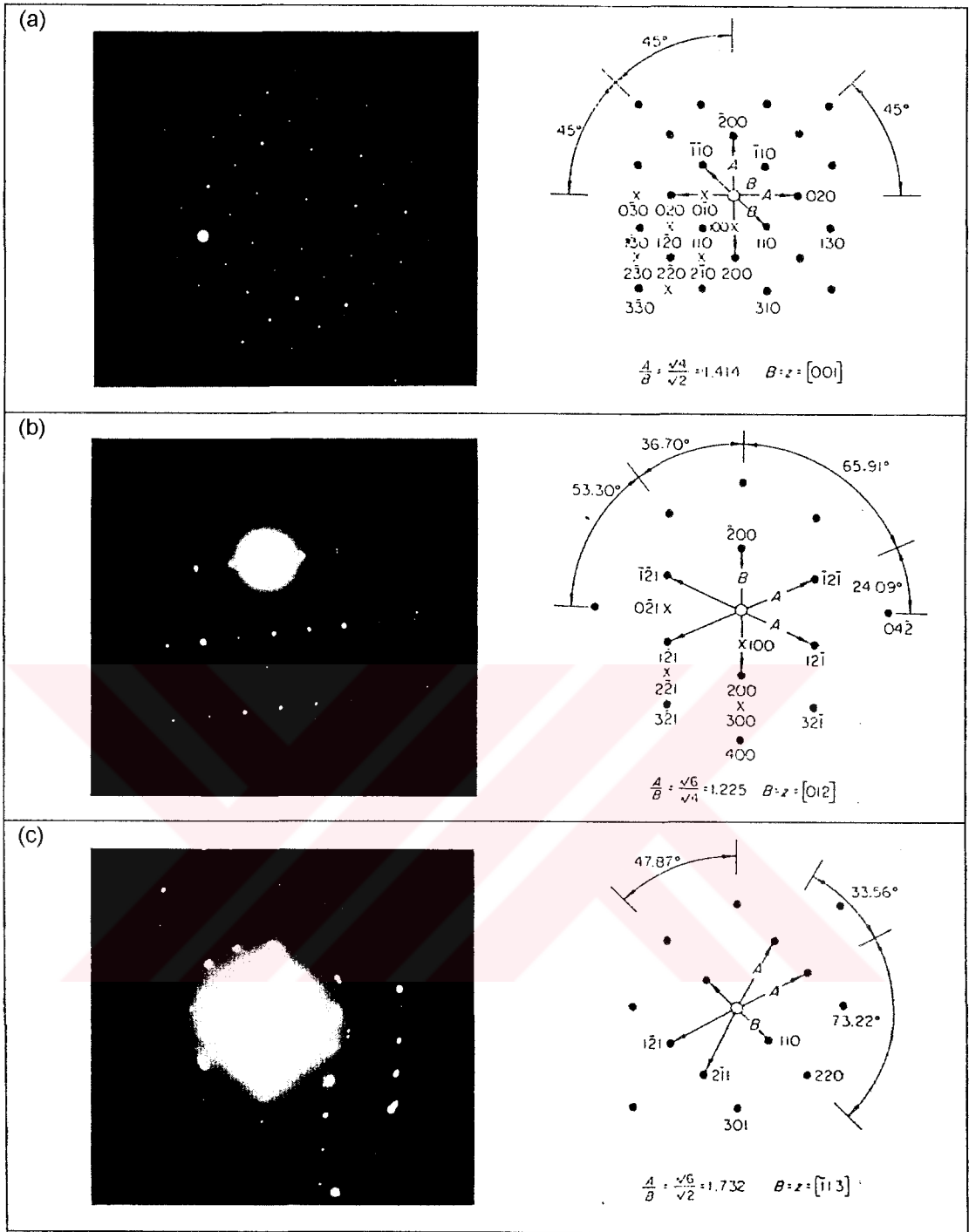


Figure 4.54 Transmission electron diffraction patterns of silicide particles corresponding to zone (a) [100], (b) [012] and (c) [113] axis. The crosses in one quadrant of the drawings indicate the positions of the spots for the ordered b.c.c. (B2) unit cell.

Table 4.5 Lattice parameter calculation for ordered BCC silicide particles.

1	2	3	4	5
z=zone axis	R ₁ and R ₂ (cm)	d=L λ / R (Å)	hkl	a = d √ h ² +k ² +l ² (Å)
[100]	0.37 0.81	6.0617 2.7689	100 210	6.0617 6.1915
[012]	0.37 0.79	6.0617 2.8390	100 021	6.0617 6.3482
[113]	0.91 0.48	2.4646 4.6725	211 110	6.0371 6.6080



Figure 4.55 TEM bright field micrograph. Microdiffraction (region marked with arrow) analysis showed that this silicide particle is along [113] zone axis. Corresponding diffraction pattern is in Figure 4.54 (c). (x 72000)

CHAPTER 5

CONCLUSIONS AND FUTURE WORKS

5.1 Conclusions

Conclusions drawn from the results of this study can be summarized as follows:

1. Ribbon formation is only possible if the continuous jet flow of molten alloy is obtained by means of the pressure applied to the molten alloy. Pressure is also a main process parameter controlling the volumetric flow rate of the melt.
2. Ribbon thickness mainly determines the solidification rate of a melt-spun ribbon. Solidification rate increases with decreasing the ribbon thickness. Resulting melt-spun ribbons varying from 30 to 250 μm in thickness have solidified at the quench rates ranging from about 10^5 to 10^7 $^{\circ}\text{C}/\text{s}$.
3. Fluid motion in the melt puddle frequently is not laminar but turbulent. The edges of crucible combining with the pressure act as the main source of turbulence. The indications of turbulent flow located at the air side of melt-spun ribbon gradually

decrease with decreasing ribbon thickness. It seems flow type of molten alloy controls the ribbon thickness due to the variation in viscosity.

4. Variations in either the thickness or width of a ribbon along its length are evidence of an unstable melt puddle. Therefore a ribbon making process needs better process control in order to obtain more uniform ribbons.
5. SEM micrographs have revealed that a high degree of microstructural refinement is achieved by rapid solidification. Rapid solidification allows only to form a second phase particles in high volume fraction which are very fine, nearly spherical and homogeneously distributed dispersoids throughout the aluminum matrix. SEM micrograph of a cross section of the melt-spun ribbon has indicated microstructural variation in the size of dispersoids from the chill to air side of the ribbon due to the difference in heat extraction.
6. Approximately 10-16 % volume fraction of second (dispersoid) phase was detected by x-ray examination. It is also evidence of solid solubility extension achieved by rapid solidification. While the fundamental lines in x-ray diffractograms could be indexed as FCC aluminum, the other lines belong to the dispersoid phase could not be indexed to any Bravais lattice. High degree of quench rate causes a reduction on the lattice parameter of aluminum and heat treatment relieves gradually this lattice distortion. Line intensity peak heights increased as a result of stress relief.

7. Electron microscopy of the melt-spun ribbons shows that RS Al-Fe-V-Si alloys have characteristically cellular morphology of FCC aluminum matrix phase and the second phase particles of the silicide phase (ordered BCC) decorate the cell boundaries. In addition, randomly oriented large (0.2-0.5 μm) granular/hexagonal particles are observed in the microstructure as the primary phase.
8. Lattice parameters of aluminum matrix and silicide dispersoids were calculated at the range of 4.0379 to 4.0542 \AA and 6.0371 to 6.6080 \AA , respectively.
9. Ribbon thickness was found to be an effective parameter to control the cell and particle size. Cell size increases strictly with the ribbon thickness, however, the size of silicide particles nearly remains constant at the range of 0.02 to 0.06 μm in diameter.
10. The microstructure of RS Al-Fe-V-Si alloys is almost stable up to 500 $^{\circ}\text{C}$ for 3 hours due to the very low coarsening rate of silicide phase. The presence of homogeneously distributed fine and nearly spherical second phase particles in high volume fraction limits the grain growth.

5.2 Future Works

The followings are suggested for the later researchs and researchers:

1. In a TEM study that is going to be done in the future, whether randomly oriented larger particles in granular/hexagonal morphology are the quasicrystalline icosahedral units or not can be identified.
2. All the melt-spun flakes and ribbons can be comminuted as powders and then consolidated as several test samples in order to investigate the mechanical properties of RS Al-Fe-V-Si alloy. A new microstructural study can also be done on the consolidated parts.
3. The available melt-spinning set-up can be advanced to a better and easier controllable one by using our experience. The experimental parameters such as pressure, jet angle, jet length, nozzle diameter etc. may be controlled and varied in a more systematic manner in order to determine their effects on the product.

REFERENCES

- [1] H. Jones, Rapid Solidification of Metals and Alloys, The Chameleon Press, London, ISBN 0901 462 18 7, April 1980.
- [2] Nicholas J. Grant, "Rapid Solidification of Metallic Particulates", High Strength P/M Alloys, 3.
- [3] R. B. Pond, U.S. Pat. 2,825,108, Metallic Filaments and Method of Making Same, Mar. 4, 1958.
- [4] R. B. Pond, Sr., "Calometric Comparison of Quench Rates in Melt Spinning and Melt Extraction", Materials Science and Engineering, 23 (1976) 87-89.
- [5] H. Hillmann and H. R. Hilzinger, "On The Formation of Amorphous Ribbons By The Melt Spin Technique".
- [6] H.S. Chen and C. E. Miller, Mat. Res. Bull., 11 (1976) 49
- [7] S. Kavesh, "Principles of Fabrication", Metallic Glasses, (1976) 36-73
- [8] T. R. Anthony and H. E. Cline, " On the uniformity of amorphous metal ribbon formed by a cylindrical jet impinging on a flat moving substrate" J. Appl. Phys., 49(2), (February 1978) 829
- [9] A. R. Yavari and P. Desré, "Substrate-induced liquid shearing and defect anisotropy in metallic glasses", J. Phys. F: Met. Phys., 14 (1984) 291-299
- [10] P. G. Zielinski and D. G. Ast, "Turbulent Flow In Chill Block Casting", Scr. Metall., 17 (1983) 291-294

- [11] H. H. Liebermann, *Rapidly Quenched Metals III*, 1 (1978) 34, The Metals Soc., London.
- [12] Hywel A. Davies, "Solidification Mechanism In Amorphous and Crystalline Ribbon Casting", *Rapidly Quenched Metals* (1985) 101
- [13] H. Jones, "Observation on a Structural Transition in Aluminum Alloys Hardened by Rapid Solidification", *Mater. Sci. Eng.*, 5 (1969-70) 1-18
- [14] D. J. Skinner, R. L. Bye, D. Raybould and A. M. Brown, "Dispersion Strengthened Al-Fe-V-Si Alloys", *Scr. Metall.*, 20 (1986) 867-872
- [15] S. K. Das, P. S. Gilman and D. Raybould, "Applications of Rapidly Solidified High Temperature Aluminum Alloys", *Key Engineering Materials*, 38-39 (1989) 367-392
- [16] S. K. Das and L. A. Davis, "High Performance Aerospace Alloys via Rapid Solidification Processing", *Materials Science and Engineering*, 98 (1988) 1-12.
- [17] C. M. Adam, in B. H. Kear, B. C. Giessen and M. Cohen (eds.), *Rapidly Solidified Amorphous and Crystalline Alloys*, Materials Research Society Symp. Proc., Vol. 8, Elsevier, New York, (1982) 411.
- [18] G Thursfield and M. J. Stowell, *J. Mater. Sci.*, 9 (1974) 1644.
- [19] D. Shechtman, I. Blech, D. Gratias and J. W. cahn, "Metallic Phase with Long-Range Orientational Order and No Translational Symmetry", *Phys. Rev. Lett.*, 53 (1984) 1951
- [20] A. Csanady, R. Wessicken, H.-U. Nissen, B. Albert, A. Griger, V. Stefaniay, "Rapidly Quenched Al-5.3 at %Mn Alloy Containing Quasicrystal Unitsé", *Material Science Forum*, 13/14 (1987) 559-566.
- [21] P. A. Bancel, P. A. Heiney, P. W. Stephens, A. I. Goldman and P. M. Horn, *Phys. Rev. Lett.*, 54 (1985) 2422

- [22] C. M. Adam and S. K. Das, in *Rapid Solidification Processing : Principles and Technologies IV*, Claitor's Publishing, Baton Rouge, Louisiana, (1988) 66.
- [23] S. K. Das, *International J. of Powder Metallurgy*, 24 (1988) 175.
- [24] A. M. Brown, D. J. Skinner, D. Raybould, S.K. Das, R. L. Bye and C. M. Adam, in *Aluminum Alloys and Their Physical and Mechanical Properties*, EMAS, West Midlands, U. K. , (1986) 1029.
- [25] B. C. Go and B. Wilshire, *Scripta Met.* 26 (1992) 435
- [26] A.K. Srivastava, S. Ranganathan and S.N. Ojha, "Effect of Processing on The Microstructural Development in a Rapidly Solidified Al-Fe-V-Si Alloy" *Processing and Fabrication of Advanced Materials for High Temperature Applications II*, The Minerals, Metals & Materials Society, (1993)
- [27] C. Suryanarayana, F.H. Froes, S. Krishnamurthy and Y-W. Kim, *Key Engineering Materials* 38-39 (1989) 343-366.
- [28] N.J. Kim, *Int. J. Rapid Sol.* 6 (1991) 175
- [29] M. Carrard, M. Gremand and M. Pierantoni, *Scripta Metall.* 25 (1991) 925
- [30] Nack J. Kim, *Int J. Rapid Solidification* 6 (1991) 175.
- [31] Y.L. Tang, S.K. Guan, D.S. Zhao, N.F. Shen and H.Q. Hu, "Effect of thermal history on δ -phase formation in rapidly quenched Al-Fe alloy", *Journal of Materials Science Letters* 12 (1993) 1749-1751.
- [32] V. Radmilovic, G. Thomas and S.K. Das, "Microstructural of α -Al base matrix and SiC particulate composites", *Materials Science and Engineering A*. 132 (1991) 171-179
- [33] A.K. Srivastava and S. Ranganathan, "A Novel Microstructure In a Rapidly Solidified Al₈₀Fe₁₀V₄Si₆ Alloy", *Scripta Metallurgica* 27 (1992) 1241-1245.
- [34] D. Munson, *J. Inst. Metals*, 95 (1967) 217

- [35] C.Y. Sun and L.F. Mondolfo, *J. Inst. Metals*, 95 (1967) 384
- [36] P. Guyot and M. Audier, "A quasicrystal structure model for Al-Mn", *Phil. Mag. B.*, 52(1) (1985) L15-19
- [37] V. Elser and C. Henley, "Crystal and Quasicrystal Structures in Al-Fe-Si Alloys", *Phys. Rev. Let.*, 55 (1985) 2883-2886.
- [38] B.D. Cullity, *Elements of X-ray Diffraction*, Addison-Wesley Publishing Company, 1978.
- [39] C.G. Levi and R. Mehrabian, *Metall. Trans. A*, 13 (1983) 13.
- [40] J.W. Edington, *Practical Electron Microscopy in Material Science*, Van Nostrand Reinhold Company (1976)
- [41] JCPDS Powder Diffraction File, Inorganic volume, second printing, 1967.
- [42] P.P. Millan, in *High Strength Powder Metallurgy Aluminum Alloys*, M.C. Koczak and G.J. Hildeman (eds), TMS-AIME, Warrendale, PA (1982) 225; also in *J. of Metals*, March 1983, 76.

APPENDIX A



Table A.1 XRD pattern obtained from the computerized x-ray diffractometer with $\text{Cu}_{K\alpha}$ radiation for Figure 4.12. The peaks numbered as 9, 15, 17, 25 and 26 are reported as the diffraction lines of aluminum as indicated in Figure 4.12. Corresponding XRD patterns of these peaks can be compared to that of aluminum ones presented in Table B.2 in Appendix B.

PEAK	2-THETA	D-SPACE	I (REL)	I (CPS)	FWHM	
1	20.900	4.2469	1.16	14.0	-0.433	#
2	22.350	3.9744	2.29	27.5	0.530	
3	24.400	3.6451	1.16	14.0	0.150	
4	26.550	3.3546	1.16	14.0	0.025	#
5	28.250	3.1565	0.50	6.0	0.025	#
6	36.300	2.4728	1.16	14.0	0.025	#
7	36.600	2.4532	1.16	14.0	0.025	#
8	37.450	2.3995	0.58	7.0	0.025	#
9	38.400	2.3423	100.00	1202.9	0.341	
10	41.900	2.1544	7.35	88.4	0.438	
11	42.450	2.1277	1.61	19.3	0.550	
12	43.100	2.0971	4.13	49.7	0.590	
13	43.400	2.0833	3.21	38.6	0.850	
14	43.750	2.0675	2.20	26.5	0.450	
15	44.650	2.0279	37.97	456.7	0.397	
16	45.550	1.9899	1.22	14.7	0.387	
17	65.050	1.4327	21.26	255.7	0.388	
18	71.200	1.3233	0.86	10.3	0.465	
19	74.250	1.2763	0.98	11.8	0.330	
20	74.850	1.2675	3.12	37.5	0.684	
21	75.250	1.2618	1.69	20.3	0.237	
22	75.650	1.2561	0.92	11.1	0.500	
23	75.900	1.2526	0.91	11.0	0.393	
24	77.600	1.2293	1.01	12.1	0.197	
25	78.300	1.2201	16.36	196.8	0.529	
26	82.400	1.1694	6.27	75.4	0.436	

26 PEAKS WERE FOUND AND WRITTEN TO THE PEAKS FILE

- peak FWHM is less than step width

APPENDIX B



Table B.1 Plane spacing equations for following crystal structures. The value of d , the distance between adjacent planes in the set (hkl) , may be found from the these equations.

Cubic	$\frac{1}{d^2} = \frac{h^2 + k^2 + l^2}{a^2}$
Tetragonal	$\frac{1}{d^2} = \frac{h^2 + k^2}{a^2} + \frac{l^2}{c^2}$
Hexagonal	$\frac{1}{d^2} = \frac{4}{3} \left(\frac{h^2 + hk + k^2}{a^2} \right) + \frac{l^2}{c^2}$
Rhombohedral	$\frac{1}{d^2} = \frac{(h^2 + k^2 + l^2) \sin^2 \alpha + 2(hk + kl + hl)(\cos^2 \alpha - \cos \alpha)}{a^2(1 - 3 \cos^2 \alpha + 2 \cos^3 \alpha)}$
Orthorhombic	$\frac{1}{d^2} = \frac{h^2}{a^2} + \frac{k^2}{b^2} + \frac{l^2}{c^2}$
Monoclinic	$\frac{1}{d^2} = \frac{1}{\sin^2 \beta} \left(\frac{h^2}{a^2} + \frac{k^2 \sin^2 \beta}{b^2} + \frac{l^2}{c^2} - \frac{2hl \cos \beta}{ac} \right)$
Triclinic	$\frac{1}{d^2} = \frac{1}{V^2} (S_{11}h^2 + S_{22}k^2 + S_{33}l^2 + 2S_{12}hk + 2S_{23}kl + 2S_{13}hl)$

Table B.2 Diffraction Index Card for Al

0 7 4 2 1 7 4 2 1 +10 7 4 2 1 7 4 2 1 +3 0													2ND		A.S.T.M.	
7 4 2 1 7 4 2 1 +20 7 4 2 1 7 4 2 1 +7 2-0													1ST CARD			
TENS GROUP CODE UNITS TENS UNITS SECOND LINE TENTHS HTHS																
4-0787 MINOR CORRECTION																
d 4-0791		2.34	2.02	1.27	2.34	AL										
I/I ₁ 4-0787		100	47	24	100	ALUMINUM										
Rad. CuKα ₁		λ 1.5405		Filter Ni		d Å	I/I ₁	hkl	d Å	I/I ₁	hkl					
Dia.		Cut off		Coll.		2.338	100	111								
I/I ₁ G. C. DIFFRACTOMETER		d corr. abs.?		Ref. SWANSON AND TATGE, JC FEL. REPORTS, NBS 1950		2.024	47	200								
Ref. SWANSON AND TATGE, JC FEL. REPORTS, NBS 1950						1.471	22	220								
						1.221	24	311								
						1.1690	7	222								
Sys. Cubic		S.G. O _H - Fm3m														
a ₀ 4.0494		c ₀		A C		1.0124	2	400								
α β γ		Z 4				0.9289	8	331								
Ref. Ibid.						.9055	8	420								
						.8266	8	422								
8 α		n ω β		t γ		Sign										
2V		D _x 2.697 mp		Color												
Ref. Ibid.																
SAMPLE PREPARED AT NBS. 99.9+ % AL AT 23°C TO REPLACE 1-1176, 1-1179, 1-1180, 2-1179, 3-0932																
1836																
CHEMICAL COMPOSITION																
MADE IN U.S.A. H93400X																
7 4 2 1 7 4 2 1 +7 2-0													HTHS			
TENS UNITS TENS UNITS TENS UNITS																
7 4 2 1 7 4 2 1 +10 +3													TENS HTHS		A.S.T.M.	

Table B.3 Quadratic Forms of Miller Indices

$h^2 + k^2 + l^2$	Cubic				Hexagonal	
	hkl				$h^2 + hk + k^2$	hk
	Simple	Face-centered	Body-centered	Diamond		
1	100				1	10
2	110	...	110		2	
3	111	111		111	3	11
4	200	200	200		4	20
5	210				5	
6	211	...	211		6	
7					7	21
8	220	220	220	220	8	
9	300, 221				9	30
10	310	...	310		10	
11	311	311		311	11	
12	222	222	222		12	22
13	320				13	31
14	321	...	321		14	
15					15	
16	400	400	400	400	16	40
17	410, 322				17	
18	411, 330	...	411, 330		18	
19	331	331	...	331	19	32
20	420	420	420		20	
21	421				21	41
22	332	...	332		22	
23					23	
24	422	422	422	422	24	
25	500, 430				25	50
26	510, 431	...	510, 431		26	
27	511, 333	511, 333	...	511, 333	27	33
28					28	42
29	520, 432				29	
30	521	...	521		30	
31					31	51
32	440	440	440	440	32	
33	522, 441				33	
34	530, 433	...	530, 433		34	
35	531	531	...	531	35	
36	600, 442	600, 442	600, 442		36	60
37	610				37	43
38	611, 532	...	611, 532		38	
39					39	52
40	620	620	620	620	40	
41	621, 540, 443				41	
42	541	...	541		42	
43	533	533	...	533	43	61
44	622	622	622		44	
45	630, 542				45	
46	631	...	631		46	
47					47	
48	444	444	444	444	48	44
49	700, 632				49	70, 53
50	710, 550, 543	...	710, 550, 543		50	
51	711, 551	711, 551	...	711, 551	51	
52	640	640	640		52	62
53	720, 641				53	
54	721, 633, 552	...	721, 633, 552		54	
55					55	
56	642	642	642	642	56	
57	722, 544				57	71
58	730	...	730		58	
59	731, 553	731, 553	...	731, 553	59	